Univerzita Karlova v Praze
Matematicko-fyzikální fakulta

DIPLOMOVÁ PRÁCE

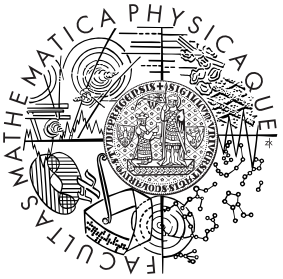

Peter Ondáč

Studium turbulence plazmatu tokamaku pomocí reciprokých sond

Katedra fyziky povrchů a plazmatu

Vedoucí diplomové práce:	Mgr. Jan Horáček, Ph.D.
Studijní program:	Fyzika
Studijní obor:	Fyzika povrchů a ionizovaných prostředí

Praha 2014

Charles University in Prague
Faculty of Mathematics and Physics

MASTER THESIS

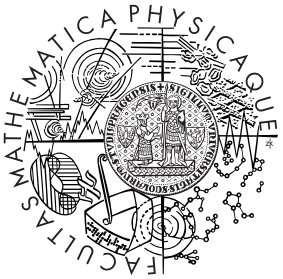

Peter Ondáč

Study of tokamak plasma turbulence by means of reciprocating probes

Department of surface and plasma science

Supervisor of the master thesis: Mgr. Jan Horáček, Ph.D.
Study programme: Physics
Specialization: Physics of surface and plasma science

Prague 2014

I would like to thank everybody who helped me any way in the processing of the thesis. Especially I am grateful to Jakub Seidl for his patient answering my questions about ESEL and my supervisor Jan Horacek for answering my questions about experimental data processing and finding a few mistakes in the thesis. Both of them also helped me in my beginnings of using the Matlab program. Thanks belongs also to prof. Jana Safrankova who glanced at my thesis and gave me a valuable feedback and prof. Milan Tichy for supervising the progress of the writing of the thesis and providing me an own place in school for working. Karel Kovarik, Petr Vondracek, Filip Janky, Tomas Markovic, Josef Havlicek answered a few my questions mainly about COMPASS data storage in Tokamak Department, Institut of Plasma Physics, Czech Academy of Sciences. S. Ondac and M. Furman found some gramatical mistakes in this thesis. I thank them for it.

The thesis is dedicated to all living organisms on Earth. We are all like one big organism cells. We are one planet.

I declare that I carried out this master thesis independently, and only with the cited sources, literature and other professional sources.
I agree with lending of this work.

I understand that my work relates to the rights and obligations under the Act No. 121/2000 Coll., the Copyright Act, as amended, in particular the fact that the Charles University in Prague has the right to conclude a license agreement on the use of this work as a school work pursuant to Section 60 paragraph 1 of the Copyright Act.

In ..... date ..... signature of the author

Název práce: Studium turbulence plazmatu tokamaku pomocí reciprokých sond

Autor: Peter Ondáč

Katedra: Katedra fyziky povrchů a plazmatu

Vedoucí diplomové práce: Mgr. Jan Horáček, Ph.D., Ústav fyziky plazmatu AV ČR

Abstrakt: Tato práce pojednává o studiu turbulencí v plazmě tokamakov a vylepšování turbulentního počítačového modelu ESEL. První kapitola pojednává o teorii související se studiem turbulencí v plazmě. Na studium těchto turbulencí jsou použity výsledky ze sondového měření na tokamaku ASDEX Upgrade a COMPASS a modelové výsledky z turbulentního počítačového modelu ESEL. Druhá kapitola popisuje použité sondy a třetí kapitola popisuje model ESEL. Přínos práce je hlavně ve čtvrté a páté kapitole, kde jsou shrnuty výsledky z porovnávání experimentálních údajů a výstupu modelu ESEL. V šesté kapitole jsou shrnuty nejdůležitější závěry z těchto porovnávání. Byly ukázány shody i neshody. Jeden z hlavních výsledků je ověření důležitosti jednoho přídavného člena v rovnicích ESEL, který znamenal jeho vylepšení. Přesto ESEL stále není schopen kompletního popisu okrajové plazmy tokamaku.

Klíčová slova: tokamak, plazma, turbulence, model, experiment

Title: Study of tokamak plasma turbulence by means of reciprocating probes

Author: Peter Ondáč

Department: Department of surface and plasma science

Supervisor: Mgr. Jan Horáček, Ph.D., Institute of Plasma Physics AS CR

Abstract: This thesis deals with the study of turbulence in tokamak plasma and improvement of an computer model ESEL. The first chapter deals with the theory related to the study of turbulence in the plasma. For the study of these turbulences the results of the probe measurements on the ASDEX Upgrade and COMPASS tokamak and model results from a computer model of the turbulent ESEL are used. The second chapter describes the used probes and the third chapter describes the model ESEL. Contribution of the work is mainly in the fourth and fifth chapter, which summarize the results of the comparisons between the experimental data and model ESEL. The sixth chapter summarizes the most important conclusions from these comparisons. Some agreements and discrepancies were shown. One of the main results of the thesis is the importance of one extra term in one governing equation of the ESEL, which means its improvement. However at present the ESEL is still not able to fully describe the tokamak plasma boundary.

Keywords: tokamak, plasma, turbulence, model, experiment

Contents

Introduction

If the humanity as a whole do not change a way of his life significantly (for example along the lines of Buddhism), it will need up to 3 times more electricity in 2050 in a high growth scenario. Beyond 2050 the energy requirements should be even higher [1].

Problems: A use of fossil fuels lead to significant global warming because of the emission of greenhouse gases. Governments of many countries has target of not allowing a temperature rise of more than 2°C [1]. 2.5°C is estimated by climatologists as a threshold for irreversible climate changes. For this it is needed to reduce the carbon emissions by about 80% in first half of the century. The fossil fuel reserves are almost depleted. Oil and gas reserves would last a few tens of years. Only the quantity of coal is for few hundred years, but the coal is the largest emitter of CO_2. In 1996 it was estimated, that reserves of coal are for 231 years, reserves of natural gas for 63 years and reserves of petroleum for 44 years [1]. [1] Even though the new reserves are discovering they are more and more difficult available - acquisition of them needs constantly more energy.

Fission based nuclear power produces a lot of long-term radioactive wastes and there is potential for catastrophic Chernobyl or Fukushima Daiichi like disasters. This disasters have a long-term bad effect on health of all organisms in far surroundings but they are unique. They are also effective and not many nuclear plants is needed. Therefore the total numbers of deaths from fission nuclear powers per kWhrs produced are small if compared to other electric energy resources [6], [7]. A new builds must be able to withstand the worst case disaster, no matter how unlikely.

Clean energy sources such as wind and solar have low efficiency, low energy density and their production is still too expensive. In the present they are not suitable for large urban industrial complexes. In the manufacture of photovoltaic panels there is generation of toxic wastes too [2].

Biofuels as ethanol or biodiesel from starch rich vegetation, sugar or from biological wastes are good but they contribute to deforestation, desertification, general loss of biodiversity and instability in food accessibility (a land determined for the biofuels can not be used for growing of a foodstuff) .

Therefore we need alternative source of energy with clean and effective energy conversion process which is cost effective, safe, environment friendly, and has easy global accessibility. The resources should be almost inexhaustible and available globally. The power plant must produce a lot of energy while occupying a small area, it must be sufficiently energy dense (for driving large scale industries).

It seems the NUCLEAR FUSION is good candidate for it. It has easy and almost unlimited access to the basic fuel, less, short-term radioactive wastes, it is safe and effective. The fuel inside the chamber will have so low density that power production stops a few seconds after fuelling is stopped. During the operation, the fusion power plant does not release CO_2 . Through manufacturing processes of some reactor components the amount of CO_2 emission (which is equal to

[1] Total fossil fuel resources including non-conventional resources such as oil shale, tar sand, heavy oil, shale gas, tar sand gas, coal bed methane, methane hydrate are accessible for around a few hundred years. But it would be unwise to deplete it all.

amount produced for its entire life cycle) should be significantly less than the coal based reactors of the same capacity produce in their life cycle [1]. A predicted ratio of the amount of radioactive material in a reactor to the allowed level of concentration in the atmosphere is for fusion reactor several orders of magnitude lower than present ratio for fission plants [1]. The tritium as main radioactive fuel in a fusion reactor can easily be discharged from human bodies through metabolism. It is a weak beta emitter. The main potential problems of radioactivity in fusion reactors should be from neutron activated reactor components. But if we use a low activity materials the components should be in a containment after decommission less than one hundred years (for fission plants the containment is needed for hundreds of years) [1]. The neutrons from a fusion reactors could change radioactive fission wastes into materials that decay more quickly. During normal operation small fractions of the radioactive materials will be released from the fusion plant. But the expected doses to the most expected public from gaseous and liquid effluents are less than 1% of the dose rate naturally occurring. In case of severe accident the expected dose to the most exposed people of the public will be around $1\mu Sv$ (the annually occcurring naturally radiation) [1]. As for safety, with the fusion reaction there is no danger of meltdown or runaway reactions. The total amount of fusion fuel in the device is at a given instant of time just enough to produce the power for a few seconds. Therefore in case of a accident the plasma will cool down quickly enough and will not cause a major explosion (in contrast to fission reactors). A structural materials of the confinement barriers will not melt in case of accident even without any cooling. For creating the conditions under which the fusion reaction can be initiated it is needed a magnetic fusion reactor or laser fusion reactor or an atomic fission device. Therefore there is very little probability that some groups of people can steal and misuse the fusion reactor components for some bad purposes. There are a lot of spin-offs of fusion research. For example a developments in high heat flux materials, superconductors, diagnostic systems, neutral beam systems, vacuum technologies, cryogenics technologies and potential interplanetary voyages. Probably only matter-antimatter and fusion based propulsion systems could provide a sufficient thrust for interplanetary spaceships.

Of course the nuclear fusion will not be sure the only one producer of clean energy. It is counted also with fission nuclear energy and clean energy as wind and solar, possibly other clean energy. Solar energy technologies see remarkable development. A plastic materials made of quantum dots can convert into electric energy even infrared solar radiation. Around 50% of the solar energy lies in the infrared spectrum [3]. A multijunction solar photovoltaic cells has a efficiency of more than 40% [5]. A cells with more than 3 junctions could has a efficiency about 58% [1].

1. Theory and Targets of the thesis

1.1 About fusion [1]

In fusion a nuclei of light elements fuse and form a nucleus of heavier elements which have less mass than the nuclei of fusing light elements. The mass difference results in the release of energy. The energy comes out mostly in the form of the kinetic energies of the products. In order to realize fusion the reactants has to come close enough so that the nuclear strong force helps them fuse by a quantum mechanical tunnelling. But the nuclei of reactants are positively charged so they has to overcome the electrostatic repulsion. Therefore the nuclei of reactants need a sufficiently kinetic energy before reaction. They can gain it in the big accelerators or by heating to very high temperatures. In second case the fusion is called the thermonuclear fusion. The energy release per unit mass of the reactants is for fusion reactions much larger as for fission reactions. [1] More (than in case of the fusion) energy per unit of mass can be released only in direct conversion mass into energy (for example matter-antimatter collision), as far as we know.

Examples of fusion reactions:

$$D + T \quad \rightarrow \quad {}^{4}_{2}\mathrm{He}(3.56MeV) \quad + \quad n^0(14.1MeV), \tag{1.1}$$

$$\begin{aligned} D + D \quad &\overset{50\%}{\rightarrow} \quad {}^{1}_{1}\mathrm{H}(3.02MeV) \quad + \quad T(1.01MeV) \\ &\overset{50\%}{\rightarrow} \quad {}^{3}_{2}\mathrm{He}(0.82MeV) \quad + \quad n^0(2.45MeV), \end{aligned} \tag{1.2}$$

$$T + T \quad \rightarrow \quad {}^{4}_{2}\mathrm{H}(7.54MeV) \quad + \quad 2n^0(3.77MeV), \tag{1.3}$$

where D is deuteron (the nucleus of deuterium), T is triton (the nucleus of tritium) and n^0 is the neutron. The ${}^{1}_{1}\mathrm{H}$, ${}^{3}_{2}\mathrm{He}$ and ${}^{4}_{2}\mathrm{He}$ are the nuclei of isotopes of the relevant chemical elements.

Research into controlled thermonuclear fusion with aim to convert fusion energy into electric energy persist more than 50 years. It has culminated in construction of the ITER (International Thermonuclear Experimental Reactor,) device which is slated to start operations in about 10 years from now. ITER should produce about 10 times more power than the input heating power and I am going to write about it in later chapters.

The ratio of deuterium to hydrogen in natural water is about 1 to 6000. Tritium has a half-life of about 12.6 years. It is unstable beta emitter and does not exist naturally. Tritium can be bred from lithium :

$${}^{6}_{3}\mathrm{Li} + n^0 \quad \rightarrow \quad {}^{4}_{2}\mathrm{He} \quad + \quad T \tag{1.4}$$

$${}^{7}_{3}\mathrm{Li} + n^0 \quad \rightarrow \quad {}^{4}_{2}\mathrm{He} \quad + \quad T \quad + \quad n^0. \tag{1.5}$$

[1] But individual fission reactions with very heavy nuclei are generally much more energetic than individual fusion reactions.

The lithium is widely a evenly available in the oceans and mainly in the Earth's crust. The fusion reaction (1.1) should be used in 1. generation fusion reactors (bigger cross-section, easy to achieve it) and the fusion reaction (1.2) should be used in 2. generation fusion reactors (weaker cross-section but lower neutron activation of materials). The fuel for fusion is likely to last several tens of thousands of years. Probably the biggest problem of the fusion are neutron activated materials (the metals become brittle, hardened and mainly radioactive). However, the reactor components from appropriate low activity materials should be in a containment after decommission less than one hundred years. In prospect is also neutron-less fusion (without unsafe radioactive materials). For example:

$$p^+ + {}^{11}_{5}\mathrm{B} \quad \rightarrow \quad 3\ {}^{4}_{2}\mathrm{He} + 8.7MeV, \tag{1.6}$$

where p^+ is the proton. In some reactions, the main reaction does not produce neutrons, but one of her chain reaction involving resulting ions or components of the fuel may produce neutrons. For example in the next reaction (1.7) there are also some reactions D+D between a deuterons , that produce a neutrons (and also produce a tritons, and then reactions D+T produce other neutrons) .

$$D + {}^{3}_{2}\mathrm{He} \quad \rightarrow \quad {}^{4}_{2}\mathrm{He}(3.6MeV) + p^+(8.7MeV). \tag{1.7}$$

In the reactors based on fusion reactions with small amount of the neutrons as the products (such as (1.6)) one has to extract very large amounts of surface heat while in the reactors based on fusion reactions with large amount of the neutrons as the products (such as (1.1)) one has to extract heat volumetrically from the reactor blankets, because the neutrons are captures in the volume of the surrounding blanket. In the first case the heat is conducted to a divertor targets which will have to bear an unprecedented amount of heat load. Therefore a great progress in ultra-high heat flux material development will be necessary for neutron-less based fusion devices. In the first generation fusion reactors with D+T reactions there will not be a direct conversion of the fusion energy to electricity because around 80% of the fusion energy goes into the neutral neutrons. It will have to be mostly used electricity generation through conventional steam turbines. But in future fusion reactors based on fusion with small amount of the neutrons as the products which give energy mainly to charged particles, it would be possible to convert about 80% of the energy from the charged particles directly into electricity (by decelerating charged particles in an electric field and using an induction effects or an electrostatic effects). It is possible to convert into electricity also microwave synchrotron radiation and roentgen bremsstrahlung radiation (by photoelectric effects in a conductive foils).

1.2 Lawson criterion [1]

Let us examine the energy balance in fusion devices. I consider in the present the most profitable reaction (1.1). The temporal variation of the internal (kinetic) energy W of the plasma may be written as:

$$\frac{dW}{dt} = P_\alpha + P_{ex} - P_{loss}. \tag{1.8}$$

The total power produced by the D-T reaction (1.1) $\boldsymbol{P_{fusion}}$ is divided between the alpha particles and the neutrons: $P_{fusion} = P_\alpha + P_n$. But only the alpha particles are charged and confined by the magnetic field and give their kinetic energy to the plasma by collisions. The neutrons are not confined by the magnetic field, therefore escape quickly without giving their energy to the plasma. They are stopped by the materials surrounding the vacuum chamber (in which the reaction happens).
$\boldsymbol{P_{ex}}$ is the external power as additional heating needed to maintain plasma if P_{fusion}(or indeed P_α) is not sufficient to compensate the total power lost by the plasma P_{loss}.
$\boldsymbol{P_{loss}}$ is the result of:

- particle and heat transport from the plasma centre towards the outside (the magnetic confinement is not perfect)

- bremsstrahlung radiation (continuous electromagnetic radiations which is produced by the deceleration of the charged particles when deflected by other charged particles in their mutual collisions)

- synchrotron radiation (the electromagnetic radiation emitted by charged particles when they are accelerated perpendicularly to their velocity, it is due to their gyration movement around magnetic field lines)

- impurity radiations (the impurities emitted by the wall surrounding the vacuum chamber and plasma which are not fully ionized produce line radiation due to the excitation and de-excitation - if the plasma is strongly polluted it may lead to an abrupt loss of plasma confinement known as a disruption)

I the $\frac{dW}{dt} = 0$ the plasma is stationary. There are defined some useful quantities:
The energy confinement time $\boldsymbol{\tau_e}$ is defined by the equation $P_{loss} = \frac{W}{\tau_e}$. This time is characteristic time of decrease in plasma energy W if the sources supplying it are abruptly cut off. The time has nothing to do with the pulse duration in fusion devices. It is dependent on some plasma and tokamak parameters and increases with increase in major plasma radius (and therefore tokamak size). Therefore ITER should be very big tokamak. The time critically depends on a properties of the plasma near the edge plasma and is in the range of 1s - 10s. It is often impossible to determine the time empirically or at least predict it, because it depends also on turbulent processes in the plasma.
The amplification factor $\boldsymbol{Q}$ is defined by the equation: $Q = \frac{P_{fusion}}{P_{ex}}$. It is not overall efficiency of the installation. A situation corresponding to $Q = 1$ is called **the Break-even**. A situation corresponding to $P_{ex} = 0$ or $Q = \infty$ is called **Ignition**. Up to the present the largest amplification factor was $Q \approx 0.64$ in the JET tokamak (Joint European Torus) in England. In ITER it shoud be $Q \geq 10$. The fusion reactors would have the ratio of created electric energy in the grid to the produced fusion energy about 0.35. Therefore Q between 20 and 40 would be sufficient for them.

Let us examine what plasma parameters (energy confinement time, density and temperature of the plasma) we need to obtain a pulse (discharge) with a

given Q at stationary state . The bigger Q, the better. Substitute into equation (1.8). Suppose the D-T plasma as a totally neutral mixture containing $50\%D$ and $50\%T$ (the density of D equals the density of T and it equals a one half of the density of electrons: $n_T = n_D = \frac{1}{2}n_e$). Suppose in addition the uniform temperature (the temperature of electrons equals the temperature of D and T: $T_e = T_D = T_T = T$). Then we have

$$W = \frac{3}{2}kT_e n_e V + \frac{3}{2}kT_D n_D V + \frac{3}{2}kT_T n_T V = 3kTn_e V, \tag{1.9}$$

where V is the total volume of the plasma (in a fusion device) and k is the Boltzmann constant.

$$\begin{aligned} P_\alpha &= f_{DT} \times E_\alpha = N_D \times \tau_{DT} \times E_\alpha = (n_D V) \times (n_T \overline{\sigma v(T)}) \times (E_\alpha) = \\ &= \frac{1}{4} n_e^2 \overline{\sigma v(T)} V E_{reac}, \end{aligned} \tag{1.10}$$

where f_{DT} is the number of fusion reactions per second, E_α is the energy of one alpha particle given off by a one fusion reaction, N_D is the number of D in V, τ_{DT} is the number of collisions one D with other T's per second, $v(T)$ is the relative velocity of D and T immediately before the collision D and T as a function of T, σ is the collision cross-section of the reaction D+T and $\overline{\sigma v(T)}$ means the mean value of $\sigma v(t)$through the all velocities of D and T.
If we substitute the definition equation of Q, the definition equation of τ_e and equations (1.9), (1.10) into the equation (1.8) at stationary state, we will get this equation:

$$n_e \tau_e = \frac{12kT}{\overline{\sigma v(T)} E_\alpha (1 + \frac{P_{fusion}}{P_\alpha Q})} \tag{1.11}$$

From (1.1) we have $\frac{P_{fusion}}{P_\alpha} \approx 5$. If we have the temperature and energy in keV then k=1. $E_\alpha \approx 3560keV$. For $T \in \langle 10keV; 20keV \rangle$ is $\overline{\sigma v(T)} \approx 1.18 \cdot 10^{-24}\, T^2 \frac{m^3}{s\ (keV)^2}$, where T is in keV. After substituting this numbers we are getting this equation:

$$n_e \tau_e T \approx \frac{2.86 \cdot 10^{21}}{(1 + \frac{5}{Q})} \frac{keV}{m^3\ s} \tag{1.12}$$

We need $Q > 1$, therefore we need:

$$n_e \tau_e T > 4.76 \cdot 10^{20}\ \frac{keV}{m^3\ s} \tag{1.13}$$

The equation (1.13) is known as the **Lawson criterion**. We can see from (1.11) if we have a fusion reaction with smaller cross-section and smaller fusion energy yield per one reaction (for example (1.2)) we need a larger $n_e \tau_e T$ product. For D-T reaction (1.1) is at the relatively low temperature the collision cross-section relatively high (D and T has very low binding energy per nucleon).

1.3 Tokamaks [1]

For the fusion we need hold a plasma with the fusion reactants confined for a sufficiently long time away from surrounding material walls and with at sufficiently high temperature and density. For achieving it there is known magnetic

and inertial confinement of the plasma. These thesis is about magnetic confinement fusion, specially about a tokamaks (Fig.1.1) . By the tokamaks it has been achieved the most successful way of trapping the plasma particles in the magnetic field. The tokamaks are the most promising candidate for the 1. generation fusion reactors . They are a fusion devices in which the plasma is formed in the shape of a torus and and the overall magnetic field for trapping the plasma consists of a toroidal magnetic field, a poloidal magnetic field (Fig.1.1) and a vertical magnetic field. The toroidal magnetic field is formed by the toroidal field coils shaped poloidally, the poloidal magnetic field is formed by a passing a toroidal plasma current with density $\boldsymbol{j}$ and the vertical magnetic field $\boldsymbol{B}_v$ can be produced by vertical field coils which are shaped toroidally and are concentric with the torus. Why the 3 components of the magnetic field? A steady magnetic field forces the charged plasma particles to move perpendicular to the magnetic induction lines along helical trajectories and restrain their motion across the magnetic induction lines. But the magnetic field allows them to move freely along the magnetic lines and we want to trap them as long as possible. Therefore **the closed toroidal magnetic induction lines**. But the Grad-B drift and the Curvature drift lead to a charge separation and the consequent electric field causes $E \times B$ drift which leads to a rapid loss of the plasma to the walls if the magnetic induction lines are only toroidal. Therefore **the poloidal component** of the magnetic field is needed. But the magnetic field with toroidal and poloidal magnetic component decreases radially and therefore a magnetic pressure proportional to B^2 decreases radially. The bigger magnetic pressure inside and the lower magnetic pressure outside of the plasma current can be interpreted as a magnetic hoop force which tries to expand the plasma radially outward. To achieve radial equilibrium **the vertical magnetic field** component is needed to use so that the $\boldsymbol{j} \times \boldsymbol{B}_v$ is directed radially inward. If If we have the three components of magnetic field in the plasma, the charged plasma particles can move across the magnetic induction lines only by collisions or through turbulence.

The toroidal plasma current is mostly driven inductively by a transformer. The plasma itself is a secondary winding of the transformer. In such case the plasma current is transient. However the toroidal plasma current can also be driven non-inductively. For example by a high energetic neutral particle beams , by a radio frequency waves at special resonant frequencies and mainly by a toroidal bootstrap current (it will be discussed more in the subsection 1.5.2). In future most of the toroidal plasma current will be bootstrap driven.

In the tokamak the plasma pressure is much smaller than the magnetic field pressure (if it was not the plasma would not be confined). The magnetic field pressure is proportional to the B^2 and the plasma pressure is proportional to the $n.T$, where B is the induction of the magnetic field, n and $T \approx 10keV$ is the density of the plasma and temperature of the plasma respectively. The B is limited by technological constraints. Therefore the density of the plasma must be low (about $5 \times 10^{20} m^{-3}$, density of the air at atmospheric pressure is about $5 \times 10^{25} m^{-3}$).

The plasma in the tokamak is heated to about $1keV$ by internal plasma currents (above temperature about $1keV$ is ohmic heating ineffective because the plasma resistivity decreases as the temperature of the plasma increases). For further heating to higher temperature high energetic neutral particle (isotopes

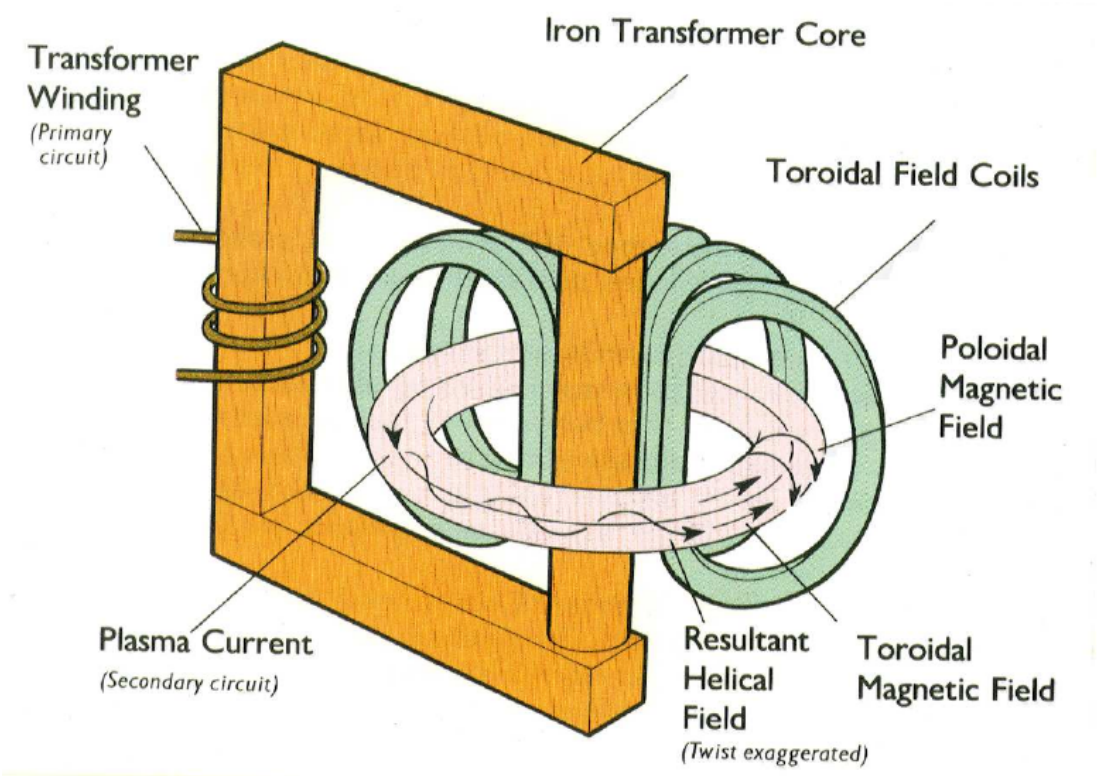

Figure 1.1: Schematic of a tokamak. [31]

of hydrogen) beams and high power radio frequency waves (with ion cyclotron, electron cyclotron, lower hybrid frequencies) are used. But the auxiliary heating techniques amplify a turbulent processes in the plasma. At present a D-shaped poloidal cross-section of the plasma is very often used. It is provided by shaping the poloidal magnetic field by an additional set of poloidal field coils concentric with the torus of the tokamak. The D-shape is good for achieving higher plasma current and higher ratio of the plasma pressure to the magnetic pressure. In present tokamaks the plasma is initiated from a limiter configuration (the plasma is restricted by the material limiter). Then the currents in the poloidal field coils are changed and the plasma is gradually brought to the divertor configuration (the outermost magnetic field lines are opened up and travel in a direction to a divertor targets). The divertor is useful mainly for reducing impurities in the plasma.

In the plasma, there are lot of internal instabilities and above or close to certain plasma current and density limits they result in a plasma disruptions.

1.4 Classical transport [8], [32]

Without instabilities the transport of energy and particles in the tokamak plasma is determined by Coulomb collisions . This transport has been calculated but the transport which actually occurs does not agree with it. The observed thermal transport by electrons can be even two orders of magnitude higher than predicted transport. The higher observed transport is probably due to instability of the plasma. But there is still no conclusive agreement between calculated

transport in which a range of instabilities has been included and experimental observed transport. Therefore an empirical methods are necessary for predicting the confinement of the tokamak plasma. For example to accumulate data from a number of tokamaks and by using statistical methods to determine how the confinement time depends on the involved parameters.

The **classical transport** is a transport in terms of a simple diffusion process, e.g. in a cylindrical plasma. The classical particle flux perpendicular to magnetic field $\boldsymbol{B}$ associated with diffusion is [32]

$$\Gamma_\perp = n\boldsymbol{v}_\perp = n\frac{\boldsymbol{E}\times\boldsymbol{B}}{B^2} - D_{C\perp}\nabla n = n\frac{\boldsymbol{E}\times\boldsymbol{B}}{B^2} - (\frac{\eta_\perp n(kT_i + kT_e)}{B^2})\nabla n, \quad (1.14)$$

$$n \approx n_i \approx n_e,$$

$$\boldsymbol{v} \equiv \frac{n_i M\boldsymbol{v}_i + n_e m\boldsymbol{v}_e}{n_i M + n_e m} \approx \frac{M\boldsymbol{v}_i + m\boldsymbol{v}_e}{M+m},$$

where **E**,**B** is the vector of electric and magnetic field respectively in the plasma, n_i, T_i, M,v_i is the density, temperature, mass and velocity of the ions respectively, n_e, T_e, m, v_e is density, temperature, mass and velocity of the electrons respectively, k is the Boltzmann constant, $D_{C\perp}$ is the classical perpendicular diffusion coefficient and $\eta_\perp$ is the perpendicular component of the specific resistivity of the plasma.

The classical perpendicular diffusion coefficient $D_\perp$ is then proportional to $1/B^2$ and n. Since η is proportional to $kT_e^{-3/2}$ it is also proportional to $kT_i^-1/2$ or $kT_e^{-1/2}$ and decreases with increasing temperature of the plasma. But the experimental observed diffusion increases with increasing temperature of the plasma. The particles moves across $\boldsymbol{B}$ with a step length equal to twice the Larmor radius. Therefore this diffusion can by slowed down by increasing B.

The classical transport model is inappropriate in a torus of the tokamak. For the collisional transport the neoclassical transport model is needed. The approximate confinement times are :

$$\tau \sim \frac{a^2}{D_\perp} \sim \frac{a^2}{\rho^2/\tau_c} \qquad classical, \quad (1.15)$$

$$\tau \sim \frac{T^{1/2}B_p^2 l^2}{n} \qquad neoclassical, \quad (1.16)$$

$$\tau \sim \frac{B_p^2 l^{1.8}}{Tn} \qquad scaled\ \ from\ \ an\ \ experiments, \quad (1.17)$$

where a is the minor radius of the plasma, ρ is the Larmor radius of the particle, τ_c is a characteristic collision time, T is the temperature of the plasma , B_p is the poloidal magnetic field and l is the plasma size.

By increasing the heating power there can be discontinuous improvement in confinement and the confinement time increase approximately two times. We call it the transition from L-mode to **H-mode**. This transition is mainly due to the appearance of an edge transport barrier.

1.5 Neoclassical transport [8]

We distinguish three main types of the neoclassical transport for different collision frequency. We can see it in Fig.1.2. The collision frequency increase with decreasing temperature. At high thermonuclear temperatures the time the electrons are in the vicinity of the ions is very small and the plasma is essentially collisionless.

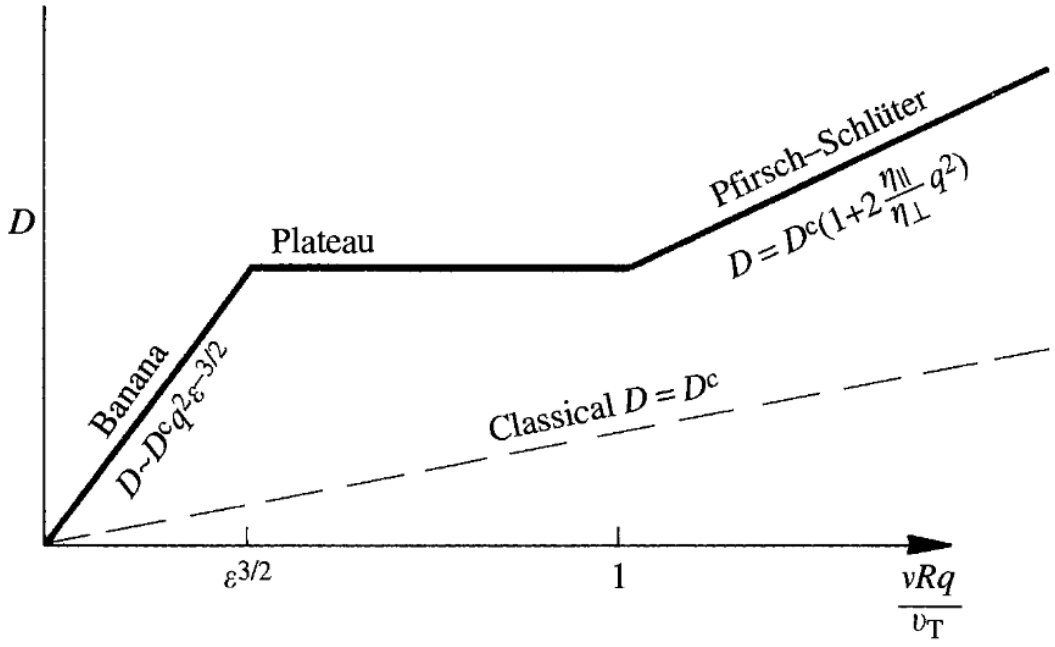

Figure 1.2: Neoclassical transport. [8]

1.5.1 Pfirsch-Schlüter transport

The radial decrease of plasma pressure causes the hoop force that acts outward along the major radius of the tokamak. This is the important difference between cylinder and toroidal plasma. On each magnetic flux surface (Fig.1.3) in which the magnetic filed lines lie, the plasma pressure p is constant and decrease with increasing minor radius coordinate because of the equation

$$\nabla n = \boldsymbol{j} \times \boldsymbol{B}. \tag{1.18}$$

The hoop force per unit volume is approximately

$$F_h \sim -\frac{r}{R}\frac{dp}{dr}, \tag{1.19}$$

where r is the minor radius coordinate and R is the major radius coordinate. This radial force must be balanced by a $\boldsymbol{j} \times \boldsymbol{B}$ per unit volume with essentially vertical current $\boldsymbol{j}_h$ perpendicular to the magnetic field. His vertical component is

$$j_{hv} \sim -\frac{r}{BR}\frac{dp}{dr}. \tag{1.20}$$

To prevent the charge accumulation in the lower and upper parts of the plasma there must be another return current. This another current was discovered by Pfirsch and Shlüter who showed it is parallel current $\boldsymbol{j}_{PS}$ along the magnetic field. His vertical component $j_{||v}$ must be equal and opposite to $j_h v$ as illustrated in Fig.1.4. Therefore the Pfirsch-Schlüter parallel current is

$$j_{PS} \sim \frac{B}{B_p} j_{||v} \sim -\frac{r}{B_p R} \frac{dp}{dr}. \tag{1.21}$$

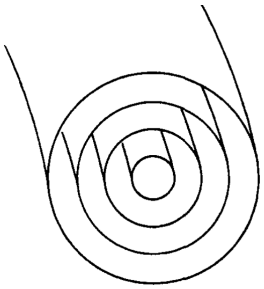

Figure 1.3: Magnetic flux surfaces forming a set of nested toroids. [8]

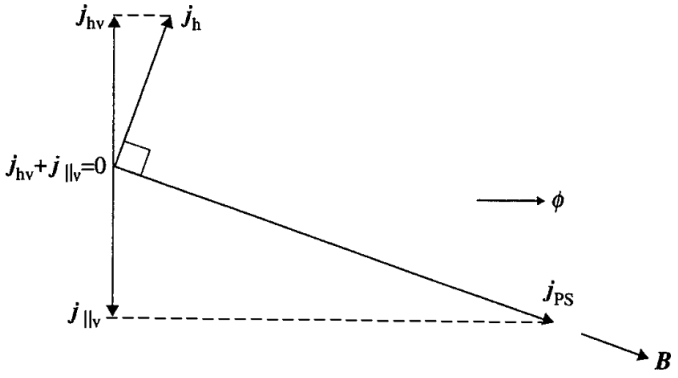

Figure 1.4: The balancing of the vertical components of the Pfirsch-Schlüter parallel current and the hoop force perpendicular current. [8]

The fluid equations used for description the classical diffusion in a cylinder plasma can be used also for the torus plasma if the temperature of the plasma is low enough and the collisions are frequent enough. The sufficiently frequent collisions means that a trapping of particles in the region of lower magnetic field on the outer side of the torus is negligible. But we must take into account the Pfirsch-Schlüter parallel current which gives one extra term in transport equation 1.14 called Pfirsch-Schlüter diffusion. The resultant perpendicular diffusion coefficient is then

$$D_{PS\perp} = (D_{C\perp})(1 + 2q^2 \frac{\eta_{||}}{\eta_\perp}), \tag{1.22}$$

where $\eta_{||}$ is the parallel component of the specific resistivity of the plasma and q is the safety factor. In an axisymmetric equilibrium the value of q has each magnetic field line and all magnetic field lines on a certain magnetic flux surface have the same q. If the field line which follows a helical path on its associated magnetic flux surface returns to the same position in the poloidal cross section after change of toroidal angle $\delta\Phi$ the q is defined by

$$q = \frac{\delta\Phi}{2\pi}. \tag{1.23}$$

1.5.2 Banana regime transport

The guiding centre is the centre about which the particle gyrates. The trajectory formed by the guiding centre is called guiding centre orbit or drift trajectory. If

the temperature of the plasma is higher and hence collisionality smaller the fluid equations cease to be applicable. The particles can be in inhomogeneous magnetic field trapped due to "mirror effect" in the lower magnetic field on the outer side of the torus. Particles with a parallel velocity

$$v_{||} \gtrsim \sqrt{\frac{r}{R}} v_{\perp}. \tag{1.24}$$

circulate continually around the torus and are called passing particles. The remaining particles with parallel velocity

$$v_{||} \lesssim \sqrt{\epsilon} v_{\perp}, \tag{1.25}$$

where $\epsilon = r/R$ is the inverse aspect-ratio of the magnetic surface and r,R are minor and major radius coordinate respectively. are trapped and are called trapped particles. The guiding centre orbit of the trapped particles are called banana orbits because its projection onto a poloidal cross-section look as a banana as illustrated in Fig.1.5.

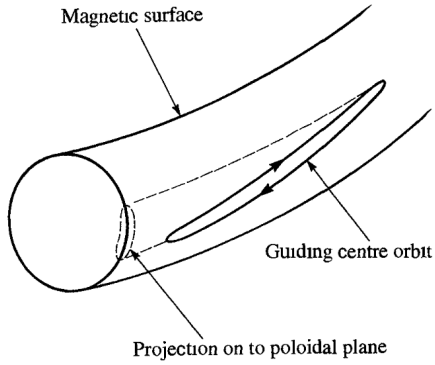

Figure 1.5: The banana orbit and its projection onto a poloidal plane. [8]

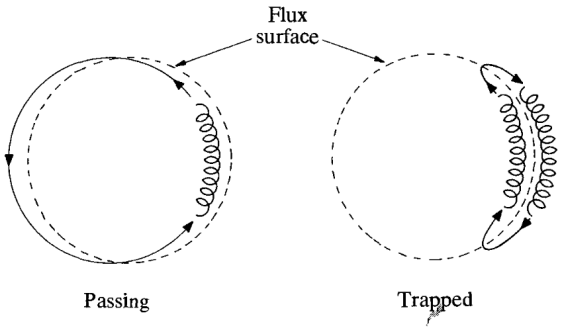

Figure 1.6: The poloidal cross-section of the orbits of a passing and a trapped particle. [8]

Both types of orbits lie within a small distance (order of the Larmor radius) of a magnetic flux surface as we can see in Fig.1.6 due to the conservation of the angular momentum. The width of the banana orbits is

$$w_b \simeq \frac{q}{\sqrt{\epsilon}} \rho. \tag{1.26}$$

It is larger than the Larmor radius and hence allow a greater diffusion with bigger step-length as in case of classical diffusion.

The fraction of the trapped particles is $v_{||}/v_{\perp} \sim \sqrt{\epsilon}$ but at small collisionality these particles dominate the transport. The transport is in the banana regime when the collisionality is such low that trapped particles complete at least one bounce orbit before they suffering a collision which cause a detrapping. Or a bounce frequency ν_b is higher than effective collision frequency ν_{ef} for detrapping otherwise there are not the banana orbits. The particles step across the flux surface by the step length $\sim w_b$ with the effective collision frequency ν_{ef}. Only a

fraction $\sim \sqrt{\epsilon}$ of the particles are trapped. We can estimate the perpendicular diffusion coefficient for the banana regime as

$$D_{B\perp} \sim \sqrt{\epsilon}\nu_{ef} w_b^2 \sim \sqrt{\epsilon}\frac{\nu}{\epsilon}\rho^2 \sim \nu\rho^2 \frac{q^2}{\epsilon^{3/2}} \sim D_{C\perp}\frac{q^2}{\epsilon^{3/2}} \tag{1.27}$$

where ν is the collision frequency. The condition for the ν in banana regime is

$$\nu < \epsilon\nu_b = \frac{\epsilon^{3/2} v_T}{qR}, \tag{1.28}$$

where v_T is the thermal velocity of the particle. Near the magnetic axis, where w_b is comparable to the distance from the magnetic axis, the width of the orbit of the trapped particle is

$$w_{pot} \sim \frac{q}{\sqrt{\epsilon_{pot}}}\rho = \frac{q}{\sqrt{w_{pot}/R}}\rho = \sqrt[3]{q^2 R\rho^2}. \tag{1.29}$$

The orbit is called potato orbit, because of the shape of the orbit, $w_{pot} > w_b$. The larger width of the orbit means larger step length and it means larger diffusion transport near the magnetic axis.

Like the Pfirsch-Schlüter parallel current is consistent with the Pfirsch-Schlüter diffusion the additional friction in the higher banana regime transport implies the toroidal **bootstrap current**. This current exists independently of the current driven by an induced toroidal electric field. It can be maintained by steady radial diffusion. Due to possibility to provide part of the poloidal magnetic field by them there is the term "bootstrap". The trapped ions and trapped electrons in the presence of a density gradient carry a parallel current analogous to the diamagnetic current of untrapped particles. As they are passing each other there is a transfer of momentum between them and their velocities are changed. The resultant current is the bootstrap current

$$j_b \sim -\frac{\sqrt{\epsilon}}{B_p}\frac{dp}{dr}, \tag{1.30}$$

where dp/dr is radial plasma pressure gradient. In contrast to the electromagnetically induced current this current peaks off-axis and equals zero at the plasma centre.

1.5.3 Plateau transport

For the collision frequency ν of the particles

$$\frac{\epsilon^{3/2} v_T}{qR} < \nu < \frac{v_T}{qR}. \tag{1.31}$$

the transport is dominated by a particles with low $v_{||}$. This domain is During a one transit round the torus the change of the parallel velocity is small, $\delta v_{||} \sim v_{||}$. The effective collision frequency for the collisions resulting in $\delta v_{||}$ is

$$\nu_{ef} \sim \frac{v_{||}}{Rq}. \tag{1.32}$$

In the time between two collisions the particle move around the torus and drifts a radial random walk step with the length

$$d \sim v_d/\nu_{ef}, \tag{1.33}$$

where v_d is the magnitude of the magnetic drift velocity $\boldsymbol{v}_d$

$$\boldsymbol{v}_d = \frac{v_{||}^2 + \frac{1}{2}v_\perp^2}{\omega_c}\frac{\boldsymbol{B}\times\nabla B}{B^2}, \tag{1.34}$$

ω_c is the cyclotron frequency of the particle. The fraction of the diffusing particles is $\sim v_{||}/v_\perp \sim v_{||}/v_T$ and hence we can again heuristic estimate the perpendicular diffusion coefficient for a plateau regime as

$$D_{P\perp} \sim \frac{v_{||}}{v_T}d^2\nu_{ef} \sim \frac{v_{||}}{v_T}\frac{v_d^2}{\nu_{ef}} \sim \frac{v_{||}}{v_T}\frac{v_T^2\rho^2/R^2}{v_{||}/Rq} = \frac{qv_T}{R}\rho^2. \tag{1.35}$$

The transport is called plateau because the $D_{P\perp}$ is not a function of ν and the graph $D_{P\perp}(\nu)$ is flat as we can see in Fig.1.2. We assumed the large aspect-ratio but in real tokamaks is not true that $\epsilon \ll 1$ and the plateau domain exists only on a very narrow region of collisionality.

The neoclassical perpendicular diffusion coefficients was derived by considering the random walk behaviour of the particles and they are proportional $\rho^2\nu$. Since $\rho \sim \sqrt{m}$ and $\nu \sim 1/sqrtm$ and hence $\rho^2\nu \sim \sqrt{m}$ the diffusion coefficient for ions is larger than for electrons. But in an axisymmetric configuration it should be equal. In fact the experimentally founded diffusion coefficients are still few times larger than the neoclassical diffusion coefficients for ions. This fact indicates that the electron diffusion is not neoclassical. We obviously must take the turbulent diffusion/transport caused by fluctuations in the plasma into account.

1.6 Turbulent transport [8], [42]

In the next text the temperature of the plasma is in eV, or $k = 1$. In the plasma the electrostatic or electromagnetic fluctuations are expected to appear as the non-linearly saturated state of microinstabilities in the plasma. Any oscillating quantity $\delta\boldsymbol{g}$ can be written as

$$\delta\boldsymbol{g} = \delta\boldsymbol{g}_0 \exp[i(\boldsymbol{kr} - \omega t)], \tag{1.36}$$

where $\delta\boldsymbol{g}_0$ is the complex amplitude and $\exp[i(\boldsymbol{kr} - \omega t)]$ is the phase of the oscillating quantity $\delta\boldsymbol{g}$. If we have the density fluctuations δn, the temperature fluctuations δT or the electric field fluctuations $\delta\boldsymbol{E}$ in the plasma then it gives a radial particle flux

$$\Gamma_\perp = \langle \delta n \frac{\delta E_\perp}{B} \rangle, \tag{1.37}$$

or a radial energy flux

$$q_\perp = \frac{3}{2}n_0\langle \delta T \frac{\delta E_\perp}{B} \rangle, \tag{1.38}$$

where n_0 is the equilibrium density and $\langle\rangle$ is an average over a flux surface. Or the radial magnetic fluctuations $\delta\boldsymbol{B}$ combines with the parallel velocity fluctuations $\delta v_{||}$ to give a particle flux

$$\Gamma = \frac{n_0}{B_0}\langle \delta v_{||} \delta B_r \rangle, \tag{1.39}$$

where B_0 is the equilibrium magnetic field. The amplitudes and phases of fluctuations δn, δT and electric potential fluctuations $\delta\phi$ at the plasma edge (see chapter 3) can be measured by Langmuir probes (see chapter 4). The relative fluctuations $\delta n/n$, $\delta T_e/T_e$ and $e\delta\phi/T_e$ rise rapidly towards the plasma edge where reaches values ≈ 0.5. The magnetic fluctuations are negligible at the plasma edge. The edge value $\delta B/B$ is typically ≈ 0.0001. This fluctuations have a characteristic frequencies $\approx 100kHz$.

If this fluctuations are account for the observed plasma transport there should be a correlation between the level of fluctuations and confinement time τ_E. At the edge of the plasma we can compare the fluxes calculated from the fluctuation measurements and a measured fluxes. By using the probes a precise analysis of the relationship between electrostatic fluctuations and observed transport is possible. A magnitudes and scalings followed from particle fluxes calculated from the fluctuation measurements have agreed with the observed transport for example in tokamak TEXT (USA) [8] and it indicates that electrostatic fluctuations provide the dominant transport mechanism.

The turbulent-induced transport can be described like this. A instability release the free energy. This energy drives a steady level of fluctuations. And this fluctuations results in a radial perpendicular transport of particles and energy. (The plasma is in a state of turbulence if it is so strongly excited that a continuous spectrum of frequencies is present.)

Transport due to electrostatic potential fluctuations $\delta\boldsymbol{\phi}$: The oscillating quantity can be written in terms of their Fourier components

$$\delta\phi(t) = \sum\nolimits_k (\delta\phi_k(t)) = \sum\nolimits_k (\delta\phi_{k0}(t)\exp(i\boldsymbol{kr})), \tag{1.40}$$

where $\boldsymbol{k}$ is the wave vector. Because of $\boldsymbol{E}\times\boldsymbol{B}$ drift, there is

$$\delta v_{\perp k} = |\delta\boldsymbol{v}_{\perp k}| = \left|\frac{-\nabla\delta\phi_k \times \boldsymbol{B}}{B^2}\right| = \left|-\frac{\boldsymbol{k}\times\boldsymbol{B}}{B^2}\delta\phi_k\right| = \frac{k_\perp \delta\phi_k}{B}. \tag{1.41}$$

For the correlation time τ_k for which the $\delta v_{\perp k}$ persists a displacement of part of the plasma is $\delta v_{\perp k}\tau_k$. Thus we can do a random walk estimate for the perpendicular (cross-field) turbulent diffusion coefficient

$$D_{T\perp} \simeq \sum\nolimits_k \left(\frac{(\delta v_{\perp k}\tau_k)^2}{\tau_k}\right) = \sum\nolimits_k (\delta v_{\perp k}^2 \tau_k). \tag{1.42}$$

τ_k is the shortest time from different possible times :the time for collisions to change the particle orbit, the time for drifts to carry particles over a perpendicular wavelength, the time for a particle to move along a parallel wavelength of the fluctuations, or the time variation of the fluctuation. If it is the time for $\boldsymbol{E}\times\boldsymbol{B}$ drift to carry particle over a perpendicular wavelength $\tau_k \simeq 1/\omega_k = 1/(\delta v_{\perp k} k_\perp)$

then the perpendicular turbulent diffusion coefficient becomes linear in electric potential fluctuations

$$D_{T\perp} \simeq \sum_k \left(\delta v_{\perp k}^2 \frac{1}{\delta v_{\perp k} k_\perp} \right) = \sum_k \left(\frac{\delta \phi_k}{B} \right). \tag{1.43}$$

Transport due to magnetic fluctuations $\delta \boldsymbol{B}$: The magnetic fluctuations $\delta \boldsymbol{B}$ can destroy the set of nested toroidal flux surfaces and then the magnetic field lines no longer map out flux surface but follow a space filling trajectory. Then thermal motion of particles along this magnetic field lines can lead to perpendicular (radial) transport of particles and energy.

Velocity shear and reduction of the turbulent transport: It is experimentally observed that improved confinement in tokamaks is associated with a strongly radially varying radial electric field E_{Rad}. It is evident mainly in the vicinity of the spontaneously generated edge transport barriers during the H-mode or internal transport barriers. This varying radial electric field can be also generated by applying a voltage to the electrodes **??** at the SOL or applying additional heating or by flows driven by the turbulence itself. The varying electric field causes the E × B drift velocity shear $\mathrm{d}v_{Pol}/\mathrm{d}r$ as is illustrated in Fig.(1.7).

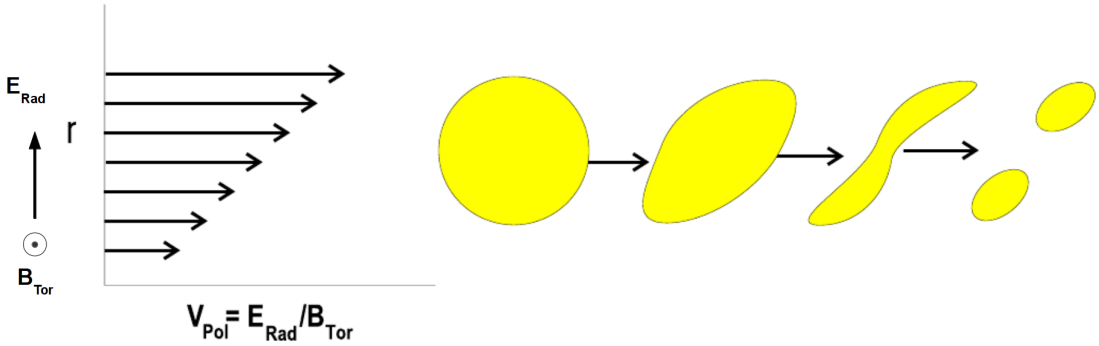

Figure 1.7: A demonstration of the destruction of turbulent plasma structures by radial shear of the poloidal (or toroidal) velocity. The arrows does not mean the movement of the structures they means the time evolution of them. The movement of the structures is also radial. [42] (modified)

It is generally agreed that turbulent radial transport of plasma is closely connected with existence of turbulent structures (they are called blobs and they will be described later in 3.2). Due to this velocity shear the turbulent structures elongate in the poloidal or toroidal direction and their radial correlation length is shorten. This way the radial turbulent transport is reduced and confinement of the particle and thermal energy improved. In principle the shear of the toroidal velocity $\mathrm{d}v_{||}/\mathrm{d}r$ can also destroy the turbulent structures but in this direction the structures are ≈ 100 times longer [10] and speeds are larger only ≈ 10 times. For example in the tokamak MAST in United Kingdom the typical values of poloidal velocities was [18] (2009) $\approx 5 - 10$km/s and toroidal velocities of $100 - 200$km/s in the plasma core . Therefore this effect is much weaker than that in case of the shear of the poloidal velocity. The radially varying radial electric field can also modify classical and neoclassical transport.

1.7 Plasma-surface interaction

One of the most important phenomena in the edge of the plasma is interaction of the plasma and a surface. This releases impurities from the material surfaces facing the plasma (or the helium in a reactor). The most easily released impurities are those adsorbed on the surfaces but there are also bulk impurities migrated to the surface. and desorbed thermally or by impact of particles from the plasma. The most problematic are the impurities of high atomic number. During the plasma start-up phase at low temperatures they become excited and due to subsequent line radiation there is the significant radiative power loss (up to 100 %). After further increase of the temperature they become highly ionized and produce many electrons which dilute the fuel. At high concentrations the impurities prevent the plasma heating.

The tokamak plasma is confined within closed magnetic flux surfaces. The Last Closed Flux Surface (LCFS) determines a boundary. The plasma in the boundary layer outside the LCFS flows along the $\boldsymbol{B}$ and then interacts with a solid surface where the ions may be neutralized and released back to the plasma with subsequent repeated ionization. The shape of the LCFS is determined by the external magnetic fields. With a divertor the solid surface is not in contact with the LCFS, but with limiter without divertor the solid surface is directly in contact with the LCFS as illustrated in Fig.1.8. Therefore by using the divertor the plasma impurity level is lower than by using only the limiter.

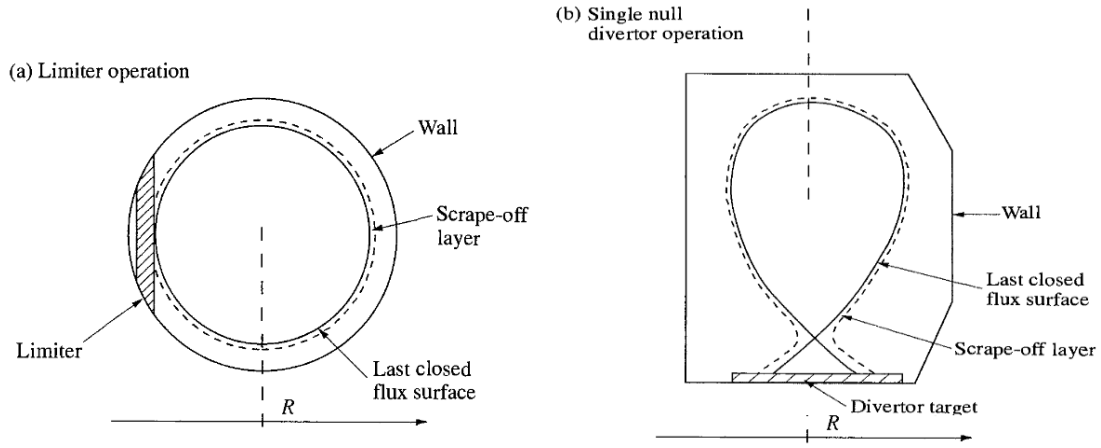

Figure 1.8: Poloidal cross-section of the LCFS (a) with a limiter and (b) with a divertor. [8]

1.8 The plasma sheath

The electrons in the plasma have higher mobility than ions, therefore a material inserted into the vicinity of the plasma charge negatively. This negative charge creates a drop of the plasma potential called the plasma sheath. The plasma sheath is a narrow area near the surface, its width being several Debye lengths. There is an electric field which equalize the electron flow and the ion flow (let's suppose a single charged ions, for example in the deuterium plasma). And

hence the total current density to material surface equals zero

$$j_i + j_e = en_{im}v_{im} - en_{em}v_{em} = 0, \tag{1.44}$$

where n_{im}, v_{im} and n_{em}, v_{em} are the ion density, mean ion velocity, electron density and mean electron velocity at the material surface respectively and e is the proton charge.

Only a small part of the potential drop extends further into the plasma beyond the sheath and this area is called presheath. A typical spatial variation of electric potential, ion velocity and the ion and electron densities across the plasma sheath (and presheath) is illustrated in Fig.1.9.

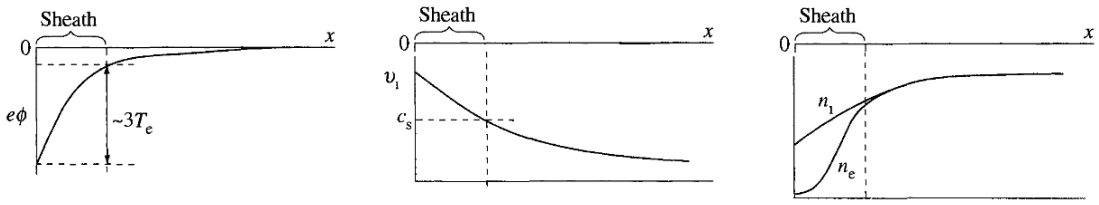

Figure 1.9: Spatial variation of electric potential, ion velocity and the ion and electron densities across the plasma sheath. [8]

Let's now compute the size of the potential drop in the vicinity of the surface and express the temperature in eV, that is the Boltzman constant $k = 1$, and $eV \approx 1.6 \cdot 10^{-19}J$. Defining the electric potential to be zero at the sheath edge $\phi_s = 0$, the electron density as a function of electric potential ϕ in the plasma is

$$n_e(\phi) = n_{es} \exp\left(\frac{e\phi}{T_e}\right), \tag{1.45}$$

where n_{es} is the electron density at the sheath edge. We find it by integrating the electron distribution function $f(v) = A\exp[-(mv^2/2 - e\phi)/T_e]$ over all v. For the ions we have the energy conservation law

$$\frac{1}{2}m_i v_i^2 + e\phi = \frac{1}{2}m_i v_{is} + 0, \tag{1.46}$$

where v_{is} is the mean ion velocity at the sheath edge. From this equation we can express the v_i. The ion flux is constant $n_i v_i = n_{is}v_{is}$, therefore $n_i(\phi)$ is given by

$$n_i(\phi) = n_{is}\frac{v_{is}}{v_i} = n_{is}\sqrt{\frac{\frac{1}{2}m_i v_{is}^2}{\frac{1}{2}m_i v_{is}^2 - e\phi}}, \tag{1.47}$$

where n_{is} is the ion density at the sheath edge which is approximately equal to the ion density outside the sheath and presheath. Substituting for n_e and n_i in the Poisson's equation we have

$$\frac{\mathrm{d}\phi}{\mathrm{d}x} = \frac{e}{\epsilon_0}(n_e - n_i) = \frac{n_{is}e}{\epsilon_0}\left[\exp\left(\frac{e\phi}{T_e}\right) - \sqrt{\left(\frac{\frac{1}{2}m_i v_{is}^2}{\frac{1}{2}m_i v_{is}^2 - e\phi}\right)}\right], \tag{1.48}$$

where ϵ_0 is permittivity of free space. In the immediate vicinity of the sheath edge the electric potential $\phi \to 0$. Thus by using the first two terms of the Taylor series of the exponential and square root function, equation (1.48) becomes

$$\frac{\mathrm{d}\phi}{\mathrm{d}x} \approx \frac{n_{is}e}{\epsilon_0}\left[\left(1 + \frac{e\phi}{T_e}\right) - \left(1 - \frac{1}{2}\frac{e\phi}{\frac{1}{2}m_i v_{is}^2 - e\phi}\right)\right] \approx \left(1 - \frac{T_e/m_i}{v_{is}^2}\frac{\phi}{\lambda_D^2}\right), \tag{1.49}$$

where

$$\lambda_D \approx \sqrt{\frac{\epsilon_0 T_e}{n_{is} e^2}}, \tag{1.50}$$

is the Debye length at the sheath edge where $n_{is} \approx n_{es}$. In the immediate vicinity of the sheath edge is the electric potential almost equal to the plasma potential outside the sheath and preseath and $\mathrm{d}\phi/\mathrm{d}x \to 0$. It requires

$$v_{is} \simeq \sqrt{\frac{T_e}{m_i}}. \tag{1.51}$$

The generalization of equation (1.51) with considering the ion temperature is

$$v_{is} = c_s \simeq \sqrt{\frac{T_e + T_i}{m_i}}, \tag{1.52}$$

where c_s is the sound speed in the plasma and the plasma enters the sheath at this speed.

The ion or electron current density into the sheath is equal to the ion or electron current density at the material surface.

$$j_i = e n_{im} v_{im} = e n_{is} c_s, \tag{1.53}$$

$$j_e = -e n_{em} v_{em} = -e \frac{1}{4} n_e(\phi_m) \sqrt{\frac{8T_e}{\pi m_e}}, \tag{1.54}$$

where ϕ_m is the electric potential at the material surface. The electrons are in the sheath in a retarding electric field and their velocity distribution remains Maxwellian but with a reduced density and temperature. From this Maxwellian distribution in the immediate vicinity of the material surface only the high energy tail of the electrons arrives at the surface. On the other hand the electric field in the sheath is accelerating for the ions and substantially disturbs Maxwellian velocity distribution. The ion velocity distribution in the immediate vicinity of the material surface is non-Maxwellian and we can consider it very approximately as accelerated and truncated Maxwellian velocity distribution.

Substitution of equations (1.53) and (1.54) into the equation (1.44) gives

$$\frac{1}{4} \exp\left(\frac{e\phi_m}{T_e}\right) \sqrt{\frac{8T_e}{\pi m_e}} \simeq \sqrt{\frac{T_e + T_i}{m_i}}, \tag{1.55}$$

and so ϕ_m is given by

$$\phi_m \simeq -\frac{T_e}{e} \frac{1}{2} \ln\left[\frac{m_i/m_e}{2\pi(1 + T_i/T_e)}\right] \qquad T_e \text{ in eV}. \tag{1.56}$$

For a deuterium plasma and $T_e = T_i$, we have $\phi_m \approx -2.8(T_e/e)$, T_e in eV. The difference between the electric potential at the material surface and the electric potential at the sheath edge $\phi_m - \phi_s = \phi_m$ is called **the floating potential V_f** . Electron and mainly ion impact on the surface cause the secondary electron emission from the surface with the total secondary electron emission coefficient δ. Considering it the floating potential is (T_e in eV).

$$V_f = -\frac{T_e}{e}\alpha \simeq \frac{T_e}{e} \frac{1}{2} \ln\left[\frac{2\pi}{(1-\delta^2)} \left(\frac{m_e}{m_i}\right) \left(1 + \frac{T_i}{T_e}\right)\right]. \tag{1.57}$$

Because of space charge effects the effective value of δ cannot exceed the value ≈ 0.8. If the plasma is in contact with a surface at a fixed potential, the plasma potential ϕ_p is determined by the floating potential. Often we consider $\phi_p \approx \phi_s$. The electric field in the boundary can have a significant effect on transport in the plasma.

The plasma sheath also influences the energy flux P from the plasma to the surface. Considering the Maxwellian ion and electron velocity distribution (the kinetic energy per one particle is $\approx 2T_e$ or $2T_i$) we have

$$\begin{aligned} P &= 2T_e(n_{em}v_{em})\frac{1}{1-\delta} + 2T_i(n_{im}v_{im}) + eV_f(n_{im}v_{im}) \simeq \\ &\simeq 2T_e(n_{es}c_s)\frac{1}{1-\delta} + 2T_i(n_{es}c_s) + eV_f(n_{es}c_s) \simeq \\ &\simeq \left[2\frac{T_i}{T_e} + \frac{2}{1-\delta} - \frac{eV_f}{T_e}\right](n_{es}c_s)T_e \simeq \gamma_s \Gamma T_e, \end{aligned} \tag{1.58}$$

where Γ is the incident particle flux and γ_s is the sheath heat transmission factor, for $T_i = T_e$, $\delta = 0$ and hydrogen plasma $\gamma_s \approx 6.5$.

1.9 The scrape-off layer

The scrape-off layer (SOL) is the region outboard of the LCFS. The parallel convective flux $\Gamma_{||}$ in the SOL along the open magnetic field lines towards the limiter or divertor is balanced by perpendicular diffusive flux $\Gamma_\perp$ from the confined plasma into the SOL across the magnetic field lines. The diffusion along the magnetic field lines can be neglected. This is schematically illustrated in Fig.1.10. L_c is called the connection length, $D_\perp$ is perpendicular turbulent diffusion coefficient and c_s is the sound speed in the plasma. The distance along the magnetic field in the SOL between two points of contacts with the solid surface is then $2L_c$.

In the steady state, provided there are not any sources or sinks for particles in the SOL we can write [61]

$$\frac{\mathrm{d}}{\mathrm{d}r}\left[-D_\perp \frac{\mathrm{d}n}{\mathrm{d}r} + nv_\perp\right] + \frac{n}{\tau_{||}} = 0, \tag{1.59}$$

where parallel loss time $\tau_{||}$ can be estimated as $\tau_{||} \approx 2L_c n/(2n_{es}c_s) \approx 2L_c/c_s$. Assuming the experimentally observed exponential decay,

$$n(r) = n(a)\exp\left[-\frac{r-a}{\lambda_n}\right], \tag{1.60}$$

where λ_n is the scrape off thickness for density and a is the minor radius at the limiter or LCFS, and assuming that $D_\perp$, $v_\perp$ and c_s are independent of radius, leads after solving the resulting differential equation for λ_n to expression:

$$\lambda_n^2 - \lambda_n v_\perp \tau_{||} - D_\perp \tau_{||} = 0. \tag{1.61}$$

Equation (1.61) has a general solution:

$$\lambda_n = \frac{v_\perp \tau_{||}}{2} \pm \sqrt{D_\perp \tau_{||} + \left(\frac{v_{||}\tau_{||}}{2}\right)^2}. \tag{1.62}$$

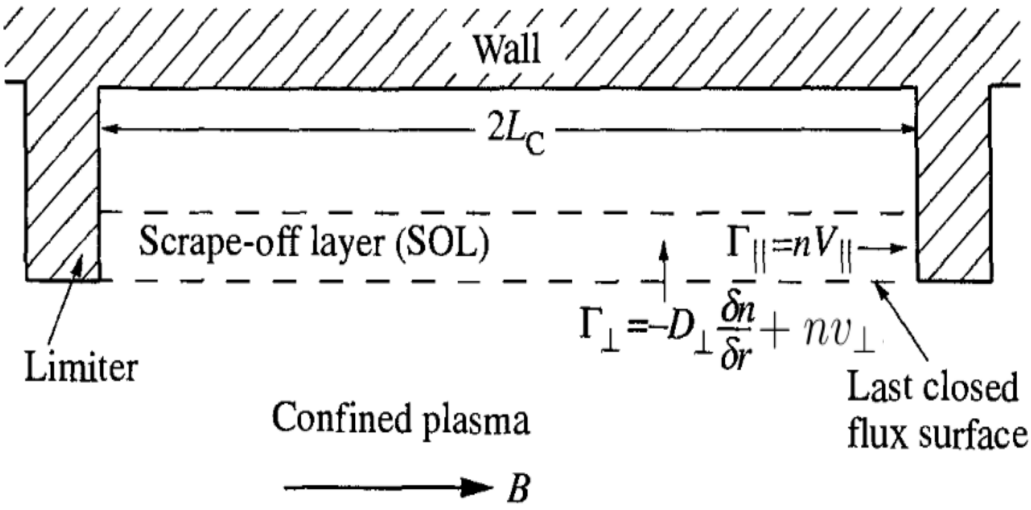

Figure 1.10: Schematic diagram of the SOL which has been straightened out. In place of the limiter there can be divertor. $V_{||} \sim c_s$. [8]

For purely diffusive perpendicular/radial transport equation (1.62) leads to the often employed equation:

$$\lambda_n = \sqrt{\frac{2L_c D_\perp}{c_s}}. \tag{1.63}$$

Similarly we can obtain the electron temperature profile from the electron heat balance

$$T_e(r) = T_e(a) \exp\left[-\frac{r-a}{\lambda_{T_e}}\right], \tag{1.64}$$

and λ_{T_e} is the scrape off thickness for electron temperature. We can measure the scrape off thickness for density and electron temperature with electrical probes, if the impurity content is small. Their typical values are $\approx 10mm$. Then we can deduce $D_\perp$ from the equation (1.62).

We can also estimate the expected value of the density at the LCFS $n(a)$. The total particle flux diffusing out from the confined plasma to the SOL between two limiters is

$$\Gamma_n \simeq \frac{\langle n \rangle V_p}{\tau_p}, \tag{1.65}$$

where τ_p is a particle replacement time, $\langle n \rangle$ is the average plasma density and V_p is the plasma volume. It is equal to the total particle flux Γ_L to both limiters in the area between them

$$\Gamma_n \simeq \Gamma_L \simeq 2\left(2\pi a \int_a^\infty n(a) \exp\left[-\frac{r-a}{\lambda_n}\right] c_s \mathrm{d}r\right) = 4\pi a\ n(a) \lambda_n c_s, \tag{1.66}$$

thus [8]

$$n(a) \simeq \frac{\langle n \rangle V_p}{\tau_p} \frac{1}{4\pi a \lambda_n c_s}. \tag{1.67}$$

Such a calculations are valid only for limiter tokamaks. For divertor tokamaks it is more complex.

1.10 Goals of the thesis

An understanding of the physics governing transport at the boundary of magnetized plasmas is crucial because the transport (which is mainly turbulent) in the outermost plasma region in contact with material surfaces regulates the particle and heat loads on the plasma-facing components. And the control of this transport is very important for particle and heat confinements in tokamaks and other magnetized plasma experiments (linear devices, reversed field pinches, stellarators). Only the intermittent turbulent structures account for more than 50% [11] of the radial plasma transport towards the material surfaces.
The turbulences cause the losses of the particles and heat from the central plasma, thus feature very high risk of damaging tokamak first wall, and other plasma-facing components. In the same time, impurities released by these components spread through the boundary region into central plasma, cooling it down by their radiation and decreasing the fusion rate due to dilution of the fuel.

Turbulence is all around us. The wind gusted down the streets or air flowing in and out of our legs is turbulent. Also the liquid core of the earth is turbulent. Turbulence dictates the weather, controls the drag on aeroplanes, cars and bridges. Richard Feynman called turbulence "the most important unsolved problem of classical physics" [4].
The mathematical description of turbulence is complex. Even though the governing equations have been known since 1845 , we can still predict with relative certainty only a little. We can take a non-statistical approach with deterministic governing equations but the variables it predicts are chaotic. Or we can take a statistical approach, then the quantities we are interested are non-random and they are well reproducible in any experiment. However in this case we cannot find a closed set of equations for describing them. There always is more unknowns than equations and to close the equation system we need to introduce some additional "ad hoc" (for a specific problem) information. This is the closure problem of turbulence [9].

The main targets of the thesis are:

- to describe the turbulent transport in the boundary of tokamak plasma;
- to describe the Langmuir and Ball-pen probes which measure that turbulent transport;
- to describe the numerical code ESEL (ElectroStatic Edge-soL; SOL means Scrape Off Layer) which simulate that turbulent transport;
- to use the results acquired from the ESEL and the probes and process them;
- to compare and discuss the results and make a conclusions.

Specially this thesis should provide a current picture of the possibilities of the numerical code ESEL to describe the transport in the scrape-off layer of the tokamak plasma. In present this numerical code is very popular in plasma physics but his development is not at the end because the understanding of particle and energy transport in tokamak boundary is still not complete. The first part of the

thesis deals with the little detailed description of the physics beyond the ESEL code and measurements using the Langmuir and ball-pen probes.

2. The fast reciprocating Probes

2.1 The reciprocating manipulator [38]

Probes have been extensively used in magnetic confinement devices in the past 50 years , and also the experimental data used in this thesis are mainly acquired by a probes. As the performance of the devices increased, fast reciprocating probe manipulators in the 1980s were developed to cope with the big heat and particle loads. If the movement of the probe pins into the plasma is fast, the damage of the probe pins due to the high heat fluxes experienced in the plasma is reduced. Originally the fast probe systems were all steel or tungsten construction with tungsten tips. The metal erodes by chemical or physical sputtering and results in the release of high Z (the proton number) atoms into the plasma core what reduces device performance. Therefore ceramic and graphite designs with low Z atoms were developed. Design for ASDEX tokamak is mostly graphite and boron nitride construction. Because of great varying of the density and temperature of the plasma across the SOL plasma the probe measurements require high spatial resolution which can be provided by probes. The reciprocating manipulators has many requirements such as:

- remote operation due to the presence of radiation, high voltage, time constraints and radio frequency field during tokamak operations;
- easy design, ease of maintenance and tips and head replacement;
- high speed reciprocation (up to 3m/s);
- high heat flux capability (up to 10MW/m^2);
- enough internal connections due to large amount of probe pins.

The probe assembly consists of two main parts: the probe (in this subhead for the probes in common meaning the word pins is used) itself and slow and fast drive mechanism, all mounted on some mechanical support (to prevent a mechanical vibrations) as shown in Fig.(2.1). Bellows absorb machine vibration and expansion.

Drive mechanism:
The slow and fast drive mechanism is a two-stage pneumatic system and it is illustrated in Fig.(2.1). By the slow drive mechanism the probe moves to a stand-by position, close to the plasma while not exposed to it. Then, during the discharge the probe reciprocates from this position into the plasma and back rapidly by the fast drive mechanism. In the case of the COMPASS tokamak the slow motion is powered by a compressed air driven motor (or manually) and his extent is around 61cm and the fast reciprocating motion is driven by a pneumatic piston under helium pressure and his extend is no more than 6cm [43]. The all motion slow and fast can be fully programmed from the control system. The speed of the fast motion is determined by a sound speed in the used drive gas. In the case of the COMPASS tokamak this speed is no more than about 1.3m/s with maximum acceleration 5 times gravimetric acceleration [43].

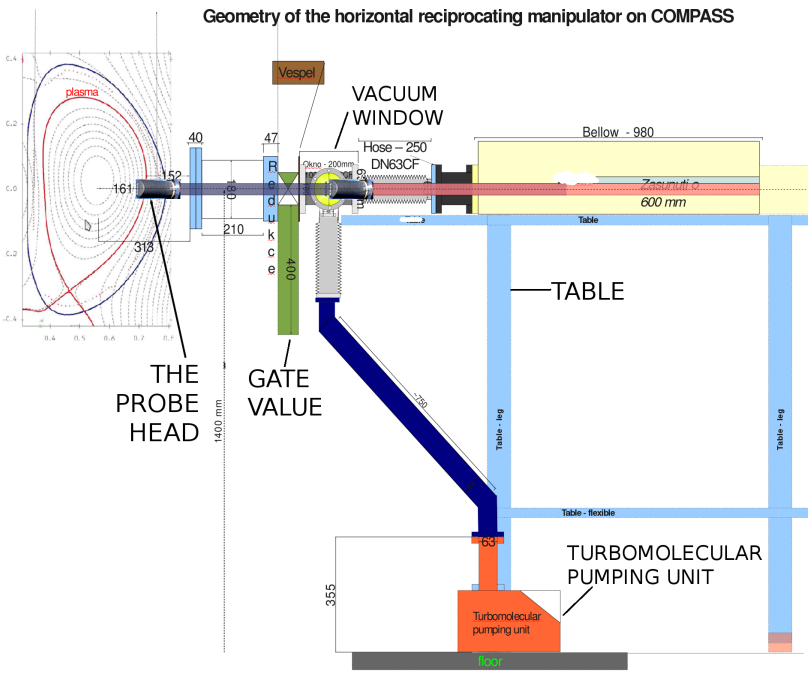

Figure 2.1: Horizontal reciprocating manipulator on COMPASS. [59]

The probe itself is composed of the probe head, shaft and rear feedthrough as shown in Fig.(2.2). The whole probe should be lightweight to maximize acceleration and to reduce forces generated during operation.

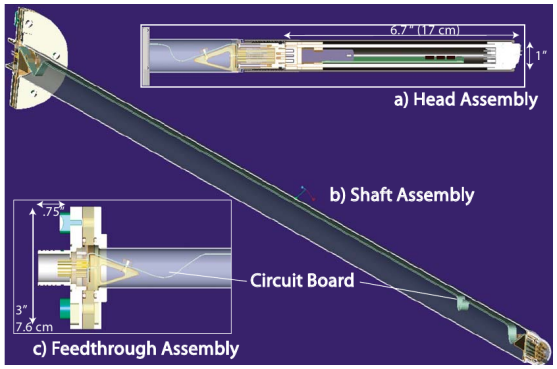

Figure 2.2: Head and shaft assembly used for NSTX tokamak. [38]

Probe head:
The purpose of the probe head (shown in Fig.(2.3) and Fig.(2.4)) is to shield and hold tips. The tips which were used for obtaining experimental data used in this thesis are known as Langmuir probes and Ball-pen probes and they will be described in next two subheads. The probe head should be replaceable due to erosion, arcing damage and thermal stress after each exposing to the plasma. The whole probe head except a small boron nitride front cover is protected against high heat fluxes by a graphite shroud which is screwed onto the shaft. The graphite is conductor and boron nitride front cover is not protected by it to prevent graphite from short circuiting the plasma. The front boron nitride piece is often heavily damaged by the plasma so it should be easily extracted often merely removing the graphite shroud and unscrewing it. Tip replacement is gen-

erally achieved by removing the front boron nitride cover and unscrewing the tips from the rods. The probe head is held by screws and graphite shroud. Electrical connection in the probe head are made via pin-socket pairs held in the back and front Vespel matrix (Fig.(2.4)). This Vespel matrices foms back and front connectors. Vespel is generally made from polyimide. Polyimide is lightweight, strong, high temperature ($\approx 300°C$) resistive slightly hygroscopic (water from the air is released during bakeout) polymer which has very low outgassing rate.

Shaft and feedthroughs:
The purpose of the shaft is to transmit the signal from the pins traditionally using coaxial cables. The common material for the shaft is Inconel. The shaft is electrically and mechanically integrated unit and can be easily rotated at the rear end by loosening the screws.

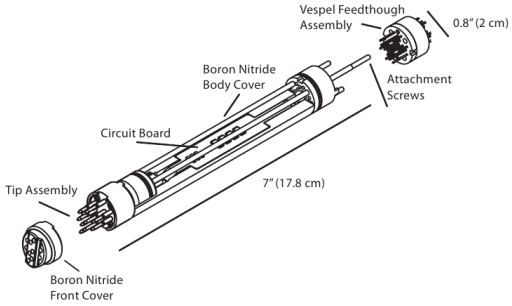

Figure 2.3: Computer generated graphics showing a probe head overview. [38]

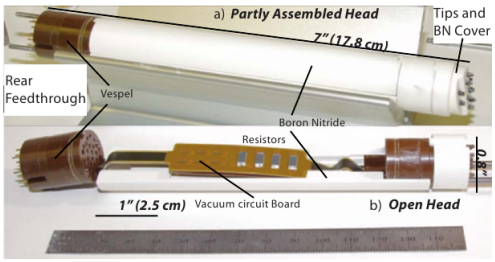

Figure 2.4: (Color online) Probe head assembly: (a) closed probe head and (b) open probe head. [38]

2.2 Langmuir probes [8]

In it's simplest form the Langmuir probe consist of a single electrode. If we apply a voltage V to the probe with respect to the vessel and measure the current I_{pr} to a probe we can obtain the current-voltage (I-V) characteristic. One example of such characteristic is illustrated in Fig.2.5.

$$V = \phi_{pr} - \phi_{\text{vessel}}, \tag{2.1}$$

where $\phi_{pr} = V$ is the electric potential at the probe surface and ϕ_{vessel} is the electric potential at the vessel surface.

The theory of Langmuir probes is based on the theory of the plasma sheath (see section 1.8). The mentioned surface is now the surface of the probe. From the equations (1.44), (1.53), (1.54) we have (T_e in eV)

$$\begin{aligned} j_{ip}(\phi_{pr} = V) &= j_{is} = j_{ip}(\phi_{pr} = V_f) = -j_{ep}(\phi_{pr} = V_f) = \\ &= e\frac{1}{4}n_{es}\sqrt{\frac{8T_e}{\pi m_e}}\exp\left(\frac{eV_f}{T_e}\right), \end{aligned} \tag{2.2}$$

$$\begin{aligned} j_{ep}(\phi_{pr} = V) &= -e\frac{1}{4}n_{es}\exp\left(\frac{eV}{T_e}\right)\sqrt{\frac{8T_e}{\pi m_e}} = \\ &= -e\frac{1}{4}n_{es}\sqrt{\frac{8T_e}{\pi m_e}}\exp\left(\frac{e(V-V_f)}{T_e}\right)\exp\left(\frac{eV_f}{T_e}\right), \end{aligned} \tag{2.3}$$

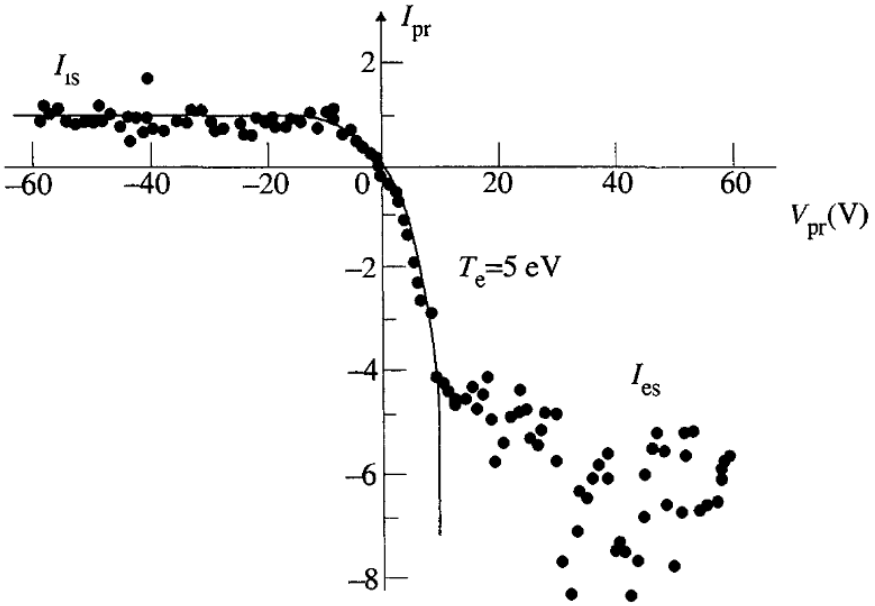

Figure 2.5: Single Langmuir probe I-V characteristic . [8]

$$\begin{aligned} I_{pr} &= (j_{ip} - j_{ep})A = (j_{is}A)\left(1 - \exp\left(\frac{e(V - V_f)}{T_e}\right)\right), \\ V &= V_f + V_{pr} < \phi_p, \end{aligned} \tag{2.4}$$

where j_{ip}, j_{ep} is the density of the ion and electron current respectively to a probe, j_{is} is the density of the ion saturation current to a probe, A is the the effective projected surface area of the probe for electron and ions (it is assumed it is the same for electrons and for ions) and ϕ_p is the plasma potential. If the probe dimensions are sufficiently large compared to the gyro-radii of the ions and electrons and to the Debye length, we can approximately write

$$A \simeq \int\limits_{S_{\text{probe}}} \frac{1}{B}\boldsymbol{B}.\mathrm{d}\boldsymbol{S}. \tag{2.5}$$

If the probe is biased sufficiently negatively the electron current equals zero and $I_{pr} = j_{is}A = I_{is}$ as we can see from equation 2.5 for $V \to -\infty$. I_{is} is independent of voltage because the ion flux to the probe is simply determined by the ion flux across the sheath edge at the ion sound speed. For $V = V_f$, $I_{pr} = 0$. The equation (2.5) is applicable only for $V < \phi_p$. In the case that $V = \phi_p$ there is no plasma sheath and

$$\begin{aligned} I_{pr} &= \left(\frac{1}{4}en_i\sqrt{\frac{8T_i}{\pi m_i}} - \frac{1}{4}en_e\sqrt{\frac{8T_e}{\pi m_e}}\right)A \simeq -\frac{1}{4}en_e\sqrt{\frac{8T_e}{\pi m_e}}A = I_{es}, \\ V &= \phi_p, \end{aligned} \tag{2.6}$$

where I_{es} is the electron saturation current. The electrons flow to the probe with a thermal velocity. When the probe is biased more positively, the electrons are attracted and $I_{pr} < I_{es}$ but not much because of space charge effects. We can derive the electron temperature (and also the V_f and I_{is}) from the fit of the ion branch ($V_{pr} \leq V_f$) of a I-V characteristic according to equation (2.5). And then

we can derive the electron density at the sheath edge from the equation (1.53), (2.2) and the assumption $T_e = T_i$ as

$$n_{es} \simeq n_{is} = \frac{I_{is}}{e^{3/2}A}\sqrt{\frac{m_i}{2T_e}}. \tag{2.7}$$

The electron (and ion) density far away from the material surface and the plasma sheath equals $n_e \approx 0.5 n_{es}$ [61], thus for general T_i and T_e and isothermal electrons and ions (the sound speed is simply $\sqrt{\frac{T_e+T_i}{m_i}}$) we have

$$n_e \simeq 2\frac{I_{is}}{e^{3/2}A}\sqrt{\frac{m_i}{T_e+T_i}}, \tag{2.8}$$

where T_e, T_i are in eV. Langmuir probes can be mounted on fast reciprocating drives but their use is limited to the plasma edge because of the large power fluxes in the confined plasma.

For a cylindrical Langmuir probe in a deuterium plasma with $T_e = T_i$ we can write

$$V_f = \phi_p - \frac{T_e}{e}\ln\left|\frac{I_{es}}{I_{is}}\right| \approx \phi_p - 2.8\frac{T_e}{e}, \qquad T_e \text{ in eV}. \tag{2.9}$$

And thus we can derive the plasma potential.

2.3 Ball-pen probes [53]

The Ball-pen probe is similar to the Katsumata probe [52]. It is simple modification of a Langmuir probe in strongly magnetized plasma. The ration $R = |I_{es}/I_{is}|$ in the equation (2.10) can not be directly experimentally obtained and it depends on many quantities. It would be suitable if this ratio was equal to one. In this case it would be possible to measure plasma potential directly, because then $V_f = \phi_p$. And it is almost possible with the ball-pen probe which is illustrated in Fig.(2.6).

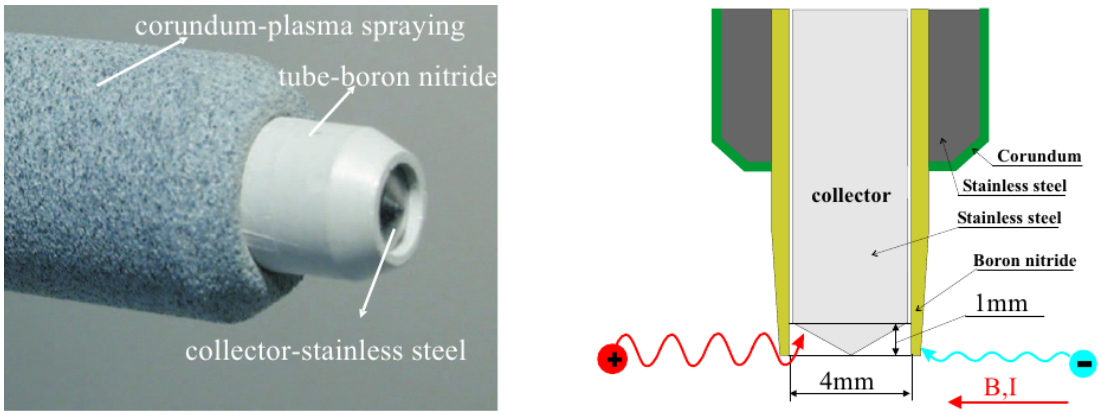

Figure 2.6: Photograph of the ball-pen probe (left) and her scheme (right). [53]

The conically shaped conducting collector is inserted inside an isolating tube made often of boron nitride. The isolating tube provides a magnetic shadow for the conducting collector and also protection from high energy flux. The magnetic

field is perpendicular to both collector and tube. The collector is movable inside the tube. It can be completely shielded or partially exposed to the plasma (and act as Langmuir probe). In the ideal case when the collector is hidden inside the tube, only ions can reach the collector surface because they have a sufficiently large Larmor radius. The electron current is almost equal to zero and $R << 1$. When the collector is close to the plasma, the electron current and the ratio R is larger than in the previous case. At a certain position of the collector, it is expected to be $I_{es} = -I_{is}$, $R = 1$ and $V_f = \phi_p$. But it is ideal case. The reality is a little different. As we can see from the experimental results performed at the GOLEM tokamak (previously CASTOR) in Czech Republic in Fig.(2.7).

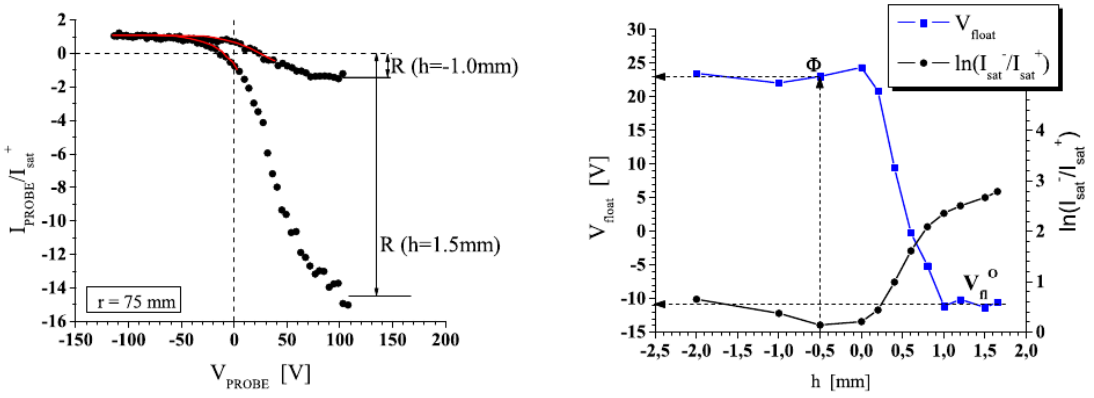

Figure 2.7: I-V characteristic for 2 different collector positions (left). The collector position h is negative if the collector is hidden inside the shielding tube. And the $\ln(R)$ and V_f as a function of the h (right). V_{fl}^0 is the floating potential measured in the operation as a Langmuir probe. When the collector is hidden the probe potential ($\approx \phi_p = \phi$) is approximately constant. The reason is not clear. [53]

The absolute value of the electron current is always higher than the ion current even when the collector is deeply inside the shielding tube. The electrons are present even in the shadow of the shielding tube. It is probably due to $\boldsymbol{E} \times \boldsymbol{B}$ drift. Nevertheless the $\ln(R)$ can attain a value close to zero (≈ 0.1 in Fig.(2.7), for $h \approx -0.5mm$) and the difference between the plasma potential ϕ_p and floating potential V_f of the probe is small. It was found experimentally [54] from a measurements in the tokamak ASDEX Upgrade that for the ball-pen probe

$$V_f = \phi_p - (0.6 \pm 0.5)\frac{T_e}{e}, \qquad T_e \text{ in eV}. \tag{2.10}$$

The comparison with the data obtained by edge Thomson scattering [54] demonstrated such functionality.

3. ESEL code and other codes

3.1 Interchange instability [60]

An instability is motion which decreases the free energy available in the plasma and brings the plasma closer to true thermodynamic equilibrium. In the true or perfect thermodynamic equilibrium in the plasma there is no free energy available, the entropy is maximal and waves in the plasma are not self-excited only excited by external effects. So instabilities are only in the plasma which is not in the stable equilibrium. In the unstable equilibrium all forces are in balance and a time-independent solution is possible but there is free energy available which can cause self-excited waves in the plasma.
The interchange instability is type of the Rayleigh-Taylor instability and grows at the expense of potential energy in the field of the centrifugal force due to curvature of the magnetic field. It significantly influences the evolution of a wide range of plasma systems. Let's assume the electrostatic situation $\mathrm{E} = -\nabla\phi$, purely toroidal magnetic field and isotropic pressure distribution and a random thermal fluctuation which caused a small sinusoidal pressure perturbation as is illustrated in Fig.(3.1). The over-tildes denotes the perturbations of the quantities.

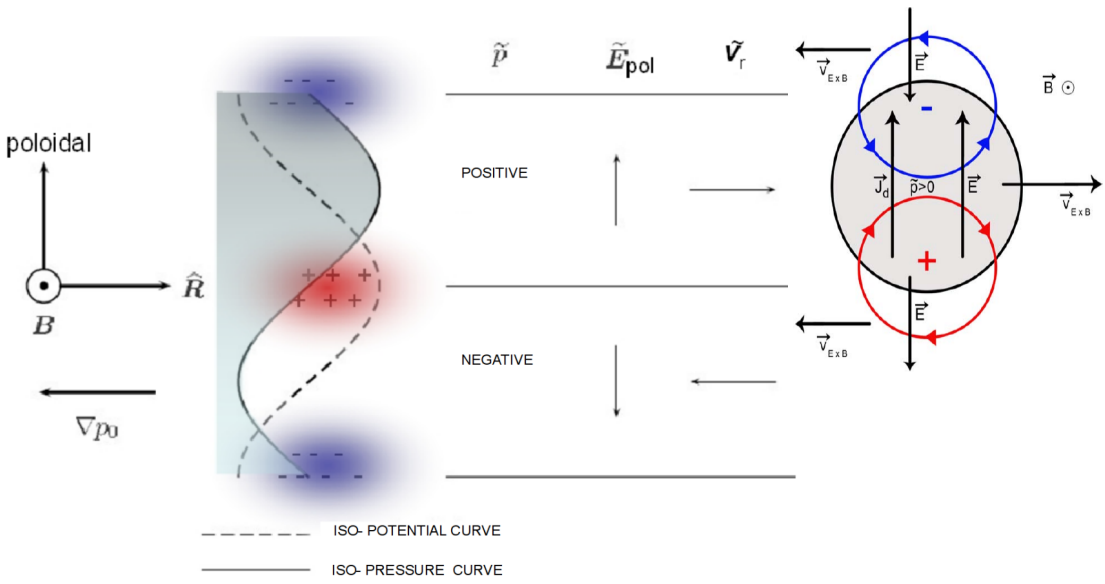

Figure 3.1: Illustration of the physical mechanism of the interchange instability. The ion gradient-B and curvature drift and also the diamagnetic drift are along the negative poloidal direction. The magnetic field strength decrease with major radius R. [42]. We can see on the right side of the picture the rotation of the turbulent structure due to Kelvin-Helmoltz instability. [63]

The gradient-B and curvature drift in the particle description or the diamagnetic drift in the fluid description are charge dependent and lead to a vertical/ poloidal charge polarization. It is readily shown that they lead to an electrostatic potential fluctuation which lags the pressure fluctuation by a phase $\pi/2$ [32]. It is also shown in Fig.(3.1). As a charge is built up on the sides of the ripple the electric field develops and changes sign as one goes from trough to crest in

the ripple. The resulting radial E × B drift is always directed outwards in those regions where the iso-pressure curve has moved outwards and inwards where the iso-pressure curve has moved inwards. The net result is a temporal growth of the initial pressure perturbation and it causes an instability. This instability causes a positive nonlinear radial transport which ruins the confined plasma equilibrium. However this situation corresponds only to the LFS of the tokamak where the magnetic field gradient ∇B and the equilibrium pressure gradient ∇p have same direction. On the HFS (high-field side) of the tokamak this gradients have opposite directions and the perturbations are stable.
The E × B drift tends to reduce the fluctuation amplitudes that is this has a stabilizing influence. For a weakly inhomogeneous pressure profile it can even completely stop the instability.

3.2 Blobs

The interchange instability results in generation of magnetic-field-aligned turbulent structures called **blobs** (Fig.(3.2)) in the vicinity of LCFS. Simultaneously there are also so called *holes*, that is low-density and low-temperature structures moving in opposite direction inwards into the region of central/confined plasma. The blobs have amplitudes significantly exceeding that of the ambient plasma and propagate radially outwards from the confined plasma. They results in a bursty transport events. Such an intermittent SOL transport due to the coherent plasma structures and corresponding instability mechanism seems to be a universal phenomenon independent of the details of magnetic field. It was found not only in the tokamaks [13] but also in stellarators [10], reversed field pinches [14] (RFX in Italy) and linear devices with no closed field lines and no curvature [12] (PISCES in USA).

For tokamak boundary plasmas they have a radial size a few centimeters and radial velocity around one-tenth of the ion sound speed ((units of km/s) close to the LCFS. Due to the particle losses along the open magnetic field lines their radial size, fluctuation amplitudes and radial velocity decay as they propagate through the SOL. For example in the T-10 tokamak in Moscow the blobs with $1.5 - 2.5$ times higher density than the background density was observed. Their radial velocity was reducing from 1km/s near the LCFS to 0.2km/s at the wall of the vacuum chamber. Their radial size was also decreasing with radius from 3cm to 0.5cm. The poloidal velocity directed towards an ion diamagnetic drif velocity was equal to $1.0 - 1.3$km/s and their poloidal size was $2 - 3$cm. The blobs was responsible for more than 50% of the total radial turbulent particle flux. In the vicinity of the LCFS the relative level of positive fluctuations was decreasing and the total turbulent flux of the particles was essentially lower than that in the far SOL. [47] (2004). Thus the intermittent transport due to the blobs defines the cross-field transport rather than cross-field diffusion.

The radial propagation is for blobs typical and make them different from for example a large scale vortex structures propagating in poloidal direction with the local E×B drift velocity and with the relatively long life time of $\approx 100\mu$s [15]. The edge localized modes (ELMs) seem to share the defining characteristics of the blobs. During the ELMs substructures in the SOL with sizes of $2 - 5$cm, lifetimes of the order of $20 - 50\mu$s, their poloidal and radial transport was observed in

the ASDEX and JET tokamaks [30]. According to [19] the blob as a filament of plasma should satisfies four theoretical properties:

- it has a single-peaked density distribution with a peak value much higher (typically $2-3$ times higher) than the surroundings root mean square fluctuations of the background plasma;

- its variation is much weaker and size much smaller in parallel direction than in the transverse direction;

- it has a dominant convective $\boldsymbol{E}\times\boldsymbol{B}$ velocity component in the direction of a charge-polarizing force (centrifugal force in tokamaks;

- it has a potential and *vorticity* ($\boldsymbol{\Omega}=\nabla\times \mathrm{v}_E$) with a dipole structure in the direction transverse to its propagation,

where $\mathrm{v}_E=(\boldsymbol{E}\times\boldsymbol{B})/B^2$ is the $\boldsymbol{E}\times\boldsymbol{B}$ drift velocity.
As the blobs move radially towards the wall a **Kelvin-Helmholtz instability** causes a rotation of upper and lower (in vertical direction) part of the blob - each in opposite direction as is illustrated in the right part of the Fig.(3.1).

The magnetic-field-aligned blobs have been explicitly observed by advanced imaging techniques [17] [16] in a wide range of confinement states as we can see in Fig.(3.3) and Fig.(3.4). In Fig.(3.4) we can see for the blobs typical tail left behind the mushroomlike front.

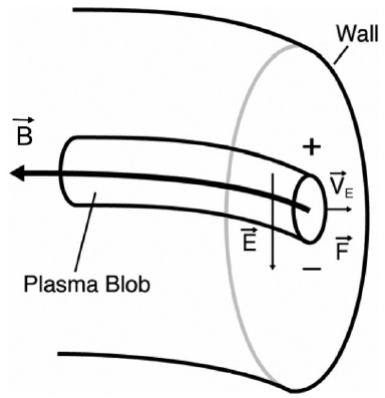

Figure 3.2: Sketch of a blob and charge polarization mechanism responsible for the radial transport. [19]

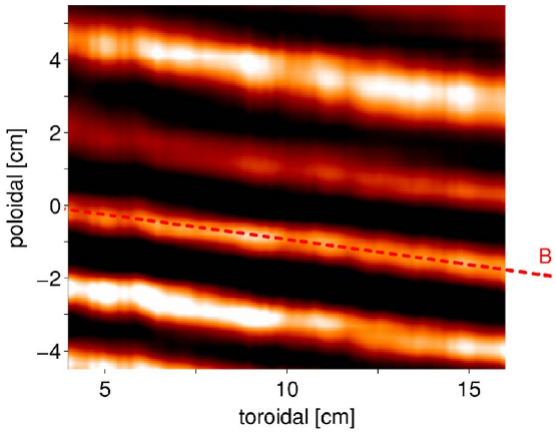

Figure 3.3: Camera snapshot (exposure time 6μms) of D_α intensity striations from an emission of a deuterium gas puff in a toroidal-poloidal cross- section at the outer midplane. A magnetic field line is superimposed at the radial position of maximum D_α emission intensity. (Color online). [17]

The nonlinear evolution and the radial propagation of the blobs were also demonstrated by numerical simulations. About this there are three next subheads.

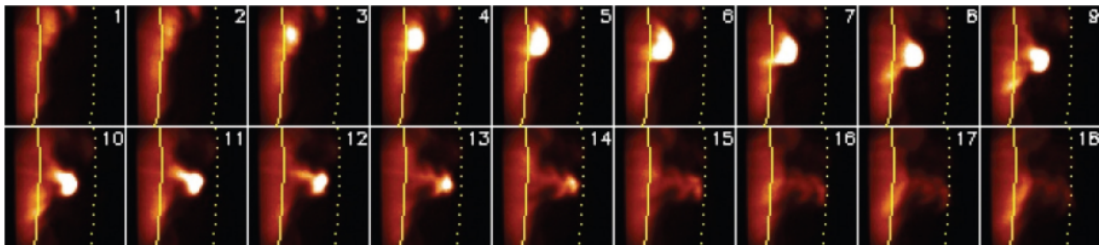

Figure 3.4: Formation and propagation of a blob observed during H-mode with the gas puff imaging diagnostic. Each box shows a 24×24cm *portion of the edge plasma just above the outer midplane in NSTX tokamak. The inter-frame is* 7.0μs*. The yelow solid line indicates the LCFS position as determined by LRDFIT equilibrium reconstruction. The dotted line represents the limiter shadow . [16]*

3.3 ESEL code

ESEL (ElectroStatic Edge-soL) is 2D (two-dimensional) drift-fluid turbulent computer code (written at present in programming language C). It has been developed in the RisøNational Laboratory in Denmark by O.E.Garcia, A.H.Nielsen, V. Naulin and J. Juul Rasmussen. ESEL is based on interchange and Bellan instability [63] (it is outside the scope of this thesis). It simulate plasma transport in the SOL at the outboard midplane of a toroidally magnetized plasma. In order to perform possible long-run simulations producing sufficient data for detailed statistical analysis it is reduced to 2D and ignores parallel drift wave dynamics and magnetic shear. It considers only electrostatic perturbations, that is perturbations of electric potential, relevant to the low pressure plasma in the SOL. The magnetic field is not evolving in time. Parallel transport along open magnetic field lines acts are included only as simple linear damping terms. It also assumes cold ions ($T_i = 0$) in some parameters and neglects electron inertia effects, finite Larmor radius and ion heat dynamics (more precisely the ion temperature equals in some equation terms nonzero but in some constants it equals zero). But it retain the fully nonlinear structure of the flow compression terms (derivatives), which is mandatory for the particle and energy conservation. This allows to describe the profile evolution and perturbations.

The 2D simulation domain features a region with particle and heat sources spatially localized in the edge region inside (and close to) the LCFS. The losses are mainly due to the radial motion along the open magnetic field lines in the SOL outside the LCFS and also due to collisional diffusion. Thus the time-averaged particle density and temperature radial profiles are peaked in the edge region inside the LCFS and relatively flat during the whole SOL. The resulting pressure gradient drives interchange mechanism in the edge region close to the LCFS, leading to the radial propagation of the blobs from the edge region close to the LCFS far into the SOL. In the process there are self-sustained sheared poloidal flows generated. These flows improve the confinement properties of the system but also lead to intermittent eruptions of hot plasma from the edge region close to the LCFS.

Equations of the ESEL code:

We have a fundamental Boltzmann equation

$$\frac{\partial f}{\partial t} + \boldsymbol{v} \cdot \nabla f + \frac{q}{m}(\boldsymbol{E} + \boldsymbol{v} \times B) \cdot \nabla_{\boldsymbol{v}} f = \left(\frac{\partial f}{\partial t}\right)_c, \tag{3.1}$$

where $f = f(\boldsymbol{r}, \boldsymbol{v}, t)$ is the velocity distribution function for particles with charge q and mass m, $\boldsymbol{E} + \boldsymbol{v} \times B$ is the electromagnetic force acting on the particles and $(\partial f/\partial t)_c$ is the time rate of change of f due to collisions. The symbol ∇ and $\nabla_{\boldsymbol{v}}$ stands for the gradient in (x, y, z) space and in velocity space that is:

$$\nabla = \left(\frac{\partial}{\partial x}; \frac{\partial}{\partial y}; \frac{\partial}{\partial z}\right),$$

$$\nabla_{\boldsymbol{v}} = \left(\frac{\partial}{\partial v_x}; \frac{\partial}{\partial v_y}; \frac{\partial}{\partial v_z}\right).$$

Now we can multiply the equation (3.1) by 1 and integrate over d$\boldsymbol{v}$ and obtain the fluid equation of continuity for particle density n:

$$\frac{\partial n}{\partial t} + \boldsymbol{v} \cdot \nabla(n\boldsymbol{u}) = \left(\frac{\partial n}{\partial t}\right)_c, \tag{3.2}$$

where $\boldsymbol{u}$ is the average or fluid velocity and $(\partial n/\partial t)_c$ is the time rate of change of n due to collisions.
Multiplying the equation (3.1) by $m\boldsymbol{v}$ and integrate over d$\boldsymbol{v}$ we can obtain the fluid equation of motion:

$$mn\left(\frac{\partial}{\partial t} + \boldsymbol{u} \cdot \nabla\right)\boldsymbol{u} = nq(\boldsymbol{E} + \boldsymbol{u} \times B) - \nabla \cdot \overleftrightarrow{\boldsymbol{P}} + \boldsymbol{R}, \tag{3.3}$$

where $\overleftrightarrow{\boldsymbol{P}} = p\overleftrightarrow{\mathbf{1}} + \overleftrightarrow{\boldsymbol{\Pi}}$ is the complete pressure tensor for a given particles which can be divided into diagonal part which represents scalar pressure p and non-diagonal stress tensor $\overleftrightarrow{\boldsymbol{\Pi}}$, $\overleftrightarrow{\mathbf{1}}$ is the unit tensor and $\boldsymbol{R}$ is the mean change in the momentum of the given particles due to collisions with all other particles.
And similarly, multiplying the equation (3.1) by $(1/2)mv^2$ and integrate over d$\boldsymbol{v}$ we can obtain the energy transport equation:

$$\frac{\partial}{\partial t}\left(\frac{nm}{2}u^2 + e\right) + \nabla \cdot \left(\frac{nm}{2}u^2\boldsymbol{u} + e\boldsymbol{u} + \overleftrightarrow{\boldsymbol{P}} \cdot \boldsymbol{u} + \boldsymbol{q}\right) = en\boldsymbol{E} \cdot \boldsymbol{u} + \boldsymbol{R} \cdot \boldsymbol{u} + Q, \tag{3.4}$$

where $nmu^2/2$ is the kinetic energy per unit volume, e internal energy per unit volume, $nmu^2/2\boldsymbol{u}$ macroscopic kinetic energy flux, $e\boldsymbol{u}$ the macroscopic internal energy flux, $\overleftrightarrow{\boldsymbol{P}} \cdot \boldsymbol{u}$ total pressure flux which represents work done by the total pressure forces , $\boldsymbol{q}$ microscopic energy flux or heat flux, $en\boldsymbol{E} \cdot \boldsymbol{u}$ Joule power per unit volume, $\boldsymbol{R} \cdot \boldsymbol{u}$ represents work done during collisions with all other particles and Q is the power per unit volume generated as a consequence of collisions with all other particles.
By using (3.2), (3.3), the equation of state $p = nT$ for scalar pressure p and equipartition theorem $(3/2)nT$ for internal energy e (temperature T is in eV) we can obtain from the (3.4) (I have verified it) the heat balance equation:

$$\frac{3}{2}n\left(\frac{\partial}{\partial t} + \boldsymbol{u} \cdot \nabla\right)T = nT\nabla \cdot \boldsymbol{u} + \overleftrightarrow{\boldsymbol{\Pi}}\nabla \cdot \boldsymbol{u} + \nabla \cdot \boldsymbol{q} = Q. \tag{3.5}$$

Let's denote the unit vector along the magnetic field $\boldsymbol{B}/B$ as $\boldsymbol{b}$. Neglecting the $\overleftrightarrow{\boldsymbol{\Pi}}$ and $\boldsymbol{R}$ in (3.3) and taking the vector product with $\boldsymbol{b}/(qnB)$ on both sides of equation (3.3) yields an expression for the fluid drift cross-field velocity:

$$\boldsymbol{u}_\perp = \boldsymbol{u}_E + \boldsymbol{u}_d + \boldsymbol{u}_p = \frac{1}{B}\boldsymbol{b}\times\nabla\phi + \frac{1}{qnB}\boldsymbol{b}\times\nabla p + \frac{m}{qB}\boldsymbol{b}\times\left(\frac{\partial}{\partial t} + \boldsymbol{u}\cdot\nabla\right)\boldsymbol{u}, \quad (3.6)$$

where $\boldsymbol{u}_E$ is the $\boldsymbol{E}\times\boldsymbol{B}$ drift or simply electric drift, $\boldsymbol{u}_d$ diamagnetic drift and $\boldsymbol{u}_p$ polarization drift. The polarization drift is a function of total cross-field velocity. It is treated iteratively and some its lowest order terms are neglected. In the governing equations of the ESEL code the Bohm normalization is used, that is the dimensionless quantities marked with line " ' " are used:

$$\begin{aligned} n' &= \frac{n}{n_0}, & T_e' &= \tfrac{T_e}{T_{e0}}, & \phi' &= \frac{e\phi}{T_{e0}}, \\ B' &= \frac{B}{B_0}, & t' &= t.\omega_{ci0}, & \boldsymbol{x}' &= \frac{\boldsymbol{x}}{\rho_{s0}}, \end{aligned} \quad (3.7)$$

where zero subscript indicates typical dimensional values of the quantities, usually chosen at the LCFS on the outboard midplane (in the ESEL simulations used in this thesis it indicates values at the LCFS only B_0 means value at the plasma centre - that is at the minor axis of the plasma) of the tokamak, and the ion gyro-frequency $\omega_{ci0} = eB_0/m_i$ and the hybrid thermal gyro-radius $\rho_{s0} = c_{s0}/\omega_{ci0}$ represents characteristic temporal and spatial scaling of the problem. $c_{s0} = \sqrt{T_{e0}/m_i}$ is the cold ion plasma sound speed.
In the code there are used a slab coordinates $(\boldsymbol{x}, \boldsymbol{y}, \boldsymbol{z})$ with $\boldsymbol{z}$ along the magnetic field. Using the Bohm normalization and substituting the cross-field drift velocity (3.6) into fluid equation of continuity for particle density (3.2) we can obtain the governing equation for low-frequency (i.e. drift ordered, or with frequency below the ion Larmor frequency) dynamics of plasma density n. Substituting the cross-field drift velocity (3.6) into heat balance equation (3.5) and using the Bohm normalization we can obtain the second governing equation for low-frequency dynamics of electron temperature T_e. The heat flux $\boldsymbol{q}$ is used in the dimensional form as the closed form of the collective cross-field heat flux $\boldsymbol{q}_\perp = (5nT_e\boldsymbol{b}\times\nabla T_e)/(2qB)$ [44] . And finally we can rewrite quasineutrality condition $\nabla\cdot(\boldsymbol{J}_p + \boldsymbol{J}_d - \boldsymbol{J}_{||}) = 0$ with using the vorticity definition $\Omega = |\nabla\times\boldsymbol{u}_E|$ and Bohm normalization as the third governing equation for low-frequency dynamics of plasma electric potential ϕ. The quasineutrality condition follows from the (3.2) multiplying by charge q and considering the total charge density equals zero and expresses the balance of density of parallel electric current $\boldsymbol{J}_{||}$, density of diamagnetic electric current $\boldsymbol{J}_d$ and density of polarization electric current $\boldsymbol{J}_{||}$. The equations are simplified using the drift approximation (i.e. averaging over ion Larmor orbits). So we have three reduced fluid equations for low-frequency dynamics of three quantities n, T_e, ϕ. Here they are [45]:

$$\frac{\mathrm{d}n'}{\mathrm{d}t'} + n'C'(\phi') - C'(n'T_e') = D'_{\perp n}\nabla'^2_\perp n' - \frac{n'}{\tau'_{||n}}, \quad (3.8)$$

$$\frac{\mathrm{d}T'_e}{\mathrm{d}t'} + \frac{2}{3}T'_e C'(\phi') - \frac{7}{3}T'_e C'(T'_e) - \frac{2}{3}\frac{T'^2_e}{n'}C'(n') = D'_{\perp T_e}\nabla'^2_\perp T'_e - \frac{T'_e}{\tau'_{||T_e}}, \tag{3.9}$$

$$\frac{\mathrm{d}\Omega'}{\mathrm{d}t'} - C'(n'T'_e) = D'_{\perp\Omega}\nabla'^2_\perp\Omega' - \frac{\Omega'}{\tau'_{||\Omega}}, \tag{3.10}$$

where the operators marked with line " ' " are operators in slab dimensionless coordinates $(\boldsymbol{x}', \boldsymbol{y}', \boldsymbol{z}')$. The vorticity Ω', the advective derivative $\mathrm{d}/\mathrm{d}t'$ and the curvature operator C' due to the non-uniform magnetic field B' are, respectively, defined by

$$\Omega' = \nabla'^2_\perp\phi',$$

$$\frac{\mathrm{d}}{\mathrm{d}t} = \frac{\partial}{\partial t'} + \boldsymbol{u}'_e\cdot\nabla' = \frac{\partial}{\partial t'} + \frac{1}{B'}\boldsymbol{z}\times\nabla'\phi'\cdot\nabla',$$

$$\frac{1}{B'} = 1 + \frac{r_0 + \rho_{s0}x'}{R_0},$$

$$C' = -\frac{\rho_{s0}}{R_0}\frac{\partial}{\partial y'}.$$

R_0 is major radius and r_0 is minor radius. For dimensional operators and quantities it stands $\Omega = \nabla^2_\perp\phi/B$, $B(r) = B_0/(1 + r\cos\theta/R_0)$ (r and θ are polar coordinates in the minor cross-section), $\mathrm{d}/\mathrm{d}t = \partial/\partial t + \boldsymbol{u}_e\cdot\nabla$, $C = \nabla(1/B)\cdot\boldsymbol{b}\times\nabla + (1/B)\nabla\times\boldsymbol{b}\cdot\nabla$.
The terms on the right-hand side of three governing equations (3.8),(3.9),(3.10) represents dissipation as a result of perpendicular collisional diffusion $D'_{\perp a}\nabla'^2_\perp a'$ and parallel losses to the divertor targets $a'/\tau'_{||a}$ (with a'= n', T'_e, Ω', and a= n, T_e, Ω) [45]:

$$D'_{\perp n} = \frac{D_{\perp n}}{\rho^2_{s0}\omega_{ci0}}, \qquad D'_{\perp T_e} = \frac{D_{\perp T_e}}{\rho^2_{s0}\omega_{ci0}}, \qquad D'_{\perp\Omega} = \frac{D_{\perp\Omega}}{\rho^2_{s0}\omega_{ci0}},$$

$$\tau'_{||n} = \tau_{||n}.\omega_{ci0}, \qquad \tau'_{||T_e} = \tau_{||T_e}.\omega_{ci0}, \qquad \tau'_{||\Omega} = \tau_{||\Omega}.\omega_{ci0}.$$

$D_{\perp n}$, $D_{\perp T_e}$, $D_{\perp\Omega}$ are neoclassical Pfirsch-Schl**ü**ter perpendicular collisional diffusion coefficients for particles, electron heat and momentum respectively. $\tau_{||n}$, $\tau_{||T_e}$, $\tau_{||\Omega}$ are the corresponding parallel loss times. The relations for their computation are shown in [45].
The density n and electron temperature T_e are in the SOL damped to a constant background level which is by definition unity in the nondimensional ESEL model. On the other hand, the vorticity is damped to zero because there is no vorticity source.
The terms in the equations (3.8),(3.9),(3.10) have in the dimensional form this meaning:
$C(\phi) = \nabla\cdot\boldsymbol{u}_E$, $C(p) = C(nT_e) = \nabla\cdot\boldsymbol{J}_d$, $\boldsymbol{\Omega}\approx\boldsymbol{b}\cdot\nabla^2_\perp\phi$, $\mathrm{d}\Omega/\mathrm{d}t = -(B\nabla\cdot\boldsymbol{J}_p)/nm$, $C(T_e) = (2q\nabla\cdot\boldsymbol{q}_\perp)/(5nT_e) + (\boldsymbol{b}\cdot\nabla n\times\nabla T_e)/(nB)$.

The parallel terms are apparently the weakest point of the ESEL and recently there has been a lot of effort to develop some more sophisticated model of parallel transport. Recently, about 2012, J. Seidl in Prague in Czech Republic added

one extra (sheath dissipation) term on the right-hand side of the equation (3.10). With this change the governing equation of the ESEL code for low-frequency dynamics of plasma electric potential ϕ looks like this:

$$\frac{\mathrm{d}\Omega'}{\mathrm{d}t'} - C'(n'T'_e) = D'_{\perp\Omega}\nabla'^2_{\perp}\Omega' - \frac{\Omega'}{\tau'_{||\Omega}} + \frac{1}{\tau'_{||n}}\frac{L_{||d}}{M_{||}2L_{||m}}\left[1 - \exp\left(\alpha - \frac{\phi'}{T'_e}\right)\right], \quad (3.11)$$

where α is the coefficient for the floating potential from the equation 1.57 for $\delta = 1$ which is ≈ 2.8 for $T_e = T_i$, $M_{||} = v_{||}/c_s$ is the parallel Mach number as the ratio of the parallel flow velocity $v_{||}$ and the warm ($T_i \neq 0$) ion sound speed c_s. In most simulations presented in this thesis is the ratio $T_i/T_e = T_{i0}/T_{e0}$. Sometimes $T_i = T_{i0}$. $L_{||d}$ is the parallel connection length for SOL between midplane and divertor and $L_{||m}$ is the parallel connection length for SOL between one divertor and second divertor. This last term on the right-hand side of (3.11) has in the dimensional form meaning of the average over the parallel direction with a connection length $L_{||m}$ of the divergence of the parallel electric current $\langle\nabla\cdot\boldsymbol{J_{||}}\rangle \approx \langle\boldsymbol{b}\cdot\nabla J_{||}\rangle = \langle\nabla(enc_s[1-\exp(-eV_{fd}/T_{ed})])\rangle \approx (enc_s/L_{||m})[1-\exp(-e\phi_d/T_{ed})]$, where c_s is the warm ($T_i \neq 0$) ion sound speed, $T_{ed} \approx T_e$ is the electron temperature in vicinity of the divertor and $-V_{fd} \approx \phi - \alpha(T_e/e)$ is the floating potential on the divertor (compare it with (2.5)).

The computational domain is illustrated in Fig.(3.5). It forms a 2D box whose sides have an extent $x'_{\max}$ in radial $\boldsymbol{x}'$ direction and $y'_{\max}$ in poloidal $\boldsymbol{y}'$ direction. It is about hundred of ρ_{s0}. This box simulate SOL plasma in the neighbourhood of the outer midplane. For the poloidal direction periodic boundary conditions are invoked that is $a'(x',0,t') = a'(x',y'_{\max},t')$, $\forall x \in (0;x'_{\max})$ (with a'= n', T'_e, ϕ', Ω'). In order to control the collective and collisional fluxes of particles and heat through the radial boundaries there are also radial boundary conditions for $\partial a'/\partial x'$ (Neumann boundary conditions) and for a' (Dirichlet boundary conditions) that is the values $\partial a'(0)/\partial x'$, $\partial a'(x'_{\max})/\partial x'$, $a'(0)$, $a'(x'_{\max})$ which are generally different for different simulations. For the vorticity $\boldsymbol{\Omega'}$ there are a stress-free boundary conditions used in most of simulations used in this thesis (their meaning is outside the scope of this thesis).

The computational domain consists from the edge area ($x \in (0;x'_{\mathrm{edge}})$) representing the central plasma, the SOL area ($x \in (x'_{\mathrm{edge}};x'_{\mathrm{SOL}})$) representing the SOL plasma and the wall shadow area ($x \in (x'_{\mathrm{SOL}};x'_{\max})$ representing the plasma outside a midplane wall major radius (Fig.(3.5)). The definition of the computational domain is $nx \times ny$ (in most simulations used in this thesis it is 948×512). Each 5000th time step $\mathrm{d}t'$ are data storaged in all this $nx \times ny$ points and we can create figure as Fig.(3.5). Each 10th time step are data poloidally averaged in radial locations representing a model probes (the black dots in Fig.(3.5)) and put into the ESEL output.

The demonstration video of the ESEL simulation matching the TCV tokamak plasma is on CD enclosed with this diploma thesis (provided by courtesy of J. Seidl).

For the ESEL the single-point probability distribution function (PDF) with increasingly non-Gaussian form and developing exponential tails at movement

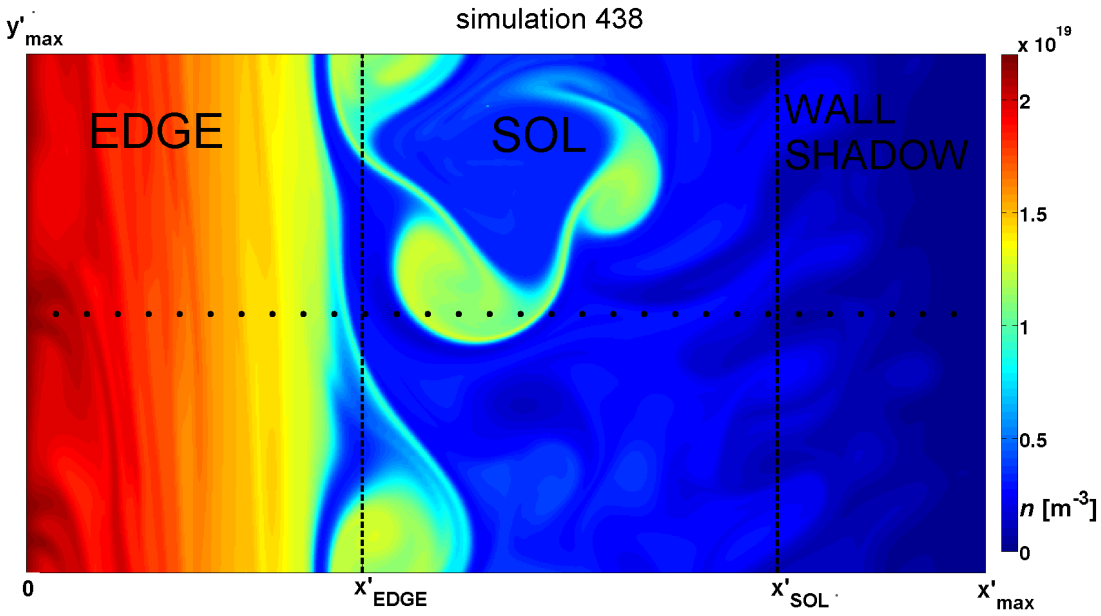

Figure 3.5: The 2D computational domain of the ESEL simulation with job number 438 (it will be used in chapter 4). The black dots represents the locations of the model probes which I used. We can also clearly see the blobs simulated by the ESEL.

from the LCFS further to the SOL [48] [44] and asymmetric conditional wave forms with a steep front and trailing wake are typical [44]. The conditional averaged wave forms or shortly CAV are averages of many time signals corresponding with the blob crossings through a certain location. It will be verified in the next chapter 4.

3.4 Time development of comparisons between ESEL and experiment

In this thesis the experimental data measured by the fast reciprocating probes in the tokamaks ASDEX Upgrade and COMPASS and the output data of the code ESEL are compared. In the past the similar comparisons was made. From the comparisons for tokamak JET there was conclusion that the SOL radial transport in JET ohmic plasma is dominated by electrostatic interchange turbulence characterized by radially propagating blobs [39] (2006). Another comparisons was made for tokamak TCV [42] in 2006, for tokamak TEXTOR [40] in 2011 or for tokamak MAST [41] in 2012. Also a comparisons for tokamak ASDEX Upgrade was made, the last by P. Vondracek in his diploma thesis [43] in 2011 and 2012. In the meantime the ESEL from Danish group (in the RisøNational Laboratory in Denmark) was used. Except the Danish group the ESEL is developed also by J. Seidl in Prague. From him the newest attempts for improvement of the ESEL was made and they are analysed in this thesis.

. Initially the ESEL was used by Danish group for comparisons between it and the tokamak TCV in Switzerland for the plasma with high collisionality

and it was very successful. The fluctuations of density in the ESEL was in good agreement with experiment data from Langmuir probes (Fig.3.6 and Fig.3.7) - year 2006.

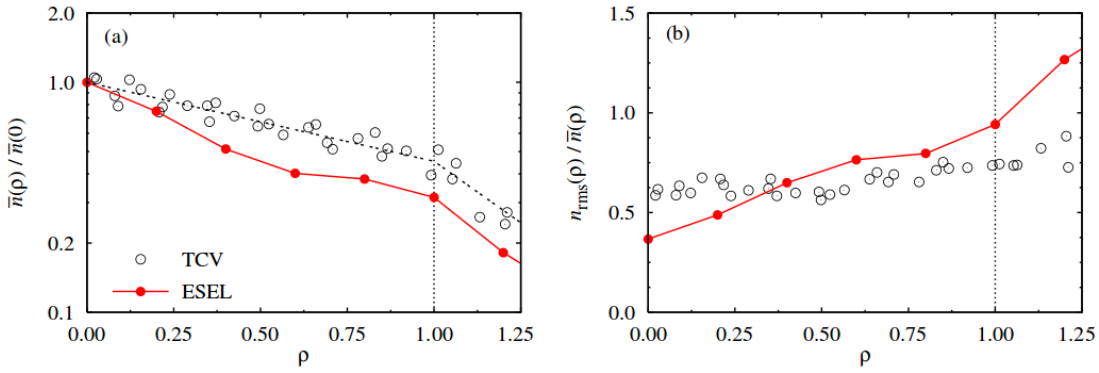

Figure 3.6: Radial variation of average (a) particle density normalized to the separatrix value and (b) relative density fluctuations from probe reciprocations at high particle density in TCV, compared with results from the ESEL matching the SOL conditions during this probe reciprocations. The broken line in (a) shows exponential fit to the experimental data points. [46]

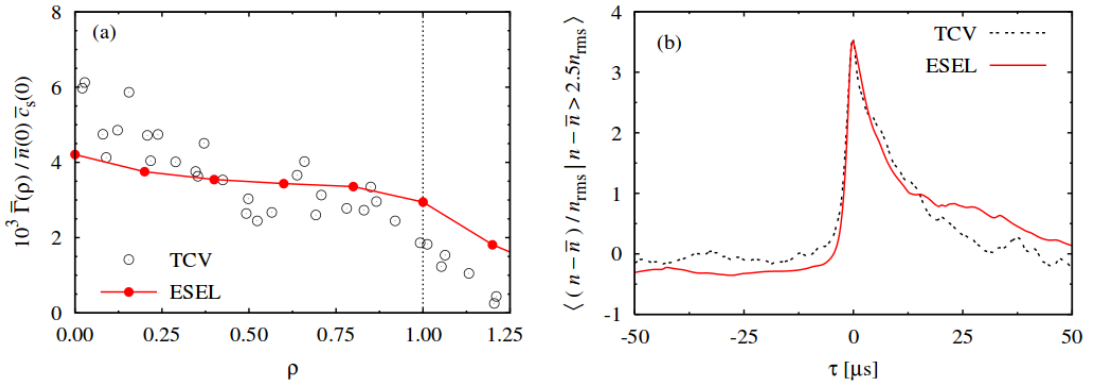

Figure 3.7: Radial variation of (a) average particle flux normalized to its acoustic value at the separatrix position and (b) the conditionally averaged wave forms at the wall radius from probe reciprocations at high particle density in TCV, compared with results from the ESEL matching the SOL conditions during this probe reciprocations. The conditionally average is taken over all particle density bursts exceeding 2.5 times the standard deviation. [46]

Also other quantitative good agreements of ESEL output with experimental data from Langmuir probes in tokamak TCV was observed concerning mainly density fluctuations and particle cross-field transport [49–51].

. Then the Danish group made comparisons between ESEL and the tokamak ASDEX Upgrade in Germany. The tokamak ASDEX Upgrade is more ITER relevant than TCV and his plasma has higher temperature and therefore lower collisionality than TCV. In this tokamak also temperature and potential was measured with high spatial ($2-4$mm) and temporal (1μs)

resolution using except Langmuir probes also ball-pen probes. Then it was compared to ESEL simulation and there was big discrepancies. The radial profile of averaged density in the ESEL was too flat contrary to the experimental profile. The radial profile of averaged electric potential from the ESEL was also very different from the experimental profile. The averaged relative temperature and electric potential fluctuations in the ESEL was too large as we can see in one ESEL simulation with the job number 137 in Fig.3.8 - year 2011.

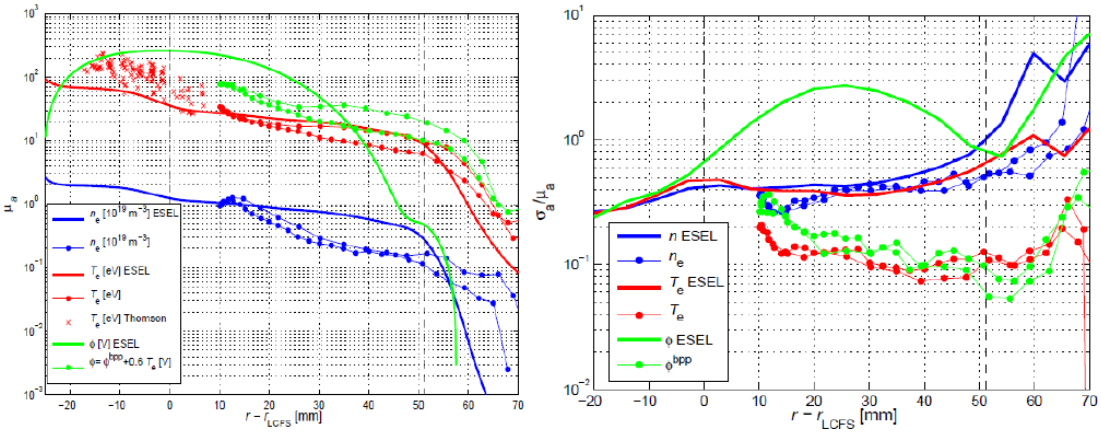

Figure 3.8: Radial variation of average (left) particle density, temperature and electric potential and (right) relative density, temperature and electric potential fluctuations from probe reciprocations in ASDEX Upgrade (dotted lines), compared with results from the ESEL simulation with number 137 (solid lines) matching the SOL conditions during this probe reciprocations.

. It was necessary to develop the ESEL further. Those days around year 2011 J. Seidl suggested the last term on the right-hand side of the equation (3.11). The new simulations around year 2012 with this extra term was created by the Danish group. For example we can see the results from a simulation with job number 002 in Fig.3.9.The radial profil of average electric potential was finally in agreement with the ASDEX data and also the radial profil of average particle density was more consistent with the ASDEX data. But the average relative density, temperature and electric potential fluctuations was even larger than those in previous simulations.

. Then in 2012 I began to compare the ESEL and ASDEX Upgrade data. I began to investigate a possibilities of interpretations of the experimental data with the help of the interchange turbulence paradigm in ESEL. As will be discussed in the next chapter, after a small change in approximation of the last extra term on the right side of equation 3.11, a simulations with job number 051 and 050 was created. The last sheath dissipation term in (3.11) had still linear form.

. In 2013 J. Seidl in Czech Republic undertook the improvement of the ESEL. He created ESEL simulations matching the ASDEX Upgrade plasma with job numbers 338, 438, 448, 462, 505, 546, 557, 655, 656, 665, 675, 771 and 772 (and many others). The last sheath dissipation term in (3.11) had

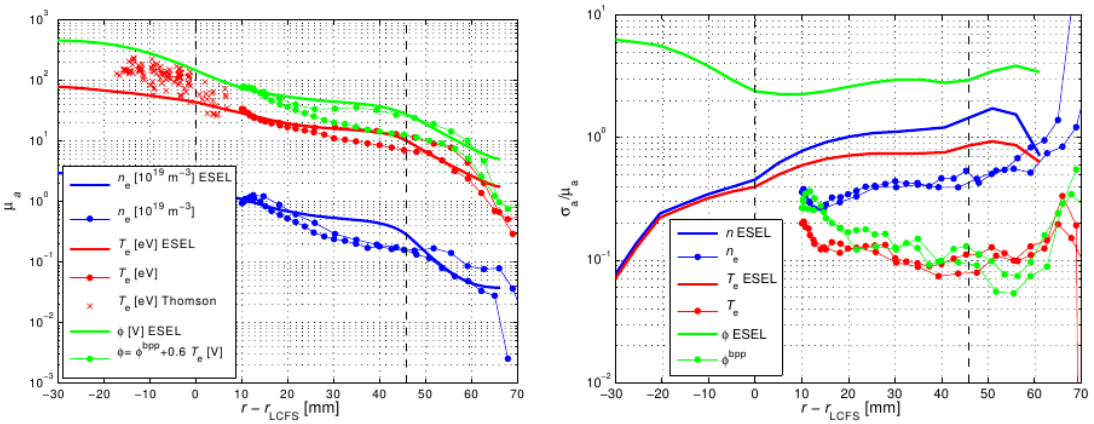

Figure 3.9: Radial variation of average (a) particle density, temperature and electric potential and (b) relative density, temperature and electric potential fluctuations from probe reciprocations in ASDEX Upgrade (dotted lines), compared with results from the ESEL simulation with number 002 (solid lines) matching the SOL conditions during this probe reciprocations. [43]

exponential form. Finally he created ESEL simulation matching the COMPASS plasma with job number 6092_2.58 (and many others). The number 6092 is the number of the corresponding charge in the tokamak COMPAS which was used for comparison. The results are presented in the next two chapters.

3.5 Other codes

During 2008 an 2D extend version of the ESEL model with name BESEL has been developed [20]. It his version the electron pressure instead of electron temperature is used as dependent variable, to ensure energy conservation (in the ESEL the energy is not well conserved). Another 2D extend version of the ESEL is GESEL which use a gyrofluid approach (finite Larmor radius) instead of fluid approach.
There is also 3D extension of the ESEL with name DiESEL [20]. DiESEL solves interchange model in 3D toroidal geometry with tokamak like magnetic field. Toroidal direction is divided into a number of drift planes. On each drift plane the equations are solved on a disk domain and communicate parallel with the nearest drift planes the ion sound speed c_s for the density equation and the Alfvén speed v_A for the vorticity equation. The DiESEL treats mainly the simple parallel dynamics and boundary conditions used in the ESEL. There is also possibility to join ESEL with 1D model SOLF1D [21] from which the information about ion temperature and parallel dynamics can be obtained.

In the next Table(3.1) the comparisons between some SOL turbulence codes and experimental data relevant to blobs are summarized. (Aditya is medium size tokamak in India. DIII-D, NSTX and C-Mod are tokamaks in USA.)

Generally **two-dimensional (2D) simulations** often rely on the thin layer approximation and assumed a local turbulence drive within the SOL. But they can

2D codes Experiment	ESEL ASDEX-Upgrade	ESEL JET	ESEL TCV	FDET Aditya	SOLT NSTX	— Helimak
Fluctuation levels		√	√	√	√	
Turbulent spectra						√
Correlation times or lengths	√		√			√
PDFs, Skewness			√	√	√	√
2D imaging		√	√		√	
Radial profiles	√	√	√		√	√
Blob properties	√		√		√	
References	[34], [43]	[45], [39]	[42], [49], [46]	[22]	[23], [24]	[25]
3D codes Experiment	BOUT DIII-D	BOUT C-Mod	BOUT NSTX	BOUT MAST	NLET C-Mod	GEMR C-Mod
Fluctuation levels		√		√	√	√
Turbulent spectra			√		√	√
Correlation times or lengths		√	√		√	√
PDFs, Skewness				√		
2D imaging	√				√	
Radial profiles		√				
Blob properties	√	√		√	√	
Parallel mode structure		√	√			
References	[26]	[26], [35], [37]	[26]	[36]	[29], [28]	[27]

Table 3.1: Comparisons of SOL simulations and experimental data. A sign "√" means that indicated comparison was attempted (not necessarily with good agreement). Comparisons were both qualitative and quantitative. [19] (modified)

be run over a wide range to identify physical trends and obtain optimal comparisons with data. **Three-dimensional (3D) simulations** usually assume frozen profiles, are time-consuming and are not easy controllable for long integration times in order to make advanced statistical analysis.

4. Comparison: ASDEX vs ESEL

4.1 ASDEX Upgrade data and their processing

The experimental data from the ASDEX Upgrade used in this thesis were measured in 2009. They were used in [34] and [43] but here in this thesis they are processed again using some more general assumption (for example ion temperature is different from electron temperature as will be discussed later). When measuring there was obtained a high enough spatial ($2-4$ mm) and temporal ($1\ \mu$s) resolution of temperature to observe details of individual turbulence structures (blobs). The plasma potential ϕ_p was measured almost directly by using ball-pen probes. The measurements were made in the SOL on the low field side (LFS) around the outboard midplane of the tokamak vessel (median plane with cylindrical coordinate $z = 0$) where the plasma pressure gradient is larger than toroidal magnetic field gradient and the plasma is very unstable. In this part of the tokamak plasma the ESEL simulates the plasma transport thus we can compare it. The experiment was performed using the reciprocating horizontal manipulator located just above ($z = 0.3125m$) the LFS midplane in the SOL of ASDEX Upgrade. The probe head with a 6cm diameter mounted on the end of the manipulator contained 4 Langmuir probes and 4 ball-pen probes. They are labeled as LP1, LP2, LP3, LP4, BPP1, BPP2, BPP3, BPP4. It is illustrated in Fig.4.1.

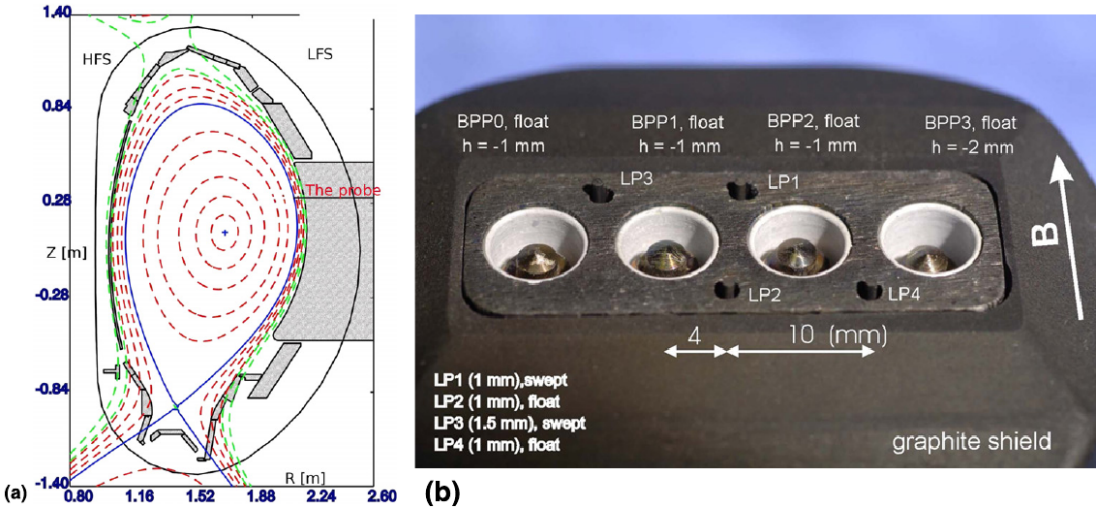

Figure 4.1: (a) Plasma geometry of the ASDEX Upgrade tokamak. The reciprocating probe reaches the LCFS above the LFS midplane $z = 0.3125m$. (b) A photograph of the reciprocating probe head with 4 Langmuir pins (LPs) and 4 ball-pen probes (BPPs). The vertical axis of the image corresponds to the parallel direction in the tokamak and the horizontal axis of the image corresponds to the poloidal direction in the tokamak. [34]

The ball-pen probes consisted of stainless steel collectors and of boron nitride shielding tubes. The diameter of collectors was 4mm and the interior diameter of shielding tubes was 6mm. The Langmuir probes was made of graphite

pins with 0.9mm diameter. In poloidal direction none of the probes shielded another. The BPPs and LPs are located in different radial position. It is good due to inclination of the magnetic flux surface with respect to the probe head surface $\approx 12°$. All probes except for LP1 and LP3 were connected as floating. LP3 was swept (connected on changeable voltage) to measure the I-V characteristic and LP1 was set to measure the ion saturation current I_{sat}^{+}. The time resolution of the measurements was limited only by the sampling frequency of the data acquisition system which was 2MHz. The analysed data come from the discharge #24349, with a reproducibility verified in data from the discharge #24348. The measurements were performed during the radial motion of the manipulator under this conditions :deuterium plasma, L-mode with the neutral beam injection (NBI) power of $\approx$ 1MW, the plasma current $\approx$ 800kA, the line averaged density $\approx 3 \cdot 10^{19}\mathrm{m}^{-3}$, and the toroidal magnetic field $\approx$ 2.5T in the plasma centre and $\approx$ 1.9T in the SOL.

The data from the probes LP1, LP2, BPP1, BPP2 were used. The next values of the potentials and temperature are in V and eV respectively.
BPP1 was floating and it measured

$$V_f^{\mathrm{BPP1}} \approx \phi_p^{\mathrm{BPP1}} - 0.6\frac{T_e^{\mathrm{BPP1}}}{e}. \tag{4.1}$$

BPP2 was floating and it measured

$$V_f^{\mathrm{BPP2}} \approx \phi_p^{\mathrm{BPP2}} - 0.6\frac{T_e^{\mathrm{BPP2}}}{e}. \tag{4.2}$$

LP1 was biased sufficiently negatively (with less than $-100V$) to measure the I_{is}.
LP2 was floating and it measured

$$V_f^{\mathrm{LP2}} \approx \phi_p^{\mathrm{LP2}} - \alpha\frac{T_e^{\mathrm{LP2}}}{e},. \tag{4.3}$$

V_f^{BPP1}, V_f^{BPP2}, V_f^{LP2} is the floating potential of the probe BPP1, BPP2 and LP2 respectively, ϕ_p^{BPP1}, ϕ_p^{BPP2}, ϕ_p^{LP2} is the plasma potential in vicinity of the BPP1, BPP2 and LP2 respectively and T_e^{BPP1}, T_e^{BPP2}, T_e^{LP2} is the electron temperature in the vicinity of the BPP1, BPP2 and LP2 respectively. The coefficient α (in the equation (1.57)) equals $\approx$ 2.8 for $T_i/T_e = 1$. But the ratio of the ion and electron temperature T_i/T_e decays in the SOL exponentially from $\approx$ 10 to $\approx$ 5 as it follows from results in [55] or [62]. Subsequently the α can be equal only $\approx$ 2 - for $T_i/T_e \approx 10$. It was used the main value of the temperature ratio as $T_i/T_e = 2$, because for such value was ESEL simulations running, and range of the ratio from $T_i/T_e = 1$ to $T_i/T_e = 10$ was used for calculation of an uncertainty of the coefficient α.
The plasma potential ϕ_p (in V), the electron temperature T_e (in eV) and the electron density n_e (in m^{-3}) were calculated as following:

$$T_e^{\mathrm{BPP1-LP2}} = \frac{(V_f^{\mathrm{BPP1}} - V_f^{\mathrm{LP2}})}{\alpha - 0.6}, \tag{4.4}$$

since $(\phi_p^{\mathrm{BPP1}} - \phi_p^{\mathrm{LP2}}) \approx 0$ and $T_e^{\mathrm{LP2}} \approx T_e^{\mathrm{BPP1}} \approx T_e^{\mathrm{BPP1-LP2}}$, see Fig.4.1 (b). $T_e^{\mathrm{BPP1-LP2}}$ is the electron temperature in the area between the probes BPP1 and LP2.

$$T_e^{\mathrm{BPP2-LP2}} = \frac{(V_f^{\mathrm{BPP2}} - V_f^{\mathrm{LP2}})}{\alpha - 0.6}, \tag{4.5}$$

since $(\phi_p^{\mathrm{BPP2}} - \phi_p^{\mathrm{LP2}}) \approx 0$ and $T_e^{\mathrm{LP2}} \approx T_e^{\mathrm{BPP2}} \approx T_e^{\mathrm{BPP2-LP2}}$, see Fig.4.1 (b). $T_e^{\mathrm{BPP2-LP2}}$ is the electron temperature in the area between the probes BPP2 and LP2.

$$T_e = \frac{T_e^{\mathrm{BPP1-LP2}} + T_e^{\mathrm{BPP2-LP2}}}{2}, \tag{4.6}$$

$$n_e = n_e^{\mathrm{LP1}} = n_0\sqrt{2}\frac{I_{is}}{\sqrt{T_e + T_i}} \approx \frac{13 \cdot 10^{18} m^{-3}\sqrt{2}}{0.014}\frac{I_{is}}{\sqrt{T_e + T_i}}, \tag{4.7}$$

where $13 \cdot 10^{18}\mathrm{m}^{-3}$ is the calibration factor (in units $\mathrm{m}^{-3}(eV)^{1/2}$) for electron density acquired by lithium beam diagnostic measurement at the deepest location reached by the probe head. The electron temperature value at this point assumed equal to ion temperature at LCFS needed for its calculation was calculated from probes signals. At this location the I_{is} was $I_{is} \approx 0.014$A. As it was found out later the deepest location of the probe head was immediate vicinity of the LCFS .

$$\phi_p = \frac{V_f^{\mathrm{BPP1}} + V_f^{\mathrm{BPP2}}}{2} \tag{4.8}$$

It would be better define ϕ_p as

$$\left(\phi_p = \frac{V_f^{\mathrm{BPP1}} + V_f^{\mathrm{BPP2}}}{2} + 0.6\frac{T_e^{\mathrm{BPP1}} + T_e^{\mathrm{BPP2}}}{2e}\right),$$

It was used the main value of the temperature ratio as $T_i/T_e = 2$, because for such value was ESEL simulations running, and range of the ratio from $T_i/T_e = 1$ to $T_i/T_e = 10$ was used for calculation of an uncertainty of the coefficient α. but T_e^{BPP1} and T_e^{BPP2} were not known. The consequences of this simplification are specifically commented in the [34]. Small frequencies originating from the background were identified and removed from the signal.

During the discharge #24349 the motion of the probe head lasted for 174.8ms (it is about the time the used data was measured). This time corresponds to the movement from the radial position 73.1066mm from the LCFS to the radial position −0.3308mm from the LCFS (0.3308mm behind LCFS) and back to the radial position 74.1788mm from the LCFS. During the discharge #24348 the total time of the movement was 168.2ms, the starting position 78.6515mm, the deepest position 6.3118mm and the ending position 80.3593mm. This motion and the data from the probes LP1, LP2, BPP1, BPP2 for discharge #24349 are shown in Fig.(4.2). For the discharge #24348 it is similar. The data from the probes LP1, LP2, BPP1, BPP2 and also the locations of the probe head with respect to the LCFS and appropriate record times were divided into 60 sets each corresponding to a time interval 2.9ms for the discharge #24349 and 2.8ms for the discharge #24348. This time intervals are short enough to treat probes as steady because they corresponds to the radial probe motion less than 2.9mm/ 2.8mm (second

is for the discharge #24348) which is much shorter than the typical scrape off thickness (1.9). This sets contains 5826/5610 values that is sufficient for basic statistic. It was verified ([34]) that the choice of this time intervals influences only the values in the wall shadow beyond 50mm from LCFS, where the ratio signal/noise is too small. For each of these 60 sets the average location of the probe head and the average record time were calculated (red crosses in the Fig.(4.2)). Also a statistical moments (mainly arithmetic mean and relative deviation) of each measured quantity for each of these 60 sets were calculated. These 60 values at appropriate 60 positions represent as 60 time average values measured by a fictiv It was used the main value of the temperature ratio as $T_i/T_e = 2$, because for such value was ESEL simulations running, and range of the ratio from $T_i/T_e = 1$ to $T_i/T_e = 10$ was used for calculation of an uncertainty of the coefficient α.e steady probes deployed in the SOL. The temporal average position of the LCFS was first determined from the EFIT (Equilibrium fitting code). Then I shifted it (because the EFIT is generally not very reliable) about 1cm deeper according to a comparison between experimental and model (ESEL) radial profile of plasma potential.

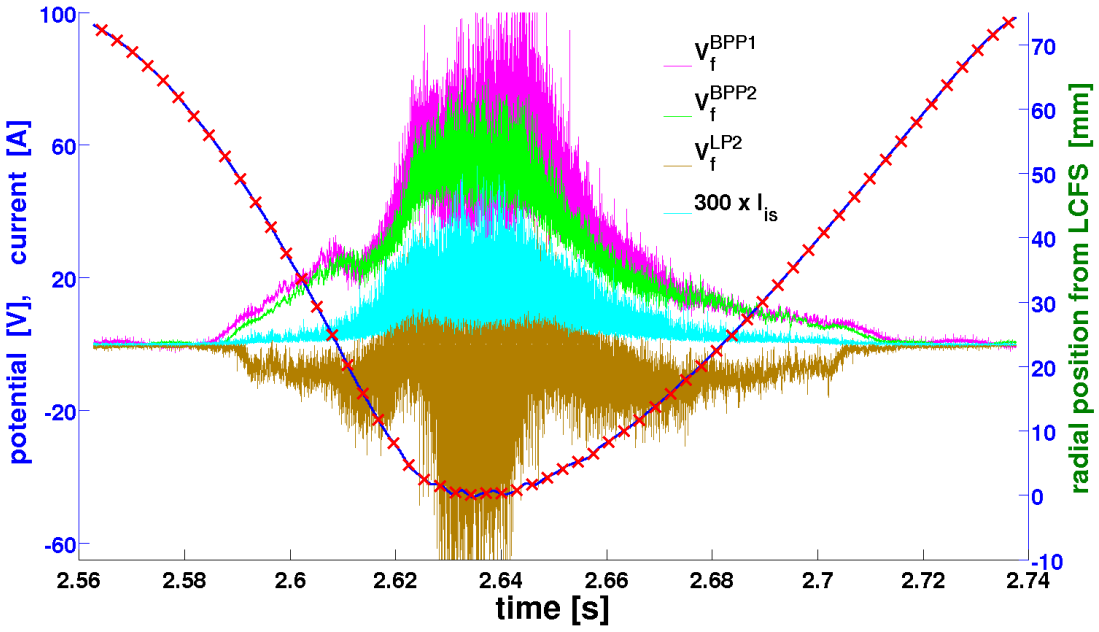

Figure 4.2: Temporal evolution of the data from the probes LP1, LP2, BPP1, BPP2 (left vertical axis) and the probe head motion with respect to the LCFS (right vertical axis) during the probe head reciprocation in discharge #24349 in ASDEX Upgrade. The red crosses mark the average probe head location and record time of the 60 used data sets.

From these 60 time sets of data the radial profiles of mean $[\langle a\rangle](r)$, radial profiles of relative fluctuations $[\sigma a/\langle a\rangle](r)$, relative profiles of mean divided by negative radial derivative of mean $\lambda(r) = -[\langle a\rangle/(\mathrm{d}\langle a\rangle)/\mathrm{d}r](r)$, conditionally averaged waveforms (CAVs) and probability density functions (PDFs) were calculated. Where $a = n$, T_e or ϕ and $\langle\ \rangle$ means time average over 5826/5610 values for each of 60 radial positions. It was calculated for three quantities : plasma density, electron temperature and plasma potential. The program Matlab was used.

The functions $[\langle a\rangle](r)$, $[\sigma a/\langle a\rangle](r)$ and $\lambda(r) = -[\langle a\rangle/(\mathrm{d}\langle a\rangle)/\mathrm{d}r](r)$ were computed directly from 60 arithmetic means and relative deviations for each radial position. The derivative in computing of $\lambda(r)$ was computed numerically in each of 59 radial position only from a two It was used the main value of the temperature ratio as $T_i/T_e = 2$, because for such value was ESEL simulations running, and range of the ratio from $T_i/T_e = 1$ to $T_i/T_e = 10$ was used for calculation of an uncertainty of the coefficient α. neighbouring values.
PDFs in this thesis describes the relative likelihood for random variable $[a(t) - \langle a(t)\rangle]/\sigma a(t)$ to take on a given value. The time t is the time of the one from 60 probe head motion sections (it was calculated for any of the 60 radial positions).

CAVs
The conditionally averaged waveforms describe a typical behaviour of $a = n$, T_e or ϕ as the blob passes across the probe head. They are average of these little pieces of the function $a(t)$ when a blob is very probably on the probe head. The time t is again as in the case of the PDFs the time of the one from 60 probe head motion sections (it was again calculated for any one of the 60 radial positions). That 'very probably' is however difficult to determine. In this thesis these *events* were triggered (determined) by large peaks on I_{is}. For time event when $I_{is}(t) > \langle I_{is}(t)\rangle + \sigma I_{is}(t)$ in a sufficiently wide time interval (as is shown in Fig.(4.3)), the time data $a(t)$ around this event was extracted and averaged. CAVs (let's denote it CAV(dt) where 2dt is time interval over which the time data was averaged) obtained in such a way are normalized to mean value and standard deviation in this thesis (that is $[CAV(\mathrm{dt}) - \langle a(2\mathrm{dt})\rangle]/\sigma a(2\mathrm{dt})$).
Two successive (blob-like) events also had to be separated by at last 1 autocorrelation time τ_c of $I_{is}(t)$ to distinguish individual blobs.
A sufficiently wide time interval satisfying the condition $I_{is}(t) > \langle I_{is}(t)\rangle + \sigma I_{is}(t)$ was used as $1/4\tau_c$ to avoid false signals.
The autocorrelation time τ_c of $I_{is}(t)$ in certain averaged radial probe head location was determined as time lag for which the cross-correlation function of $I_{is}(t)$ decreases on $1/e$ its maximum value (for zero time lag).

4.2 ESEL data and their processing

The two simulations from Danish group and the more than 13 simulations from J. Seidl in Prague was processed . The Danish simulations has time series of the density, electron temperature and plasma potential in hdf5 (hierarchical data format) files and the remaining have it in text files. Both have also as output 2D matrices of density, electron temperature and plasma potential (or vorticity) and they were used only to create a video in CD enclosed with this diploma thesis .

The most important output data were time series of the dimensionless density, electron temperature and plasma potential values that was gained by poloidal averaging (over the computing area shown in Fig.(3.5)) in a certain number of radial locations representing a model probes (the black dots in Fig.(3.5)) In most of the simulations there was 30 radial locations representing a 30 model probes.

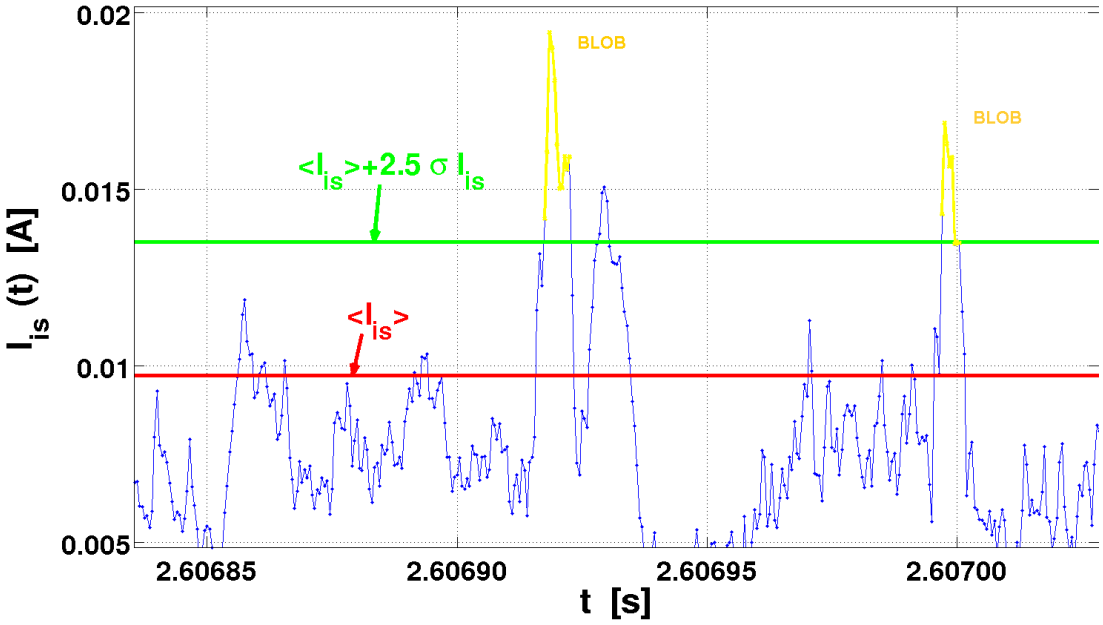

Figure 4.3: The I_{is} as function of time at position around 25mm *from LCFS. The yellow colour marks the peak satisfying the condition $I_{is}(t) > \langle I_{is}(t)\rangle + \sigma I_{is}(t)$ in a time interval greater than* 1/4 *of the autocorrelation time τ_c of $I_{is}(t)$.*

For each radial location the data was poloidally averaged and written to the output text file each 10th time step of the ESEL. So we had a time data sets for each from 30 radial locations similarly as in the case of the experimental data. It was only needed to multiply it with appropriate ESEL parameters in order to obtain the corresponding dimensional values. Further the data were processed in a similar manner as in the case of the experimental data. That is the $[\langle a\rangle](r)$, $[\sigma a/\langle a\rangle](r)$ and $\lambda(r) = -[\langle a\rangle/(\mathrm{d}\langle a\rangle)/\mathrm{d}r](r)$ ($a = n$, T_e or ϕ), CAVs and PDFs were calculated using by the program Matlab .

4.3 Comparison and discussion

We examined 15 different ESEL turbulence simulations matching ASDEX Upgrade tokamak plasma during the discharge #24349 (or #24348). First 2 simulations considers the last term in (3.11) in linear form (slower changes of plasma potential). They come from Danish group. Remaining 13 simulations had this term in exponential form (faster changes of plasma potential). They come from J. Seidl and they result from changing mainly the boundary conditions, neoclassical Pfirsch-Schlüter perpendicular collisional diffusion coefficient for particles $D'_{\perp n}$ and parallel loss time for particles $\tau'_{||n}$. The impact on the ESEL dynamic was observed and discussed 4.3.1, and some more general conclusions was claimed 4.3.2.

For clarity in the next results $\lambda(r)$ is not shown, it can be derived from $[\langle a\rangle](r)$. $\lambda(r)$ however gave us a valuable information. Also for clarity only the data from the discharge #24349 are shown - they are labeled "ASDEX9" in figures. The data from the discharge #24348 (same conditions as in the case of

the discharge #24349) are not shown because they are very similar to the data from the discharge #24349. They served mainly for verification of data from the discharge #24349.

The comparison results are shown on the figures. The experimental data as well as the ESEL data were computed for the ratio $T_i/T_e = 2$. The error bars in the figures of radial profiles of means represent the range of the ratio from $T_i/T_e = 1$ to $T_i/T_e = 10$. When comparing the ESEL and experiment I used the words as "good" and "bad", they are in meaning in comparison with experiment. The "good" means more in agreement with experiment and the "bad" means less in agreement with experiment. In the figures the first (from the left) vertical black dash line represents the LCFS and the second vertical black dash line represent the boundary between SOL and wall shadow. It is important to note that the plasma potential in the ESEL can be shifted by the constant that is there is not zero level of the electric potential energy. Therefore we can shift the radial profiles of means up or down. We can also add to it some of its derivative with respect to radial distance. It is because of absence a zero or first derivative (with respect to the space coordinates) of the plasma potential ϕ in the ESEL governing equations 3.3. It is also important to note that the CAVs in this and next chapter are not compared in the completely same locations in the SOL plasma. I verified the same conclusions we can say about the compared CAVs in more closer locations in the SOL plasma. In the figures the following labels were used:

- LE — Left Edge of the ESEl computation domain, e.g. $\phi'(LE)$ is the value of the plasma potential on the left edge of the ESEL computation domain;
- ASDEX9 — the data obtained from the probes during the discharge #24349;
- Doppler9 — the data obtained from the Doppler reflectometer during the discharge #24349;
- Thomson — the data obtained from the Thomson scattering during the discharge #24349;
- Thomson-fit — the fit of the Thomson scattering data;
- ASDEX9-gaussfit - the gaussian fit of the PDFs calculated from the ASDEX9 data
- $E_r(LE)$ means dimensionless $E'_r(LE)$.

4.3.1 Changing of the ESEL boundary conditions or parameters

In each of the following sections one or two important changes are presented and the corresponding simulations are described (I chose only a few essential parameters and boundary conditions). The all simulations match the ASDEX Upgrade tokamak plasma. For each change in the ESEL code it is shown for clarity only more significant impact on the ESEL dynamic.

Change of the form of the sheath dissipation (3.11) term from linear to exponential The 3 simulations were used. They are labeled "lin.", "lin., average" and "$\phi'(LE) = -40$".

- "lin." is the Danish simulation with job number 050. It has the sheet dissipation term in (3.11) in this linear form

$$\frac{1}{\tau'_{||n}} \frac{L_{||d}}{M_{||} 2 L_{||m}} \left[\frac{\phi'}{T'_e} - \alpha \right],$$

  and the following parameters and boundary conditions: $T_{e0} = T_{i0} = 30\text{eV}$, $n_0 = 1.5 \cdot 10^{19}\text{m}^{-3}$, $M_{||} = 1$, $E'_r(LE) = \text{d}\phi'/\text{d}x'(LE) = 0$, $n'(LE) = 2$, $T'_e(LE) = 2$.

- "lin., average" is also the Danish simulation with job number 051. It has the sheet dissipation term in (3.11) in this averaged linear form

$$\frac{1}{\tau'_{||n}} \frac{L_{||d}}{M_{||} 2 L_{||m}} \left[\frac{\langle \phi' \rangle}{\langle T'_e \rangle} - \alpha \right],$$

  where $\langle\rangle$ means average over the parallel direction y' of the ESEL computational domain, and the following parameters and boundary conditions: $T_{e0} = T_{i0} = 30\text{eV}$, $n_0 = 1.5 \cdot 10^{19}\text{m}^{-3}$, $M_{||} = 1$, $E'_r(LE) = 0$, $n'(LE) = 2$, $T'_e(LE) = 2$.

- "$\phi'(LE) = -40$" is the Prague simulation with job number 438. It has the sheet dissipation term in exponential form as we can see in (3.11) (the last term) and the all following simulations in this chapter are also Prague simulations with exponential form of the sheath dissipation term shown in (3.11). It has the following parameters and boundary conditions: $T_{e0} = 30\text{eV}$, $T_{i0} = 60\text{eV}$, $n_0 = 1.25 \cdot 10^{19}\text{m}^{-3}$, $M_{||} = 0.5$, $\phi'(LE) = -40$, $n'(LE) = 1.75$, $T'_e(LE) = 13.5$, $D'_{\perp n}$ is multiplied by factor 2, $1/\tau'_{||n}$ is multiplied by factor 1.

- $[\langle n \rangle](r)$ is still too flat (in comparison with experiment);
- $[\langle T_e \rangle](r)$ is slightly worse, but still good enough;
- $[\langle \phi \rangle](r)$ is better, almost as in experiment; 4.4
- $[\sigma n / \langle n \rangle](r)$ is better; 4.5
- $[\sigma T_e / \langle T_e \rangle](r)$ is still bad;

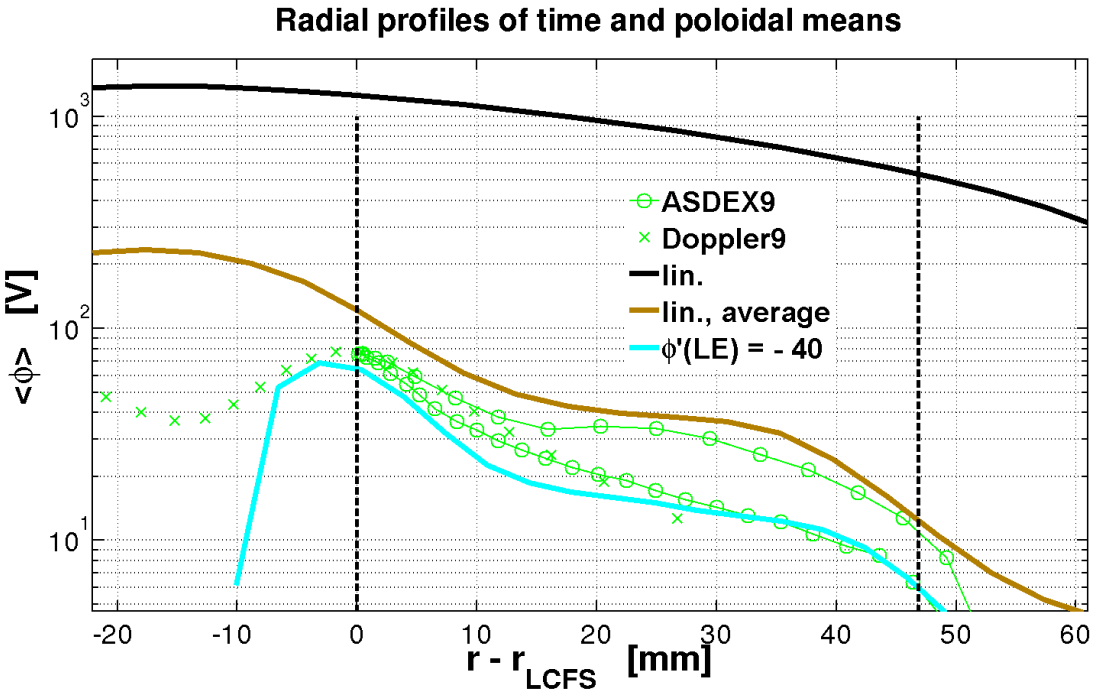

Figure 4.4: The radial profiles of the mean density. The simulations labeled "lin." and "lin., average" have linear form of the sheath dissipation term and the simulation labeled "$\phi'(LE) = -40$" has exponential form of the sheath dissipation term.

- $[\sigma\phi/\langle\phi\rangle](r)$ is still bad;
- CAVs of n and T_e remains relatively good;
- CAVs of ϕ are much better; 4.6

  In the case of the CAVs of electron temperature T_e and plasma potential ϕ however we can not pronounce a decisive conclusion, because the experimental results obtained from the discharge #24349 (or #24348) are probably wrong (CAVs of electron temperature have a negative peak 4.7 and CAV of plasma potential has one positive and one negative peak in the area far from the LCFS 4.6). This problem, mainly about CAVs of the T_e is discussed in [42] where the same experimental data were used. The CAVs of the T_e should surely have a positive peak. And the experimental CAV of the ϕ (as show ESEL provided that there is the sheath dissipation term) should have according to us also a one positive peak without negative peak. This view is substantiated by other experimental results from ASDEX Upgrade tokamak as we can see in [64].

- PDFs of n are better, mainly far from the LCFS; 4.8
- PDFs of T_e and ϕ are still relatively good, mainly far from the LCFS.

The Change of the form of the sheath dissipation term from linear to exponential produces better results without worse results. Therefore further in this chapter only Prague simulations with exponential form of the sheath dissipation

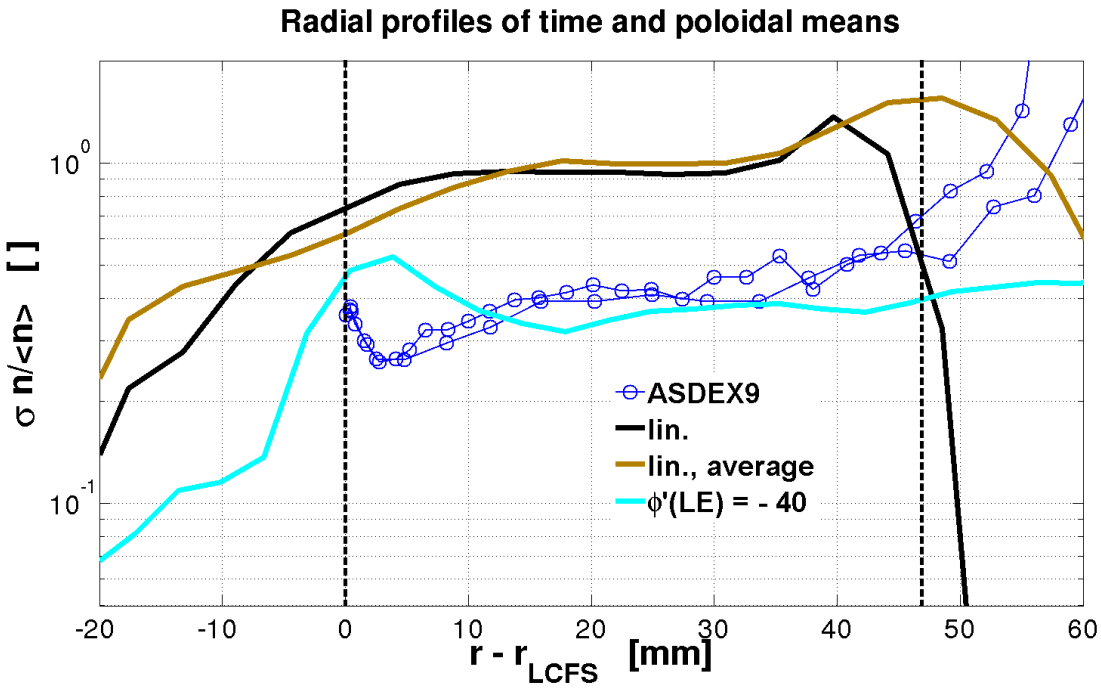

Figure 4.5: The radial profiles of the relative density fluctuations.

term are shown.

Changes of ϕ'(LE) and T_e'(LE))

The 6 simulations were used. They are labeled "$\phi'(LE) = -40/T_e'(LE) = 13.5$", "$\phi'(LE) = -36/T_e'(LE) = 13.5$", "$\phi'(LE) = -40/T_e'(LE) = 20$" and "$\phi'(LE) = -36/T_e'(LE) = 20$".

- "$\phi'(LE) = -40/T_e'(LE) = 13.5$" is the simulation $\phi'(LE) = -40$ with job number 438 described above. It has the following parameters and boundary conditions: $T_{e0} = 30\text{eV}$, $T_{i0} = 60\text{eV}$, $n_0 = 1.25 \cdot 10^{19}\text{m}^{-3}$, $M_{||} = 0.5$, $\phi'(LE) = -40$, $n'(LE) = 1.75$, $T_e'(LE) = 13.5$, $D'_{\perp n}$ is multiplied by factor 2, $1/\tau'_{||n}$ is multiplied by factor 1.

- "$\phi'(LE) = -36/T_e'(LE) = 13.5$" is the Prague simulation with job number 338. It has the following parameters and boundary conditions: $T_{e0} = 30\text{eV}$, $T_{i0} = 60\text{eV}$, $n_0 = 1.25 \cdot 10^{19}\text{m}^{-3}$, $M_{||} = 0.5$, $\phi'(LE) = -36$, $n'(LE) = 1.75$, $T_e'(LE) = 13.5$, $D'_{\perp n}$ is multiplied by factor 2, $1/\tau'_{||n}$ is multiplied by factor 1.

- "$\phi'(LE) = -40/T_e'(LE) = 20$" is the Prague simulation with job number 462. It has the following parameters and boundary conditions: $T_{e0} = 30\text{eV}$, $T_{i0} = 60\text{eV}$, $n_0 = 1.25 \cdot 10^{19}\text{m}^{-3}$, $M_{||} = 0.5$, $\phi'(LE) = -40$, $n'(LE) = 1.75$, $T_e'(LE) = 20$, $D'_{\perp n}$ is multiplied by factor 2, $1/\tau'_{||n}$ is multiplied by factor 1.

- "$\phi'(LE) = -40/T_e'(LE) = 20$" is the Prague simulation with job number 448. It has the following parameters and boundary conditions: $T_{e0} = 30\text{eV}$, $T_{i0} = 60\text{eV}$, $n_0 = 1.25 \cdot 10^{19}\text{m}^{-3}$, $M_{||} = 0.5$, $\phi'(LE) = -36$, $n'(LE) = 1.75$, $T_e'(LE) = 20$, $D'_{\perp n}$ is multiplied by factor 2, $1/\tau'_{||n}$ is multiplied by factor 1.

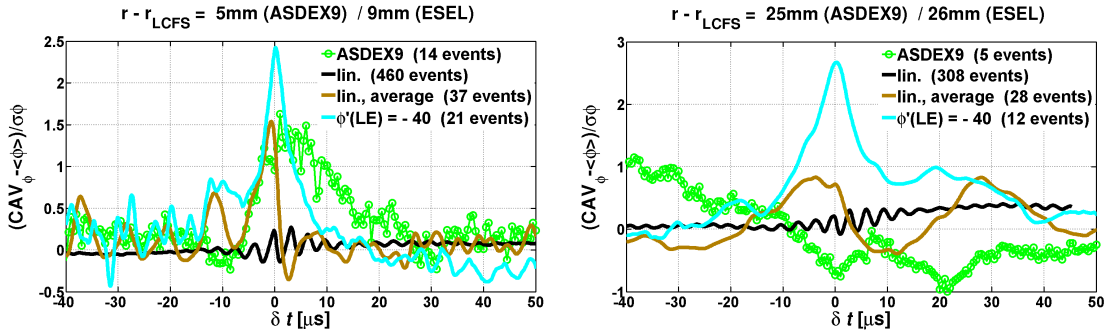

Figure 4.6: Conditional average (CAV) of the plasma potential ϕ computed near the LCFS (left) and far from the LCFS (right). Far from the LCFS has experimental CAV one negative and one positive peak, but model CAV has only one positive peak.

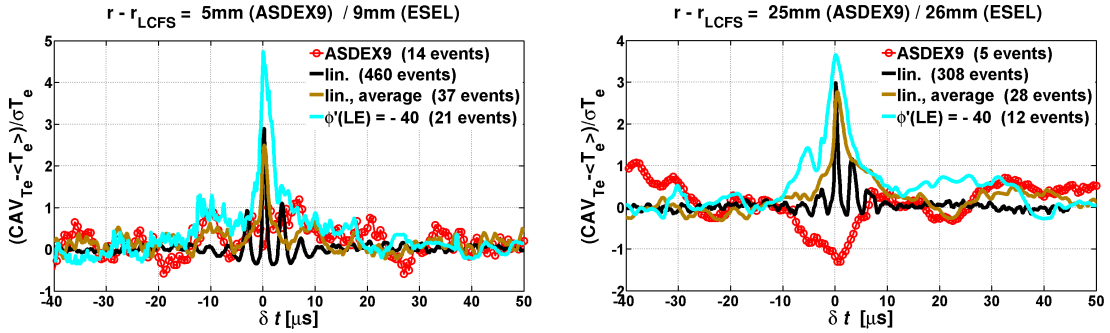

Figure 4.7: Conditional average (CAV) of the electron temperature T_e computed near the LCFS (left) and far from the LCFS (right). Far from the LCFS has experimental CAV one negative peak, but model CAV has one positive peak.

These changes of $\phi'(LE)$ and T'_e(LE) was too small to observe a significant impact on the ESEL dynamic. However we can see a trend in the drop of the radial density profile if the $\phi'(LE)$ increase 4.9.

But one change, the change of T'_e(LE) at E'_r(LE $= 1.25$ had a significant impact on the ESEL dynamic. For this change the 2 simulations were used. They are labeled "$T'_e(LE) = 13.5$" and "$T'_e(LE) = 20$".

- "$T'_e(LE) = 13.5$" is the Prague simulation with job number 505. It has the following parameters and boundary conditions: $T_{e0} = 30$eV, $T_{i0} = 60$eV, $n_0 = 1.25 \cdot 10^{19}\mathrm{m}^{-3}$, $M_{||} = 0.5$, $E'_r(LE) = 1.25$, $n'(LE) = 1.75$, $T'_e(LE) = 13.5$, $D'_{\perp n}$ is multiplied by factor 2, $1/\tau'_{||n}$ is multiplied by factor 1.

- "$T'_e(LE) = 20$" is the Prague simulation with job number 557. It has the following parameters and boundary conditions: $T_{e0} = 30$eV, $T_{i0} = 60$eV, $n_0 = 1.25 \cdot 10^{19}\mathrm{m}^{-3}$, $M_{||} = 0.5$, $E'_r(LE) = 1.25$, $n'(LE) = 1.75$, $T'_e(LE) = 20$, $D'_{\perp n}$ is multiplied by factor 2, $1/\tau'_{||n}$ is multiplied by factor 1.

The increase in T'_e(LE) results in the following:

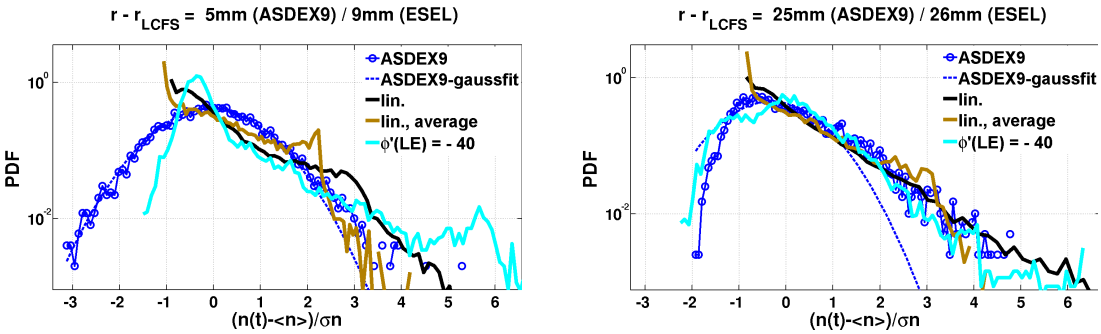

Figure 4.8: PDF of the density n calculated near the LCFS (left) and far from the LCFS (right). The exponential form of the sheath dissipation term results in good agreement with experiment in the location far from the LCFS.

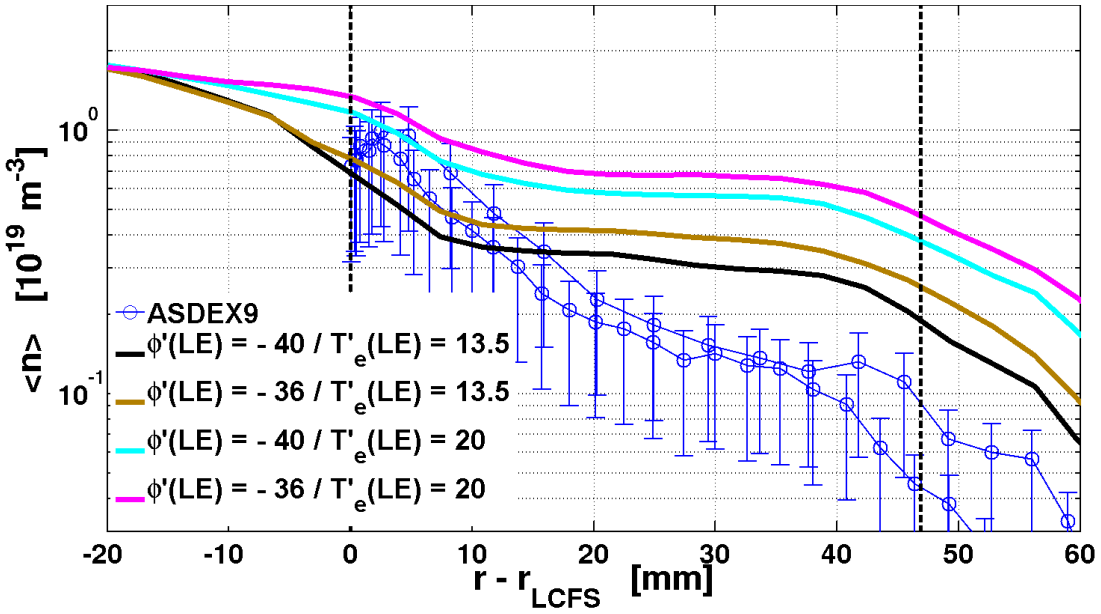

Figure 4.9: The radial profiles of the mean density $\langle n \rangle$. If the $\phi'(LE)$ increase, the profiles drop.

- $[\langle n \rangle](r)$ becomes much more flatter and raises - less in agreement with experiment; 4.10
- $[\langle T_e \rangle](r)$ becomes more flatter and raises - more in agreement with experiment; 4.11
- $[\langle \phi \rangle](r)$ raises - less in agreement with experiment; 4.12
- $[\sigma n / \langle n \rangle](r)$ becomes too small compared to the experiment; 4.13
- PDFs of n become better near the LCFS but worse far from the LCFS. 4.14

Change of E'_r(LE)

The 2 simulations were used. They are labeled "$E_r(LE) = 1.25$" and "$E_r(LE) = 1.20$".

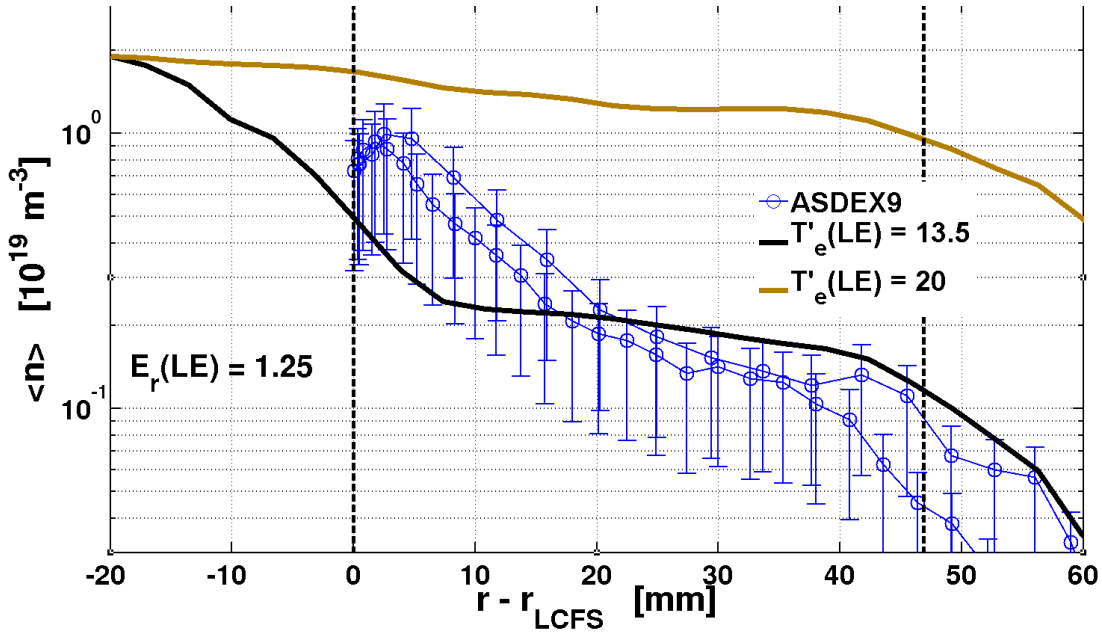

Figure 4.10: The radial profiles of the mean density $\langle n \rangle$. Increase in $T'_e(\mathrm{LE})$ at $E'_r(\mathrm{LE} = 1.25$ results in much more flatter and high placed profile.

- "$E_r(LE) = 1.25$" is the simulation $T'_e(LE) = 13.5$ with job number 505 described above. It has the following parameters and boundary conditions: $T_{e0} = 30\mathrm{eV}$, $T_{i0} = 60\mathrm{eV}$, $n_0 = 1.25 \cdot 10^{19}\mathrm{m}^{-3}$, $M_{||} = 0.5$, $E'_r(LE) = 1.25$, $n'(LE) = 1.75$, $T'_e(LE) = 13.5$, $D'_{\perp n}$ is multiplied by factor 2, $1/\tau'_{||n}$ is multiplied by factor 1.

- "$E_r(LE) = 1.20$" is the Prague simulation with job number 546. It has the following parameters and boundary conditions: $T_{e0} = 30\mathrm{eV}$, $T_{i0} = 60\mathrm{eV}$, $n_0 = 1.25 \cdot 10^{19}\mathrm{m}^{-3}$, $M_{||} = 0.5$, $E'_r(LE) = 1.20$, $n'(LE) = 1.75$, $T'_e(LE) = 13.5$, $D'_{\perp n}$ is multiplied by factor 2, $1/\tau'_{||n}$ is multiplied by factor 1.

This change at $T'_e(\mathrm{LE}) = 13.5$ has again only negligible impact on the ESEL dynamic (probably within the statistical error). Again we can see the trend in the drop of the radial mean density profile if the $E'_r(\mathrm{LE}$ increase. 4.15

Changes of $D'_{\perp n}$

The 4 simulations were used. They are labeled "$1.5 \times D'_{\perp n}$", "$3 \times D'_{\perp n}$", "$6 \times D'_{\perp n}$" and "$12 \times D'_{\perp n}$".

- "$1.5 \times D'_{\perp n}$" is the Prague simulation with job number 655. It has the following parameters and boundary conditions: $T_{e0} = 30\mathrm{eV}$, $T_{i0} = 60\mathrm{eV}$, $n_0 = 1.25 \cdot 10^{19}\mathrm{m}^{-3}$, $M_{||} = 0.5$, $E'_r(LE) = 1.20$, $n'(LE) = 1.75$, $T'_e(LE) = 13.5$, $D'_{\perp n}$ is multiplied by factor 1.5, $1/\tau'_{||n}$ is multiplied by factor 1.

- "$1.5 \times D'_{\perp n}$" is the Prague simulation with job number 656. It has the following parameters and boundary conditions: $T_{e0} = 30\mathrm{eV}$, $T_{i0} = 60\mathrm{eV}$, $n_0 = 1.25 \cdot 10^{19}\mathrm{m}^{-3}$, $M_{||} = 0.5$, $E'_r(LE) = 1.20$, $n'(LE) = 1.75$, $T'_e(LE) = 13.5$, $D'_{\perp n}$ is multiplied by factor 3, $1/\tau'_{||n}$ is multiplied by factor 1.

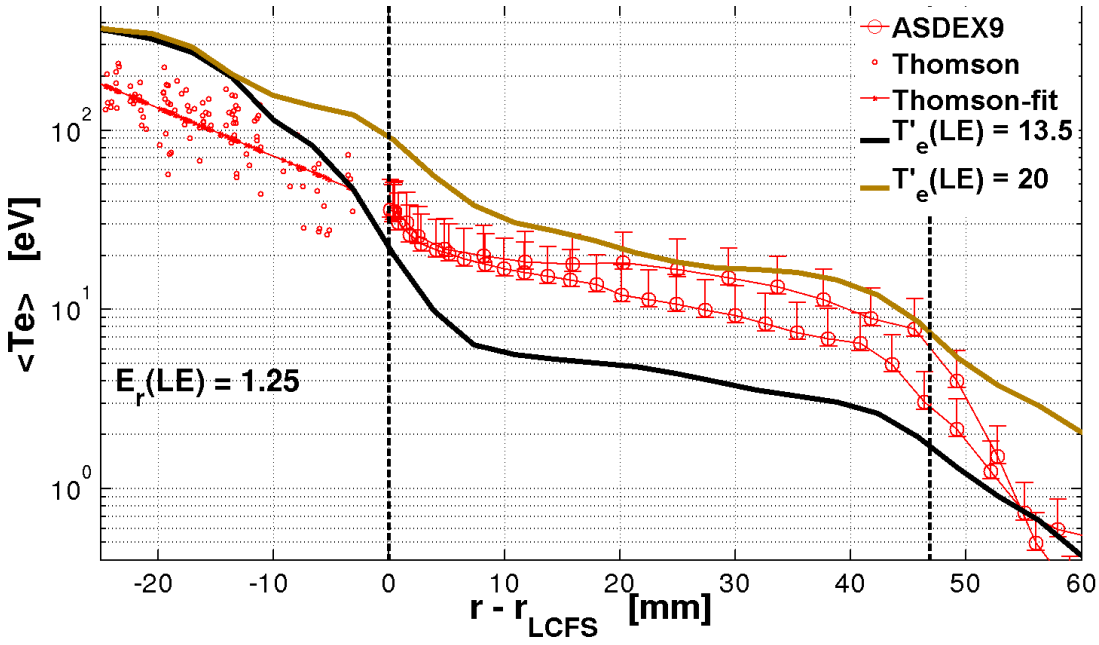

Figure 4.11: The radial profiles of the mean electron temperature $\langle T_e \rangle$. Increase in $T'_e(\mathrm{LE})$ at $E'_r(\mathrm{LE} = 1.25$ results in more flatter and higher placed profile.

- "$1.5 \times D'_{\perp n}$" is the Prague simulation with job number 665. It has the following parameters and boundary conditions: $T_{e0} = 30\mathrm{eV}$, $T_{i0} = 60\mathrm{eV}$, $n_0 = 1.25 \cdot 10^{19}\mathrm{m}^{-3}$, $M_{||} = 0.5$, $E'_r(LE) = 1.20$, $n'(LE) = 1.75$, $T'_e(LE) = 13.5$, $D'_{\perp n}$ is multiplied by factor 6, $1/\tau'_{||n}$ is multiplied by factor 1.

- "$1.5 \times D'_{\perp n}$" is the Prague simulation with job number 675. It has the following parameters and boundary conditions: $T_{e0} = 30\mathrm{eV}$, $T_{i0} = 60\mathrm{eV}$, $n_0 = 1.25 \cdot 10^{19}\mathrm{m}^{-3}$, $M_{||} = 0.5$, $E'_r(LE) = 1.20$, $n'(LE) = 1.75$, $T'_e(LE) = 13.5$, $D'_{\perp n}$ is multiplied by factor 12, $1/\tau'_{||n}$ is multiplied by factor 1.

Extent of the changes of $D'_{\perp n}$ was large enough to observe significant impact on the ESEL dynamic. The increase in $D'_{\perp n}$ results in the following:

- $[\langle n \rangle](r)$ becomes steeper and drops - more in agreement with experiment; 4.16

- $[\langle T_e \rangle](r)$ and $[\langle \phi \rangle](r)$ drops - less in agreement with the experiment; 4.17, 4.18

- $[\sigma n/\langle n \rangle](r)$ becomes too small compared to the experiment; 4.19

- $[\sigma T_e/\langle T_e \rangle](r)$ and $[\sigma \phi/\langle \phi \rangle](r)$ becomes smaller - more in agreement with the experiment : 4.20, 4.21

The simulation $12 \times D'_{\perp n}$ has finally almost as steep mean density profile 4.16 as we can seen in the experiment - it can be shifted up by the choice of the greater value of density n_0 at the LCFS. But we have seen that this simulation is very probably not good. It corresponds to a SOL plasma almost without blobs ("bubbling plasma") as we can see in CAVs of n 4.22 (3 events near the LCFS and

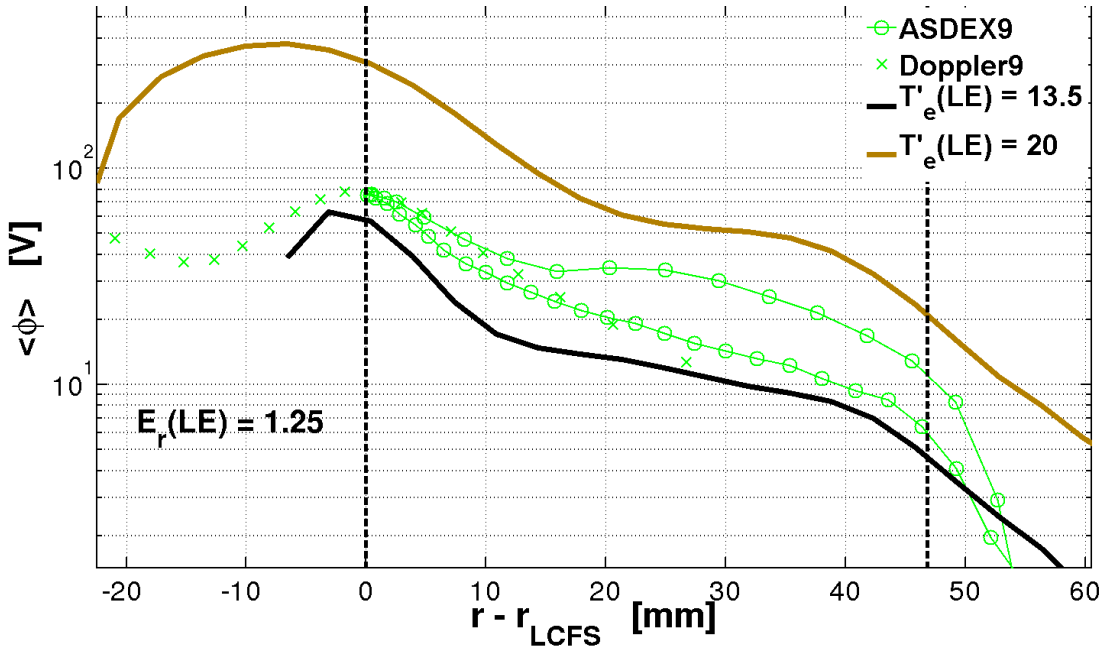

Figure 4.12: The radial profiles of the mean plasma potential $\langle\phi\rangle$. Increase in $T'_e(\mathrm{LE})$ at $E'_r(\mathrm{LE} = 1.25$ results in higher placed profile.

1 event far from the LCFS) or for example in PDFs of T_e 4.23 (almost Gaussian probability distribution corresponding to the state without blobs).

Changes of $1/\tau'_{||n}$

The 2 simulations were used. They are labeled "$1.5/\tau'_{||n}$" and "$3/\tau'_{||n}$".

- "$1.5/\tau'_{||n}$" is the Prague simulation with job number 771. It has the following parameters and boundary conditions: $T_{e0} = 30\mathrm{eV}$, $T_{i0} = 60\mathrm{eV}$, $n_0 = 1.25 \cdot 10^{19}\mathrm{m}^{-3}$, $M_{||} = 0.5$, $E'_r(LE) = 1.20$, $n'(LE) = 1.75$, $T'_e(LE) = 13.5$, $D'_{\perp n}$ is multiplied by factor 2, $1/\tau'_{||n}$ is multiplied by factor 1.5.

- "$3/\tau'_{||n}$" is the Prague simulation with job number 772. It has the following parameters and boundary conditions: $T_{e0} = 30\mathrm{eV}$, $T_{i0} = 60\mathrm{eV}$, $n_0 = 1.25 \cdot 10^{19}\mathrm{m}^{-3}$, $M_{||} = 0.5$, $E'_r(LE) = 1.20$, $n'(LE) = 1.75$, $T'_e(LE) = 13.5$, $D'_{\perp n}$ is multiplied by factor 2, $1/\tau'_{||n}$ is multiplied by factor 3.

The change of $1/\tau'_{||n}$ was not large enough to observe some significant (beyond the extend of the statistical error) impact on the radial profiles of means $[\langle n\rangle](r)$, $[\langle T_e\rangle](r)$, $[\langle\phi\rangle](r)$, CAVs of n, T_e, ϕ or PDFs of n, T_e, ϕ. But we can see that decrease in parallel loss times for particle density $1/\tau'_{||n}$ (increase in parallel losses of particle density) results in the following:

- $[\sigma n/\langle n\rangle](r)$ becomes too big compared to the experiment ; 4.24
- $[\sigma T_e/\langle T_e\rangle](r)$ and $[\sigma\phi/\langle\phi\rangle](r)$ becomes bigger - less in agreement with experiment : 4.25, 4.26

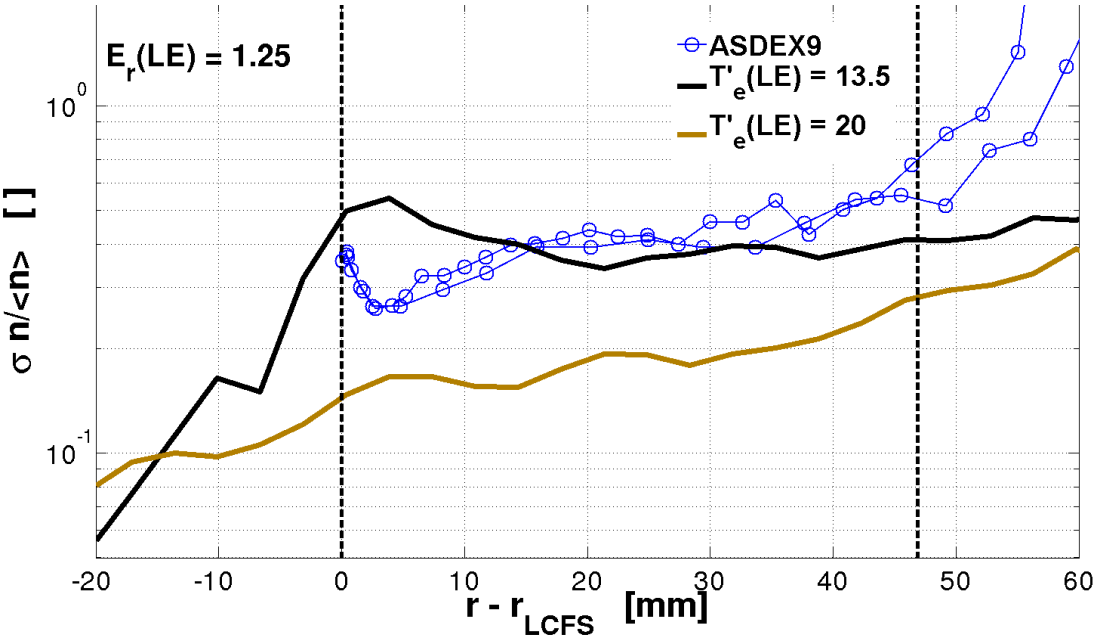

Figure 4.13: The radial profiles of the relative density fluctuations. Increase in $T'_e(\mathrm{LE})$ at $E'_r(\mathrm{LE} = 1.25$ results in too small fluctuations.

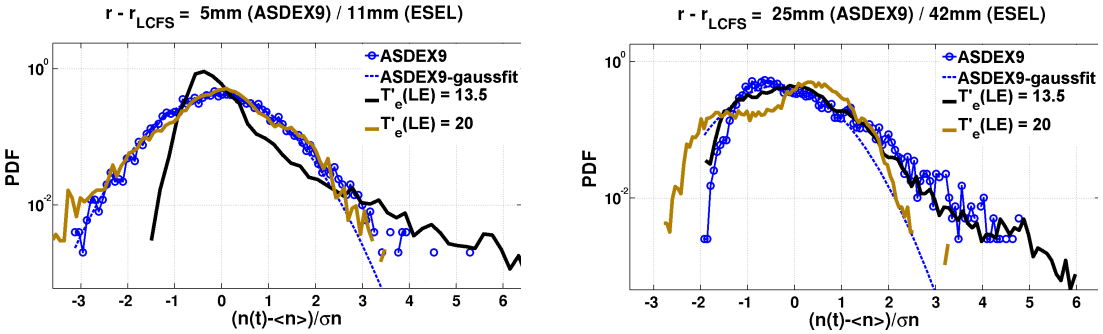

Figure 4.14: PDF of the density n calculated near the LCFS (left) and far from the LCFS (right). Increase in $T'_e(\mathrm{LE})$ at $E'_r(\mathrm{LE} = 1.25$ results in good PDF near the LCFS but bad PDF far from the LCFS.

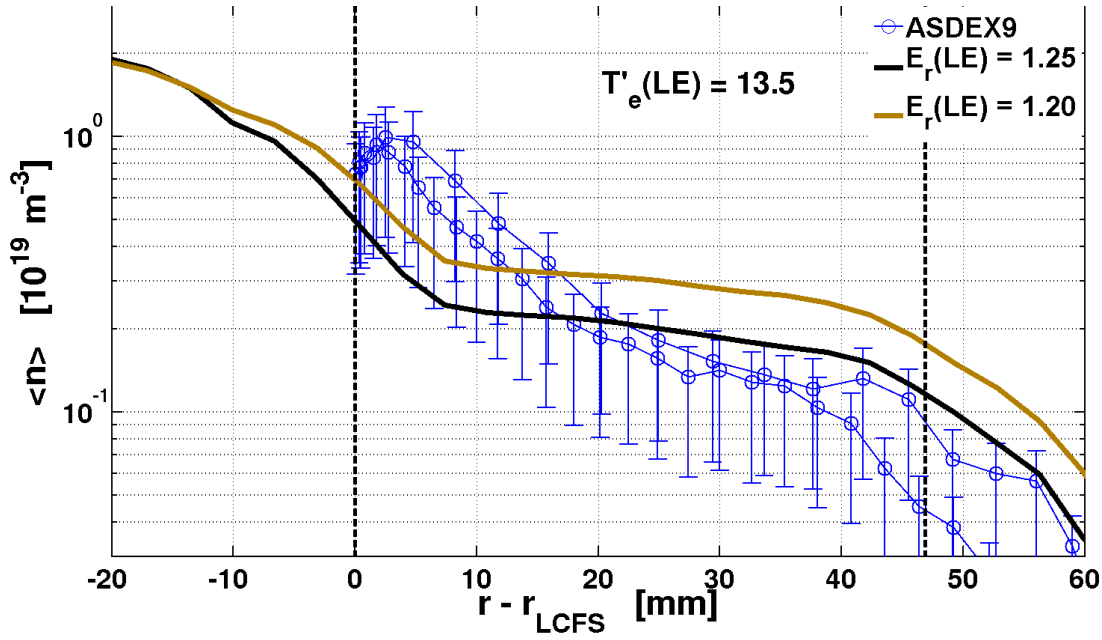

Figure 4.15: The radial profiles of the mean density $\langle n \rangle$. If the E'_r(LE increase, the profile drops.

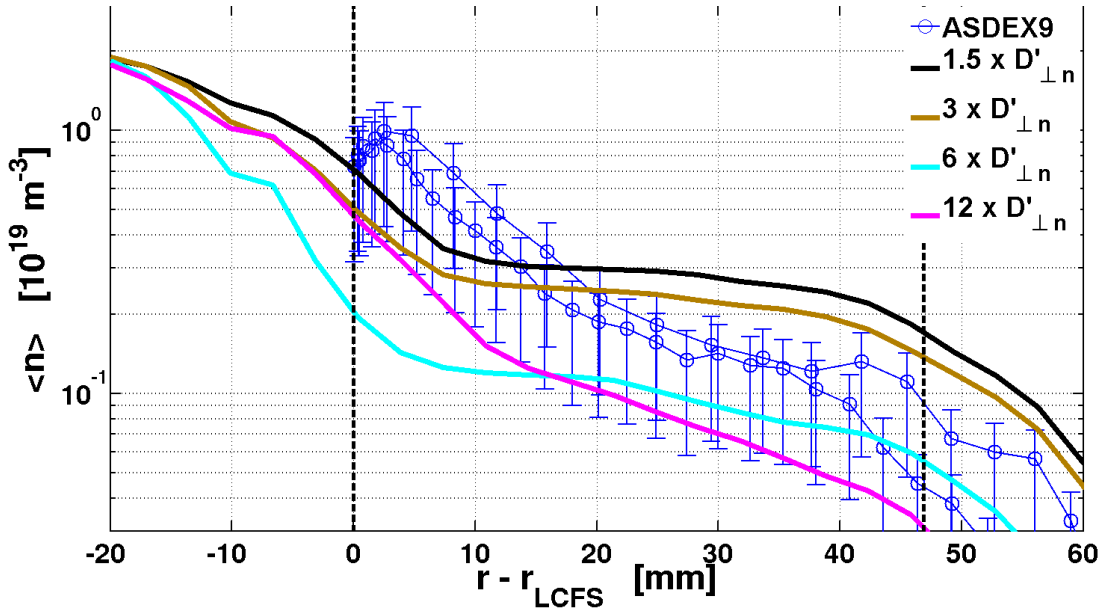

Figure 4.16: The radial profiles of the mean density $\langle n \rangle$. Increase in $D'_{\perp n}$ results in steeper and dropped profile.

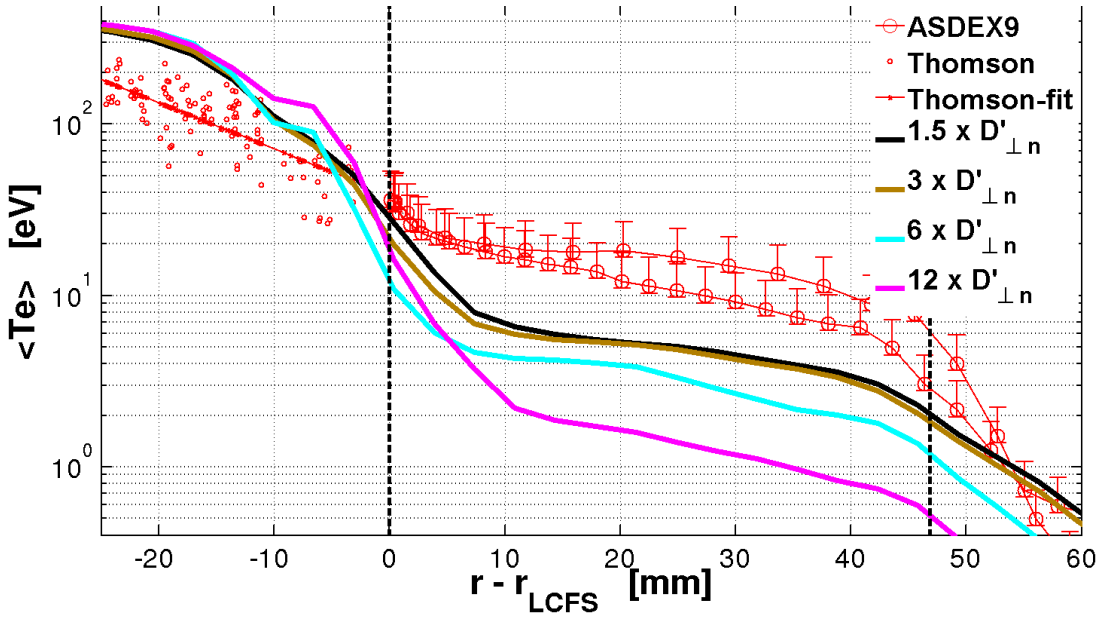

Figure 4.17: The radial profiles of the mean electron temperature $\langle T_e \rangle$. Increase in $D'_{\perp n}$ results in dropped profile.

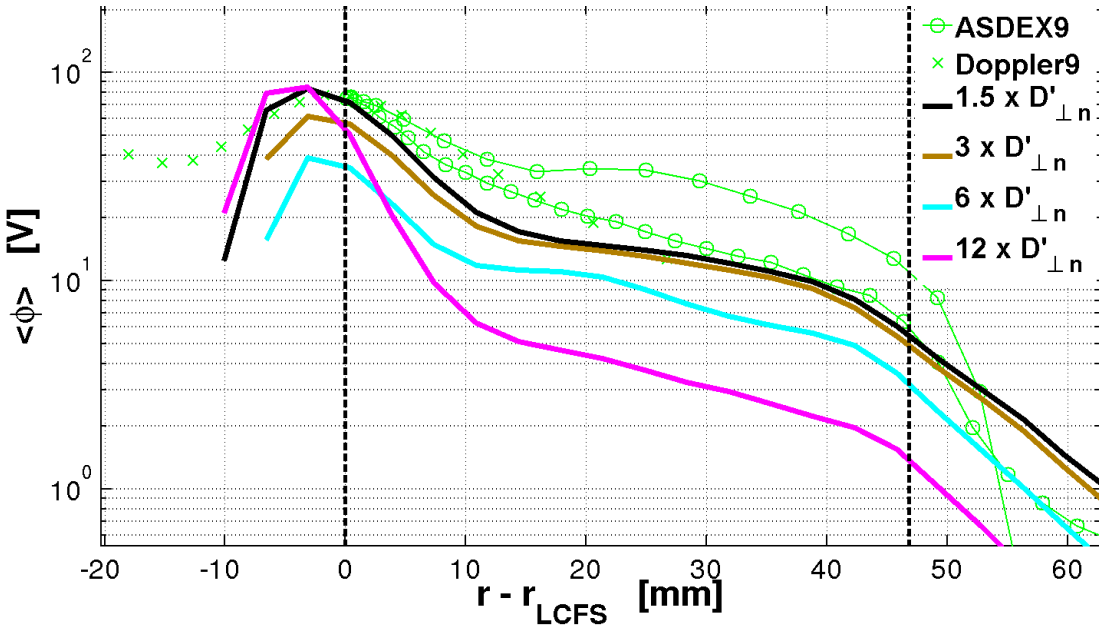

Figure 4.18: The radial profiles of the mean plasma potential $\langle \phi \rangle$. Increase in $D'_{\perp n}$ results in dropped profile.

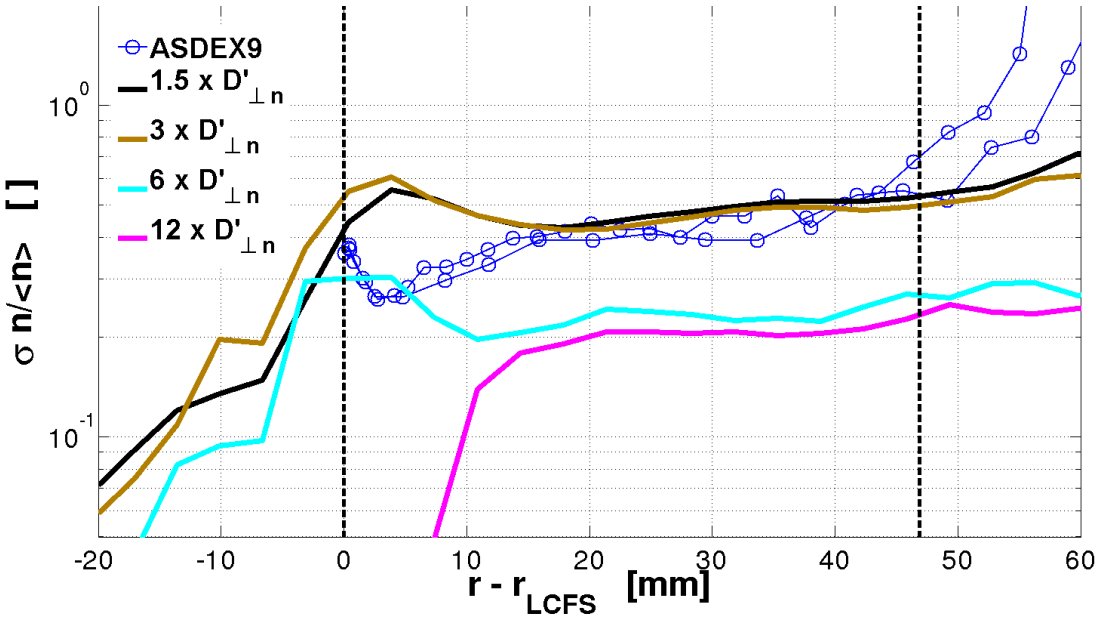

Figure 4.19: The radial profiles of the relative density fluctuations. Increase in $D'_{\perp n}$ results in too small fluctuations.

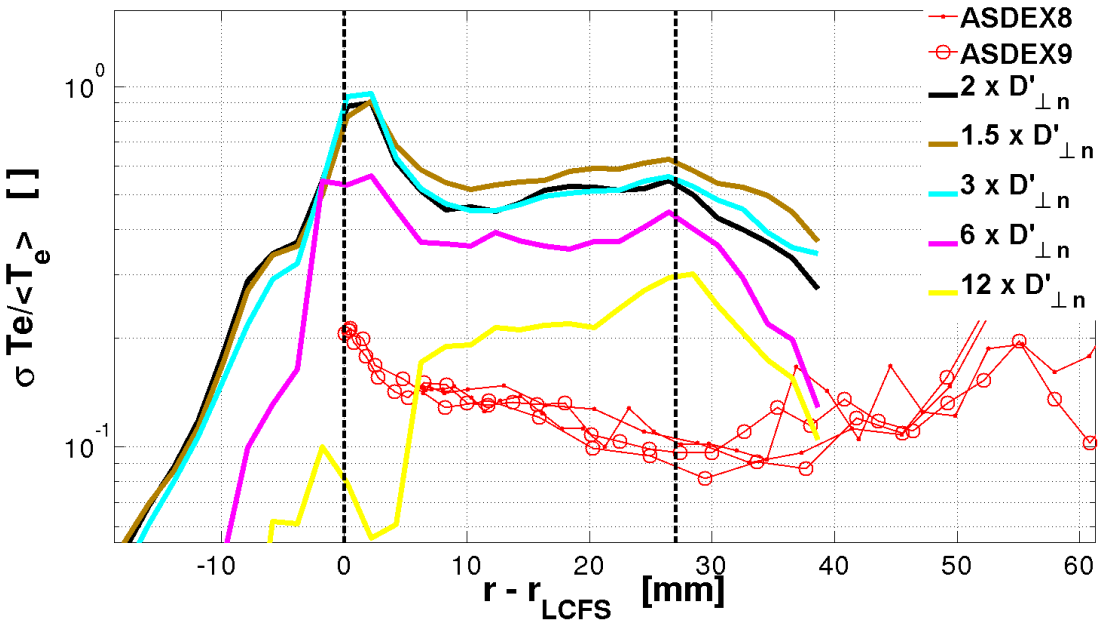

Figure 4.20: The radial profiles of the relative electron temperature fluctuations. Increase in $D'_{\perp n}$ results in smaller fluctuations.

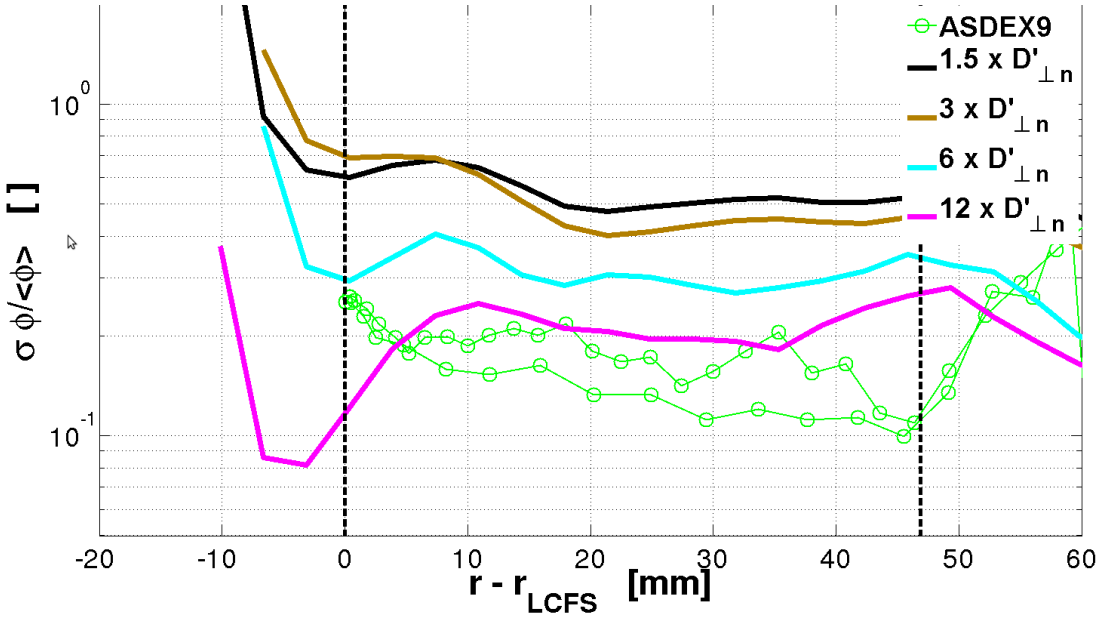

Figure 4.21: The radial profiles of the relative plasma potential fluctuations. Increase in $D'_{\perp n}$ results in smaller fluctuations.

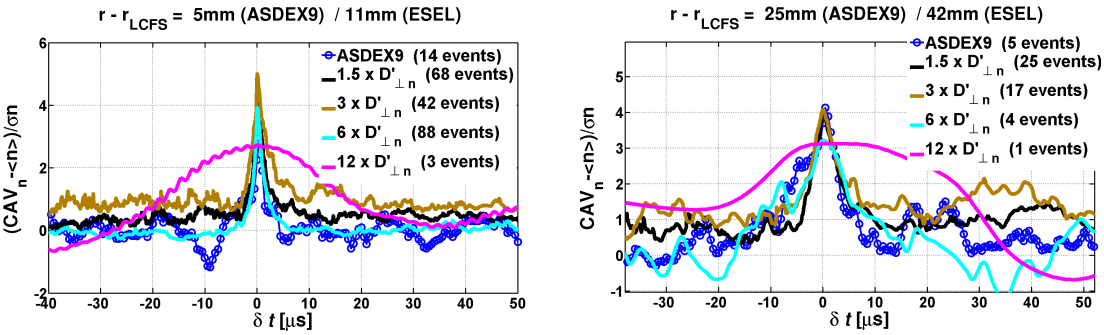

Figure 4.22: Conditional average (CAV) of the density n computed near the LCFS (left) and far from the LCFS (right). Excessive increase in $D'_{\perp n}$ results in SOL plasma almost without blobs.

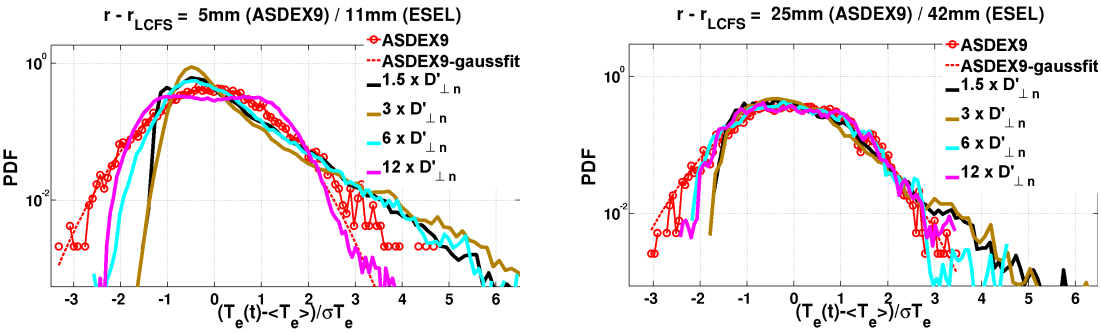

Figure 4.23: PDF of the density n calculated near the LCFS (left) and far from the LCFS (right). Excessive increase in $D'_{\perp n}$ results in almost Gaussian PDF.

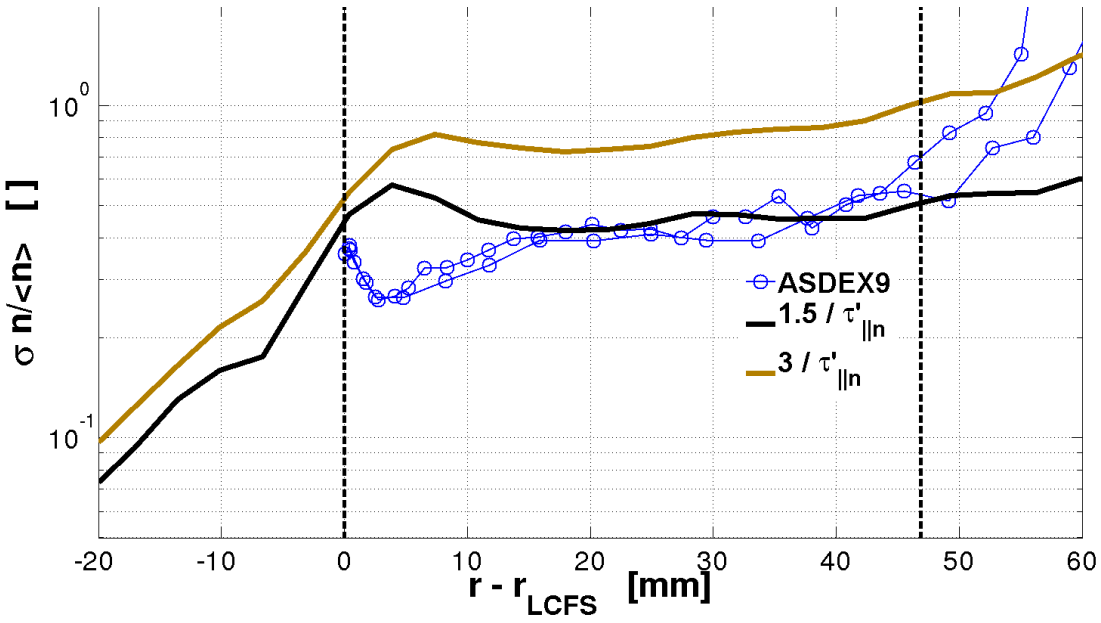

Figure 4.24: The radial profiles of the relative density fluctuations. Increase in parallel losses of particle density results in too big fluctuations.

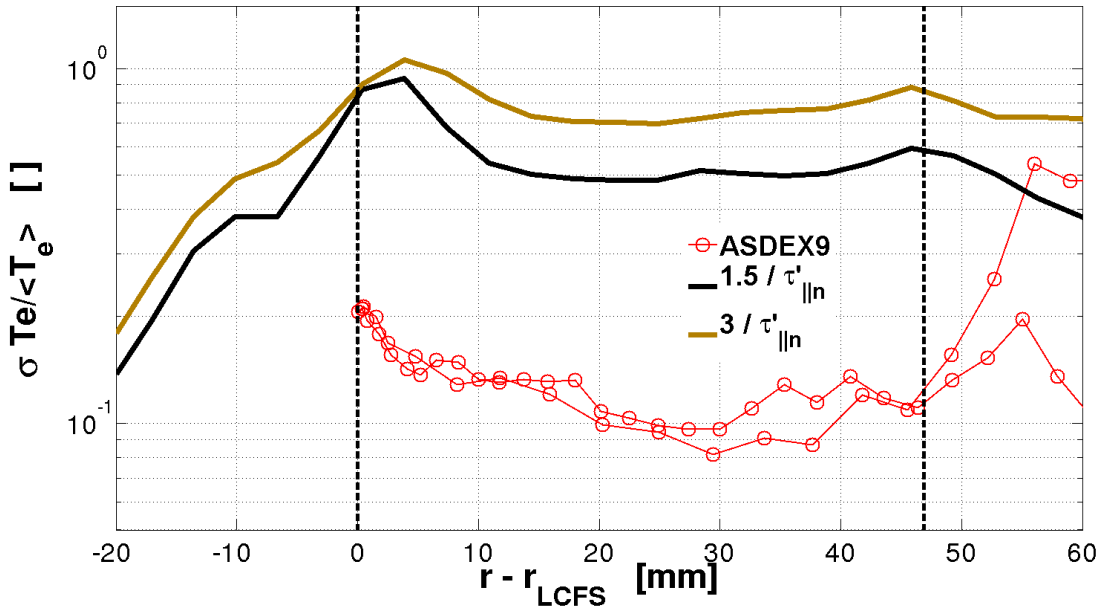

Figure 4.25: The radial profiles of the relative electron temperature fluctuations. Increase in parallel losses of particle density results in bigger fluctuations.

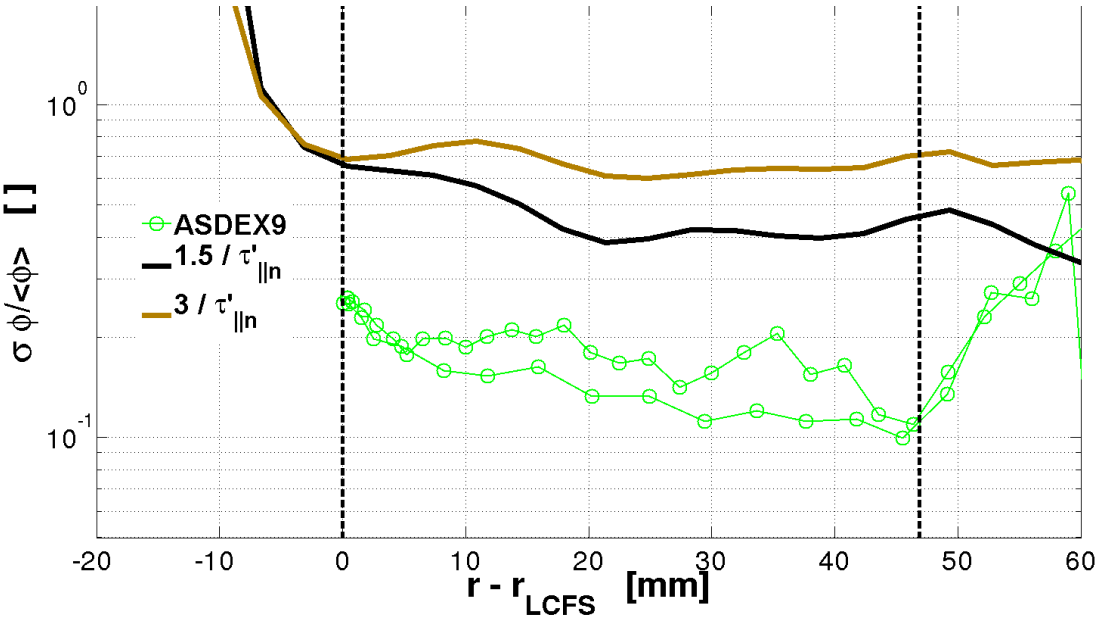

Figure 4.26: The radial profiles of the relative plasma potential fluctuations. Increase in parallel losses of particle density results in bigger fluctuations.

4.3.2 General conclusions

On the basis of the comparisons in 4.3.1 corresponding to the ASDEX Upgrade tokamak we also can say some more general conclusions about the current ESEL model with exponential form of sheath dissipation term (the last term in (3.11))matching the ASDEX Upgrade tokamak plasma. The claims are supported by a figures. For clarity I chose always only one (only in one case two) most representative simulation for each claim. The conclusions are checked with results of 3 the ESEL simulations matching the COMPASS tokamak plasma in the next chapter 5.

ESEL simulations with exponential form of the sheath dissipation term matching the ASDEX Upgrade tokamak plasma are in general able to **well describe** (relatively) the following:

- the radial profiles of the mean electron temperature; 4.27

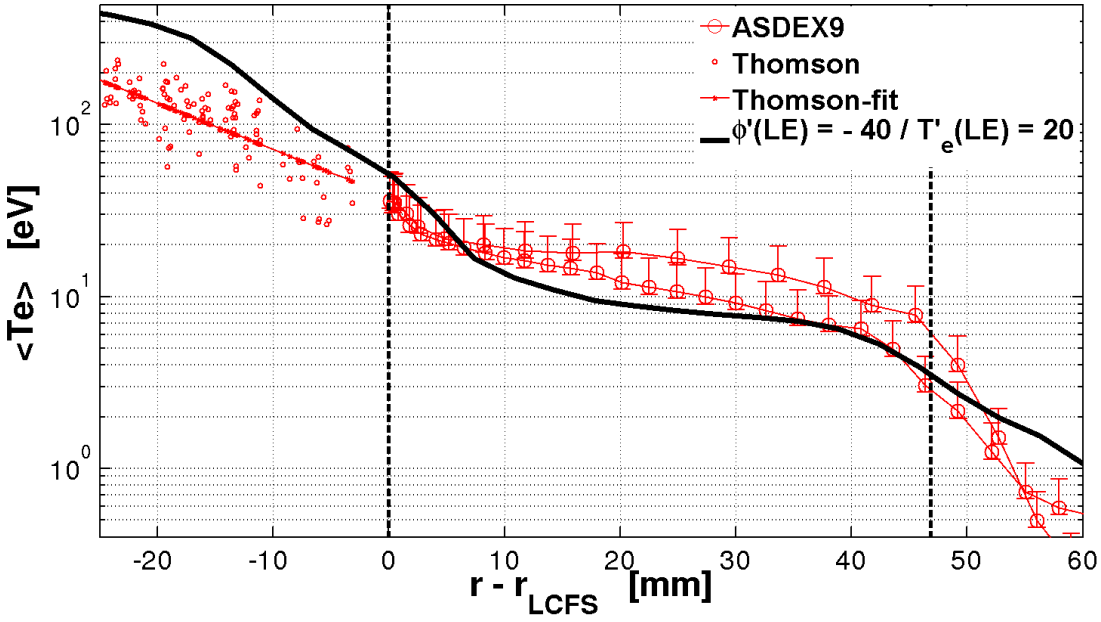

Figure 4.27: The radial profiles of the mean electron temperature $\langle T_e \rangle$. Good agreement with experiment.

- the radial profiles of the mean plasma potential $\langle \phi \rangle$; 4.28
- except the are near and far from the LCFS, the radial profiles of the relative density fluctuations; 4.29
- the normalized (on mean and standard deviation) CAVs of density provided that neoclassical perpendicular collisional diffusion coefficient for particles $D'_{\perp n}$is not large enough; 4.22
- the normalized PDFs of density n, electron temperature T_e and plasma potential ϕ in far SOL plasma. 4.30, 4.31

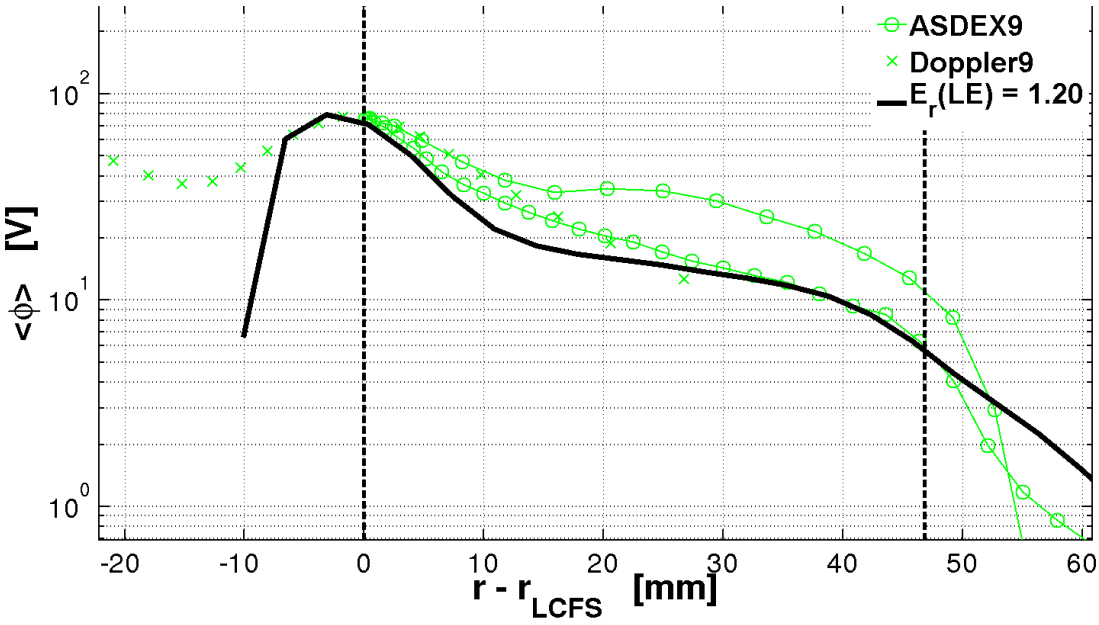

Figure 4.28: The radial profiles of the mean plasma potential $\langle\phi\rangle$. Good agreement with experiment.

But it is at the cost of other discrepancies. ESEL simulations with exponential form of the sheath dissipation term matching the ASDEX Upgrade tokamak plasma in general **badly describe** the following:

- the radial profiles of the mean density $\langle n\rangle$; 4.16
- the radial profiles of the relative electron temperature fluctuations ; 4.25
- the radial profiles of the relative plasma potential fluctuations; 4.21
- near the LCFS, the normalized PDFs of density n, electron temperature T_e and plasma potential ϕ. 4.20, 4.32

The fact that ESEL poorly describes the normalized PDFs of density n, electron temperature T_e and plasma potential ϕ near the LCFS can be due to the presence of a Gaussian noise in the experimental data and also due to the fact that in the vicinity of the LCFS a drift waves and other aspects neglected by the ESEL model play a role.

As mentioned before 4.3.1 in the case of the CAVs of electron temperature T_e and plasma potential ϕ we can not pronounce a decisive conclusion, because the experimental results obtained from the discharge #24349 (or #24348) are probably wrong.

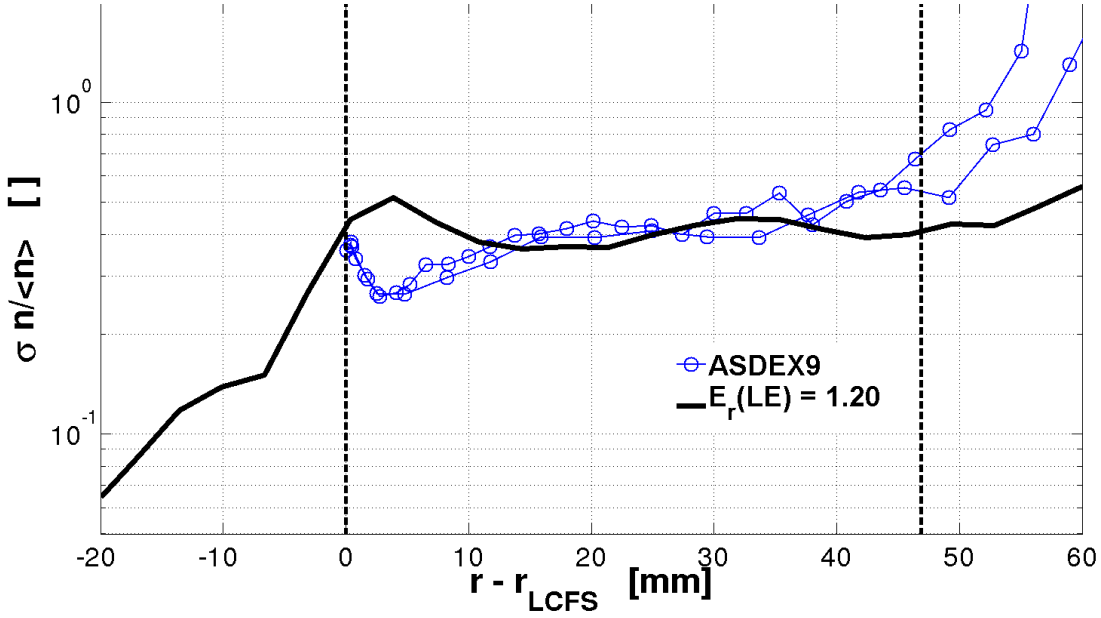

Figure 4.29: The radial profiles of the relative density fluctuations. Good agreement with experiment in the middle of the SOL.

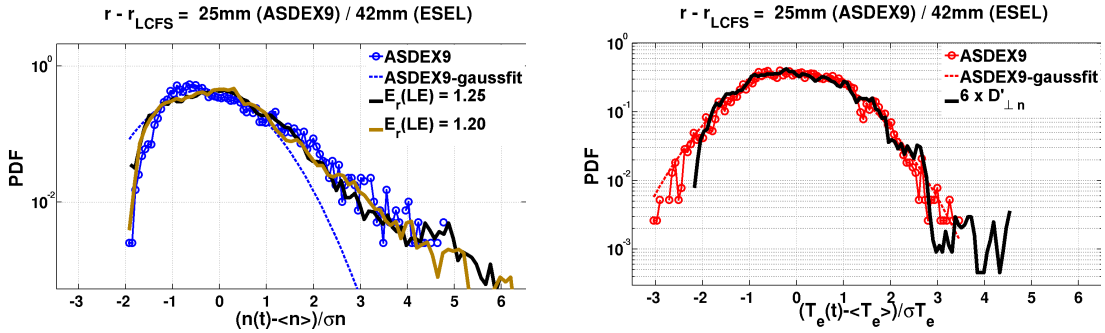

Figure 4.30: PDF of the density n (left) and electron temperature T_e (right) calculated far from the LCFS. Good agreement with experiment.

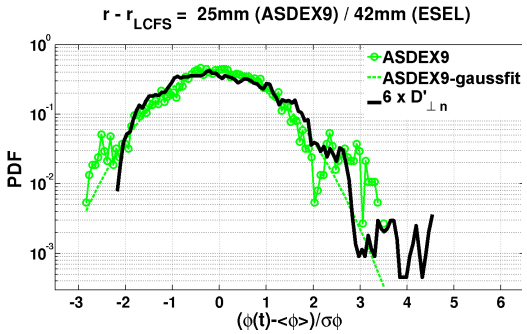

Figure 4.31: PDF of the plasma potential ϕ calculated far from the LCFS . Good agreement with experiment.

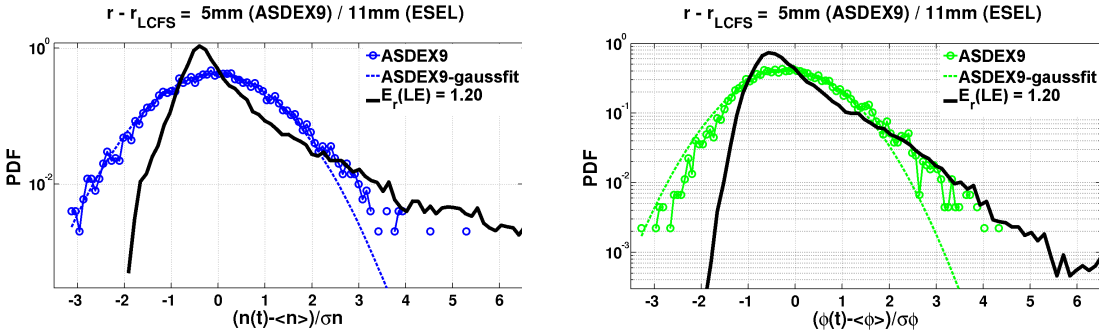

Figure 4.32: PDF of the density n (left) and the plasma potential ϕ (right) calculated near the LCFS . Greater skewness in the ESEL PDFs than in the experimental PDFs.

5. Comparison: COMPASS vs ESEL

5.1 Data and their processing

The experimental data from the COMPASS tokamak were obtained in November 2013 during the discharge #6092. The probe head shown in Fig.(5.1) was inserted into COMPASS plasma by the fast reciprocating horizontal midplane manipulator in position of the outboard midplane of the vessel (cylindrical coordinate $z = 0$) on the low field side (LFS) as we can see in Fig.(5.2).

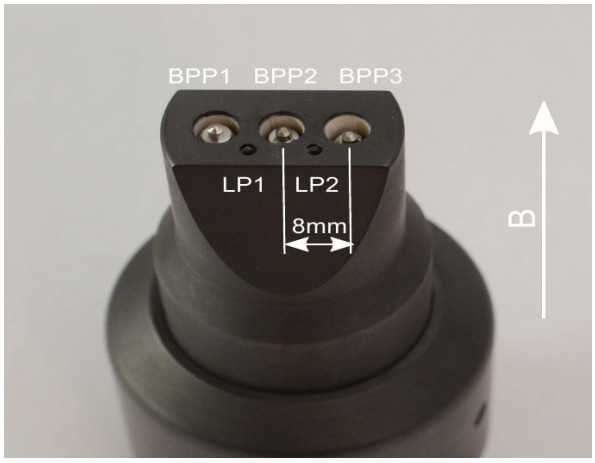

Figure 5.1: The probe head used in COMPASS midplane reciprocating manipulator. Its mouth has diameter 3cm. *There was* 3 *ball-pen probes (BPPs) and* 2 *Langmuir probes (LPs). The vertical direction of the image parallel to the probe head surface corresponds to the toroidal direction in the tokamak and the horizontal direction of the image parallel to the probe head surface corresponds to the poloidal direction in the tokamak. The poloidal distance between LPs and BPPs is* ≈ 4mm

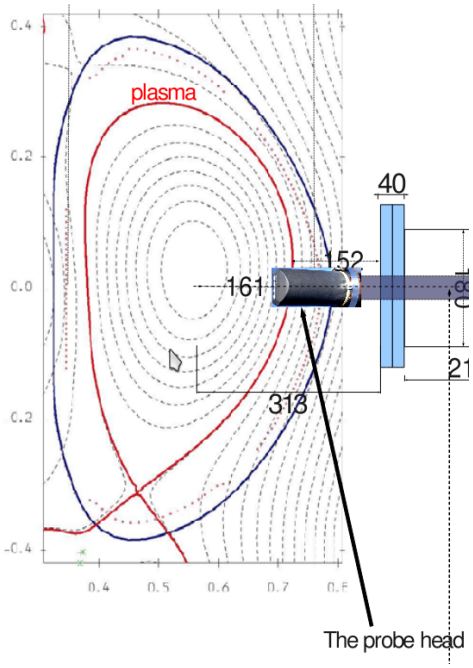

Figure 5.2: The location of the probe head against the COMPASS chamber (the poloidal cross-section is shown in the schema). [59]

[56].

The probe head contained 3 ball-pen probes BPP1, BPP2, BPP3 consisting of stainless steel collectors and alumina shielding and 2 Langmuir probes LP1, LP2 was made of graphite pins (the same as on ASDEX Upgrade tokamak). Ball-pen collectors had diameters of 2mm and ball-pen shielding had interior diameter

5mm. Langmuir pins had diameters of 0.9mm and was protruding 1.5mm into the plasma.

The measurements were performed in D-shaped plasma under this conditions: L-mode, ohmic heating, typical value of toroidal magnetic field in minor axis of the tokamak (at $R \approx 0.56$m) $B_{t0} \approx 1.155$T, plasma current $I_P \approx 110$kA and space and temporal averaged electron (and also ion) density $n_e \approx 5 \cdot 10^{19} m^{-3}$. Shot duration was ≈ 311ms (from ≈ 958ms to ≈ 1269ms) - it was determined from the time progress of the toroidal plasma current. Vacuum pressure was $\approx 7.4 \mu$Pa. T_e in the plasma centre varied between ≈ 600eV and ≈ 1000eV (obtained from the Thomson scattering). The sampling frequency of the data acquisition system was 5Hz.

The data processing was similar as in the case of ASDEX Upgrade. The data from the probes LP1, LP2, BPP2, BPP3 were used. Again the values of the potentials are in V and the values of the temperatures are in eV.

BPP2 was floating and it measured

$$V_f^{\mathrm{BPP2}} \approx \phi_p^{\mathrm{BPP2}} - 0.6 \frac{T_e^{\mathrm{BPP2}}}{e}. \tag{5.1}$$

BPP3 was floating and it measured

$$V_f^{\mathrm{BPP3}} \approx \phi_p^{\mathrm{BPP3}} - 0.6 \frac{T_e^{\mathrm{BPP3}}}{e}. \tag{5.2}$$

LP2 was floating and it measured

$$V_f^{\mathrm{LP2}} \approx \phi_p^{\mathrm{LP2}} - \alpha \frac{T_e^{\mathrm{LP2}}}{e}, \tag{5.3}$$

where $\alpha \approx 2.8$ for $T_e = T_i$ (see equation (1.57)). The indexes has the same meaning as in the case of ASDEX Upgrade data processing in 4.1. The voltage on the probes is always with respect to the tokamak vessel/chamber and tokamak vessel is grounded ($\phi_{\mathrm{vessel}} = 0V$).

The signals from the probes LP1, LP2, BPP2, BPP3 during the probe head motion and the probe head location as a function of time are shown in Fig.(5.3). LP1 was biased sufficiently negatively ($\approx -240V$ when the probe head moved in and $\approx -190V$ when the probe head moved out of the plasma) to measure the I_{is}.

The plasma potential ϕ_p (in V), the electron temperature T_e (in eV) and the electron density n_e (in m^{-3}) were calculated as following:

$$T_e \simeq T_e^{\mathrm{BPP2-LP2}} = \frac{(V_f^{\mathrm{BPP2}} - V_f^{\mathrm{LP2}})}{\alpha - 0.6}, \tag{5.4}$$

$T_e^{\mathrm{BPP2-LP2}}$ is the electron temperature in the area between the probes BPP2 and LP2. $\alpha \approx 2.8$ (see (1.57)) for $T_i/T_e = 1$, as in the case of the ASDEX Upgrade it was used the main value of the temperature ratio as $T_i/T_e = 2$ and range of the ratio from $T_i/T_e = 1$ to $T_i/T_e = 10$ was used for calculation of an uncertainty of the coefficient α.

$$n_e = n_e^{\mathrm{LP1}} = \left(2\frac{\sqrt{m_i}}{Se^{3/2}}\right)\frac{I_{is}}{\sqrt{T_e + T_i}}, \tag{5.5}$$

(2.10). S is a Langmuir probe effective collection area calculated as

$$S = \pi\frac{d^2}{4} + \pi dh, \tag{5.6}$$

where $d \approx 0.9$mm is the diameter of the probe and $h \approx 1.5$mm is the length of a part of the probe which is protruding into the plasma. The ions have much bigger Larmor radius than electrons and they fall down at probe surface from all sides not only from the direction of the magnetic field. For these reason the whole visible probe area was considered as effective collection area.

$$\phi_p = V_f^{\mathrm{BPP2}} + 0.6T_e. \tag{5.7}$$

Small frequencies originating from the background were identified and removed from the signals.

When the probe head reached the deepest location there was sudden drop of voltage of the probe LP1 to 0V as we can see in Fig.(5.4) and the probe LP2 became probably self-emitting as we have seen from their signal (it is also somewhat visible in Fig.(5.3)- the brown signal). That was probably because of an electric arc. We can see in Fig.(5.3) that the arc did not relate to the probe BPP2 and maybe also to BPP3. But it influenced the signal from Langmuir probes. It could be the electric arc between the probes LP1 and LP2. The corresponding data (between time $\approx$ 1095ms) to $\approx$ 1160ms) were not considered. They are not very important because during the movement of the probe head into the plasma all data was used. We had data from all radial probe head locations and missing data from the movement out of the plasma would be only for a confirmation of the data from the movement into the plasma. We can see the used signals from the probes LP1, LP2, BPP2, BPP3 in Fig.(5.5). In Fig.(5.5) there is also the probe head location as a function of time.

All this data was obtained from the WebCDB on tokamak COMPASS homepage [58]. First we had only the probe head location in the major radius coordinates. It was needed to calculate the position of LCFS (at LFS of the midplane of the vessel) in the major radius coordinates from the EFIT data and subsequently the probe head location with respect to the LCFS (in mm). But the EFIT very likely did not compute the LCFS location correctly. There was assumptions from some other discharges that the EFIT compute the LCFS size about 2cm smaller. It is obvious from comparisons between LCFS midplane position gained from EFIT and LCFS midplane position gained from BPP2 signal. The ball-pen probes measure almost the plasma potential and their signal such as the plasma potential should be maximal in time the probes reach the LCFS. The agreement between the LCFS position determined by the ball-pen probe and LCFS position determined by a Doppler reflectometry is shown for example in [57]. We can see such peaks in signals from the probes BPP2 and BPP3 in Fig.(5.3). Therefore the LCFS position was determined by the signal of the BPP2.

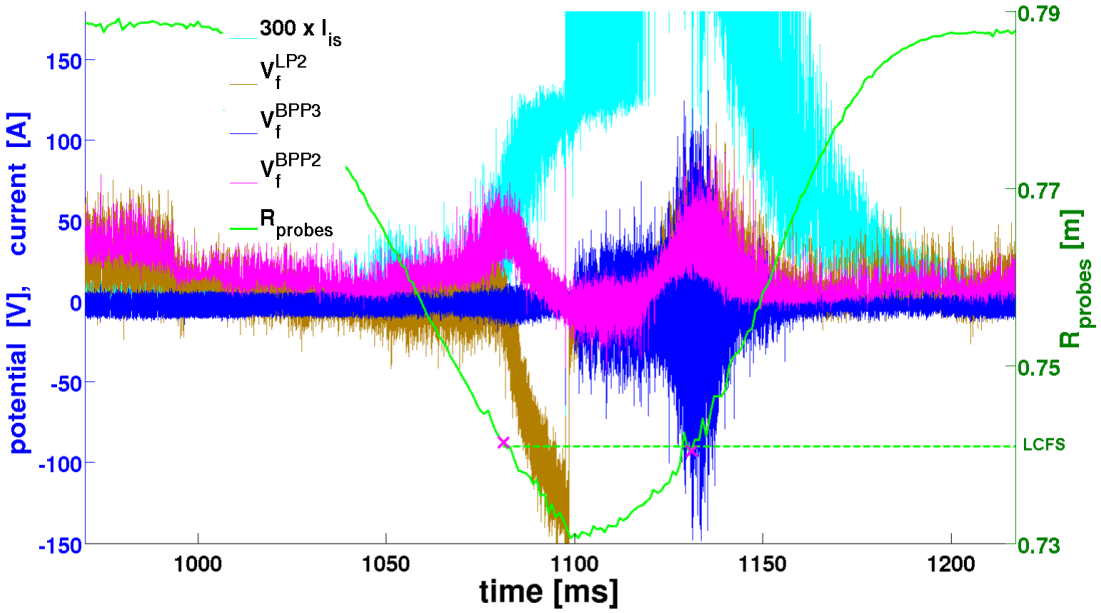

Figure 5.3: The all data from the probes LP1 (I_{is}), LP2 (V_f^{LP2}), BPP2 (V_f^{BPP2}), BPP3(V_f^{BPP3}) during the probe head motion and the probe head location in major radius coordinate. The two pink crosses correspond to the position of the LCFS determined by the ping signal of the probe BPP2.

According to the EFIT the position of the LCFS at LFS of the midplane was fluctuating. The fluctuation of the LCFS position gained from EFIT could be shifted by a value determined from the BPP2 signal. But that shift surely was not the same during the all probe head motion. Therefore I did not consider the fluctuation of the position of the LCFS and considered it constant during the all probe head motion.

The data from the probes BPP2, LP1, LP2 (BPP3 was not essential for further calculation) obtained before the electric arc and appropriate record times were divided into 62 sets, each corresponding to a time interval ≈ 2.016ms. This time interval is short enough to treat probes as steady because it corresponds to the radial probe move less than 2mm which is much shorter than the typical scrape off thickness (1.9). These sets contain 10080 values and that is sufficient for a basic statistic. For each of these 62 sets the corresponding location of the probe head and record time were calculated. Also a statistical moments (mainly arithmetic mean and relative deviation) of each measured quantity for each of these 62 sets were calculated. These 62 values at appropriate 62 positions represent as 62 time average values measured by a fictive steady probes deployed in the SOL.

As in the case of the ASDEX Upgrade data processing in 4.1 the radial profiles of mean $[\langle a\rangle](r)$, radial profiles of relative fluctuations $[\sigma a/\langle a\rangle](r)$, relative profiles of mean divided by negative radial derivative of mean $\lambda(r) = -[\langle a\rangle/(\mathrm{d}\langle a\rangle)/\mathrm{d}r](r)$, conditionally averaged waveforms (CAVs) and probability density functions (PDFs) were calculated, where $a = n$, T_e or ϕ and $\langle\ \rangle$ means time average over 10080 values for each of 62 radial positions. It was calculated again for three quantities : plasma density, electron temperature and plasma po-

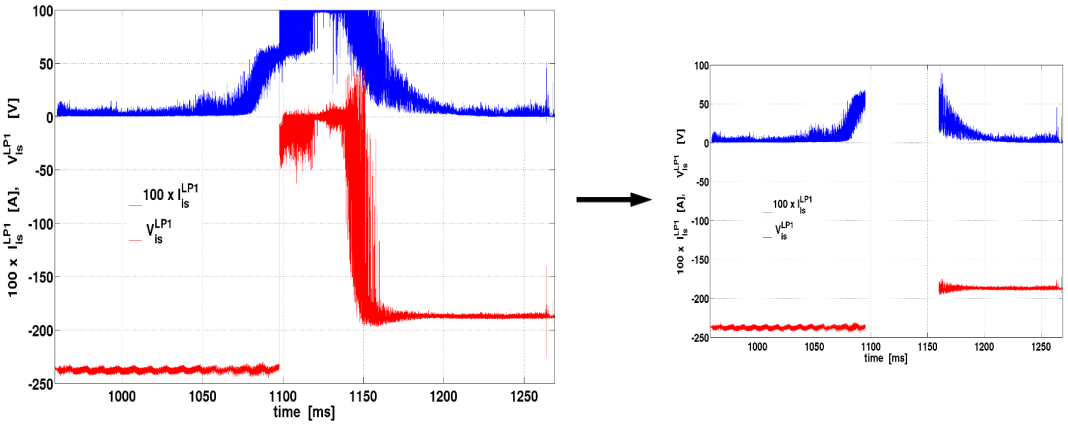

Figure 5.4: (Left) The original voltage and current data from the probe LP1 which measured the ion saturation current. (Right) The data after cutting off the unsuitable data represented very probably an electric arc.

tential and again using the program Matlab.

The **ESEL data** was processed as in the case of the ASDEX Upgrade using the program Matlab. Only small corrections in Matlab scripts and functions were needed.

5.2 Comparison and discussion

For clarity as in the case of the ASDEX Upgrade data in previous chapter 4, $\lambda(r)$ and the data from the discharge #24348 are not shown. The experimental data as well as the ESEL data were again computed for the ratio $T_i/T_e = 2$ and the error bars in the figures of radial profiles of means represent the range of the ratio from $T_i/T_e = 1$ to $T_i/T_e = 10$. I also did not show the CAVs because they are not very plausible. It depends on criterion for width and separation length of events 4.1 and there is also on more reason. As mentioned before in 4.3, we can add to plasma potential ϕ some of its derivative with respect to radial distance which results in optional poloidal velocity. It can together with poloidal boundary conditions lead to a repeated recording of the same blob. In the figures the following labels were used:

- COMPASS — the COMPASS data obtained from the probes during the discharge #6092;
- COMPASS-gaussfit - the gaussian fit of the PDFs calculated from the COMPASS data

In this chapter the general conclusions about the ESEL simulations matching the ASDEX Upgrade tokamak plasma claimed in 4.3.2 are checked for the ESEL simulations matching the COMPASS tokamak plasma.
The 3 simulations were used. They are labeled "without, greater", "without, lower" and "lin."

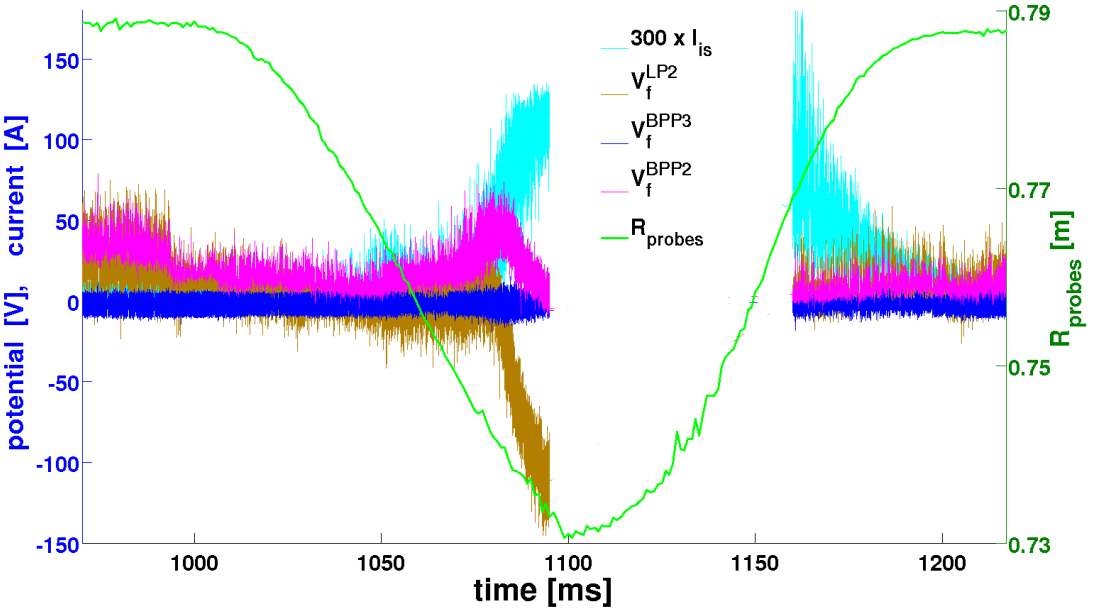

Figure 5.5: The data from the probes LP1 (I_{is}), LP2 (V_f^{LP2}), BPP2 (V_f^{BPP2}), BPP3(V_f^{BPP3}) after cutting of an area representing electric arc and the probe head location in major radius coordinate. The data plotted in 5.2 are only from first part representing the time before the electric arc , second part was not used because LP2 was probably self-emitting after the electric arc.

- "without, greater" is the Prague simulation with job number 4.112. It has not the sheet dissipation term in (3.11) (without it). It has the following parameters and boundary conditions: $T_{e0} = 25\mathrm{eV}$, $T_{i0} = 50\mathrm{eV}$, $n_0 = 1.2 \cdot 10^{19}\mathrm{m}^{-3}$, $M_{||} = 0.5$, $\phi'(LE) = 0$, $n'(LE) = 2.95$, $T'_e(LE) = 86.7$, $D'_{\perp n}$ is multiplied by factor 2, $1/\tau'_{||n}$ is multiplied by factor 1.

- "without, lower" is the Prague simulation with job number 4.118. It has not the sheet dissipation term in (3.11) (without it). It has the following parameters and boundary conditions: $T_{e0} = 25\mathrm{eV}$, $T_{i0} = 50\mathrm{eV}$, $n_0 = 1.2 \cdot 10^{19}\mathrm{m}^{-3}$, $M_{||} = 0.5$, $\phi'(LE) = 0$, $n'(LE) = 2.0$ (lower than in the case of the previous simulation), $T'_e(LE) = 2.0$, $D'_{\perp n}$ is multiplied by factor 2, $1/\tau'_{||n}$ is multiplied by factor 1.

- "lin." is the Prague simulation with job number 4.137. It has the sheet dissipation term in (3.11) in this linear form

$$\frac{1}{\tau'_{||n}} \frac{L_{||d}}{M_{||} 2 L_{||m}} \left[\frac{\langle \phi' \rangle}{\langle T'_e \rangle} - \alpha \right],$$

  where $\langle\rangle$ means average over the time $\tau'_{||n}$, and the following parameters and boundary conditions: $T_{e0} = 25\mathrm{eV}$, $T_{i0} = 30\mathrm{eV}$, $n_0 = 1.5 \cdot 10^{19}\mathrm{m}^{-3}$, $M_{||} = 0.5$, $E'_r(LE) = 0.5$, $n'(LE) = 2.0$, $T'_e(LE) = 2.0$, $D'_{\perp n}$ is multiplied by factor 2, $1/\tau'_{||n}$ is multiplied by factor 1.

I observed the ESEL simulation with linear form of the sheath dissipation term matching the COMPASS tokamak plasma is able to relatively **well describe** the following: repeated recording of the same

- the radial profiles of the mean density ; 5.6 Due to the computational time demands the value $n_0 = 1.5 \cdot 10^{19}\mathrm{m}^{-3}$ was chosen greater than it was calculated from the experiment ($\approx 1.2 \cdot 10^{19}\mathrm{m}^{-3}$). Therefore the model radial profile of the mean density in 5.6 should be slightly lower.

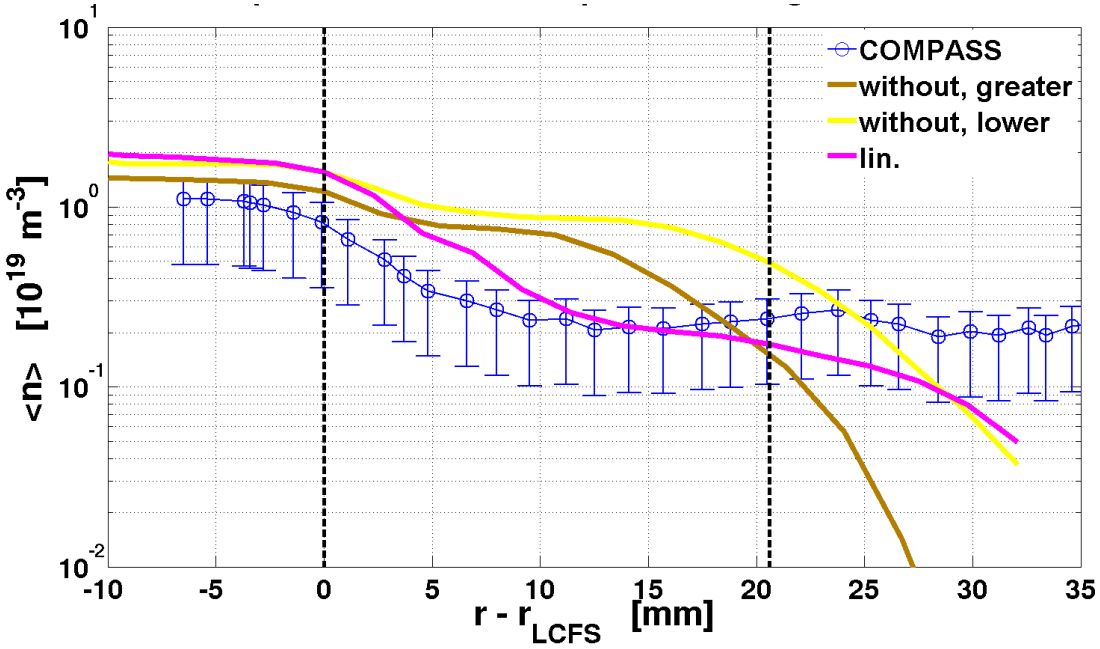

Figure 5.6: The radial profiles of the mean density $\langle n \rangle$. The simulation "lin." with the sheath dissipation term is in relatively good agreement with experiment.

It is remarkable observation. The ESEL is not able to well describe too steep radial profile of the mean density in the case of the ASDEX Upgrade tokamak plasma but it is able to relatively well describe flatter radial profile of the mean density in the case of the COMPASS tokamak plasma (and also TCV tokamak plasma).

- the radial profiles of the relative density and plasma potential fluctuations. ; 5.7, 5.8

  repeated recording of the same

- the normalized PDFs of density n, electron temperature T_e and plasma potential ϕ; 5.9, 5.10, 5.11

But it is again at the cost of other discrepancies. The ESEL simulation with linear form of the sheath dissipation term matching the COMPASS tokamak plasma **badly describes** the following:

- the radial profiles of the mean electron temperature $\langle T_e \rangle$; 5.12
- the radial profiles of the mean plasma potential $\langle \phi \rangle$; 5.13
- the radial profiles of the relative electron temperature fluctuations. 5.14

The two ESEL simulations with without sheath dissipation term matching the COMPASS tokamak plasma generally **badly describe** the radial profile of

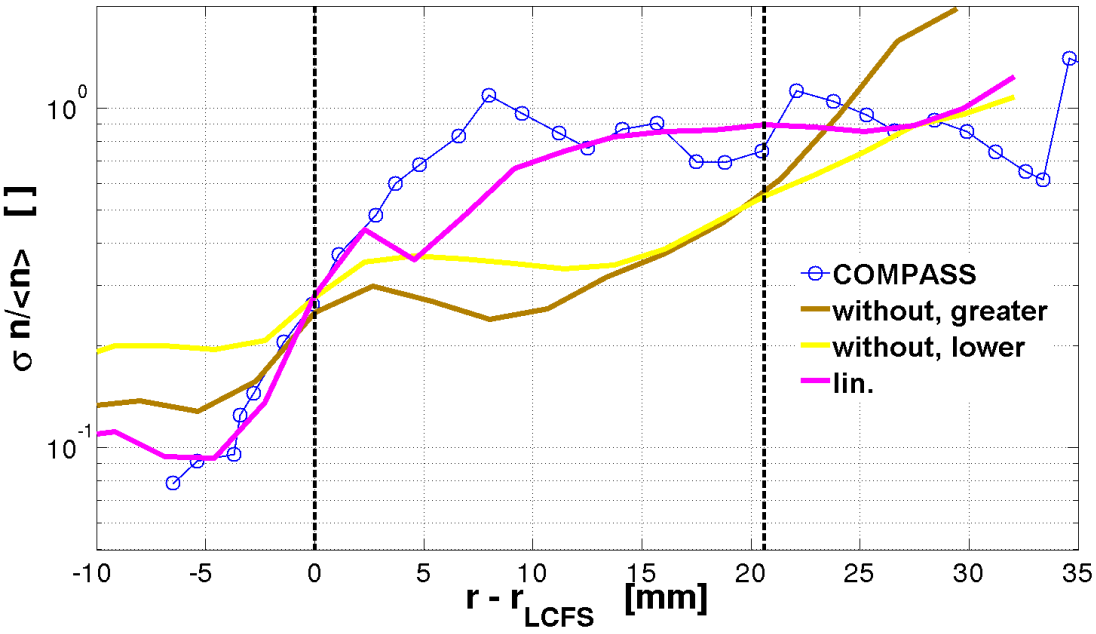

Figure 5.7: The radial profiles of the relative density fluctuations. The simulation "lin." with the sheath dissipation term is in relatively good agreement with experiment.

mean density n 5.6, electron temperature T_e 5.12, plasma potential ϕ 5.13 and the radial profile of the relative density 5.7 and plasma potential 5.8 fluctuations. But they **well describe** the PDFs of the n 5.9, T_e 5.10, ϕ 5.11 and surprisingly finally also the relative electron temperature fluctuations except the area near the LCFS 5.14 (where, as mentioned before, a drift waves and other aspects neglected by the ESEL model play a role).

We can see that only claim about well description of the relative density fluctuations and PDFs was verified. But this fact may not be generally true due to the fact that I used only 3 different simulations in the case of the COMPASS tokamak plasma.

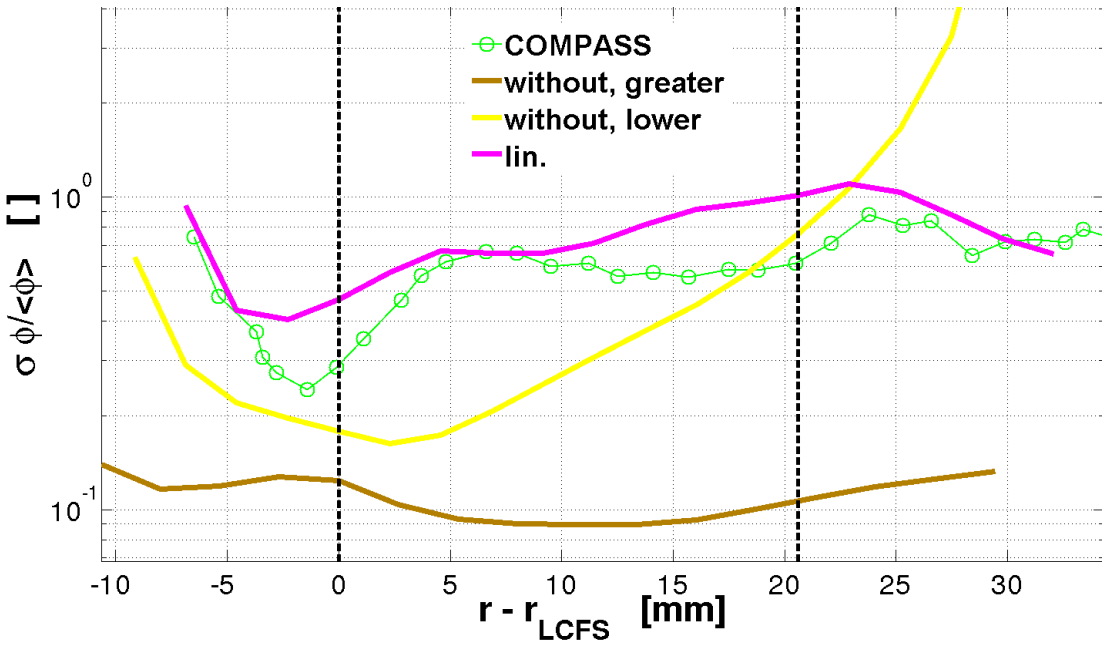

Figure 5.8: The radial profiles of the relative plasma potential fluctuations. The simulation "lin." with the sheath dissipation term is in relatively good agreement with experiment.

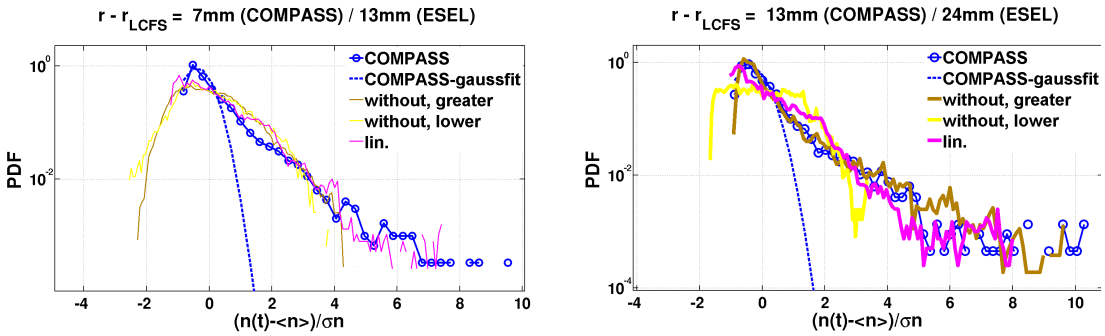

Figure 5.9: PDFs of the density n calculated near (left) and far (right) from the LCFS. Good agreement with experiment.

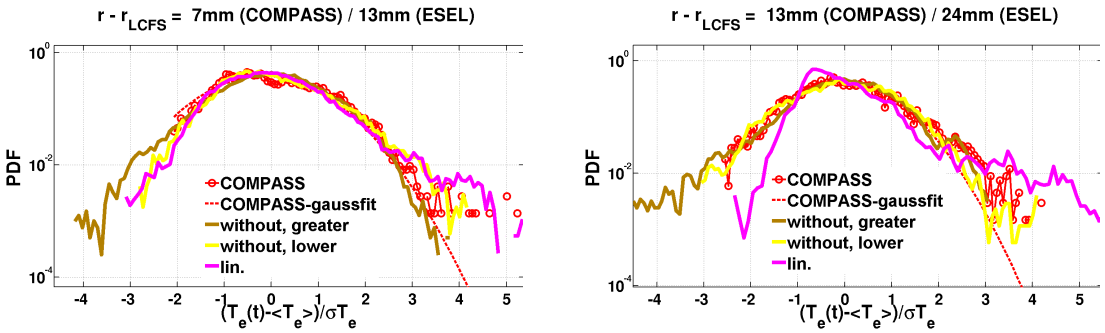

Figure 5.10: PDFs of the electron temperature T_e calculated near (left) and far (right) from the LCFS. Good agreement with experiment.

relative density and plasma potential fluctuations

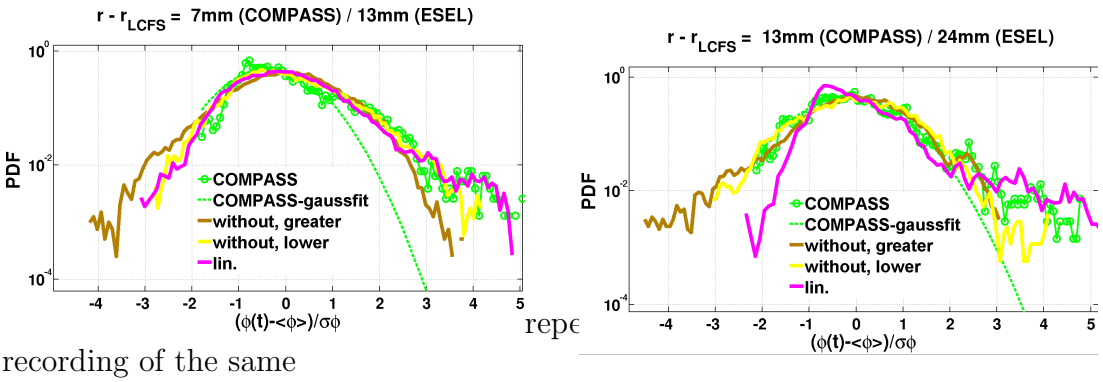

repe

recording of the same

Figure 5.11: PDFs of the plasma potential ϕ calculated near (left) and far (right) from the LCFS. Good agreement with experiment.

relative density and plasma potential fluctuations

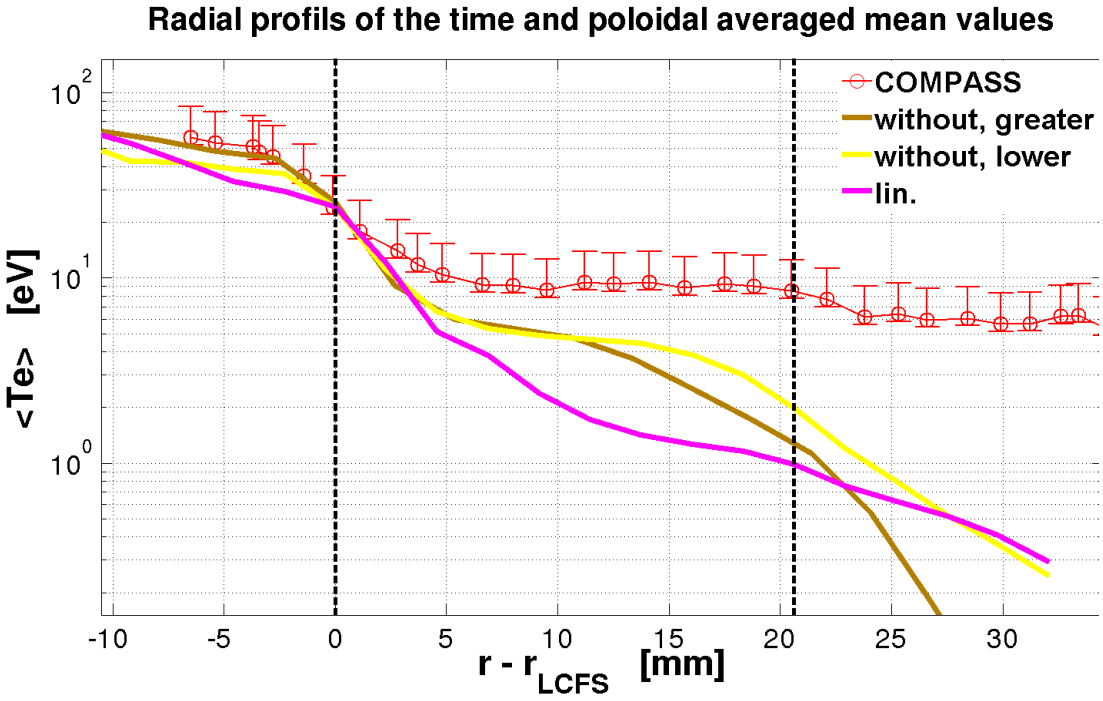

Figure 5.12: The radial profiles of the mean electron temperature.

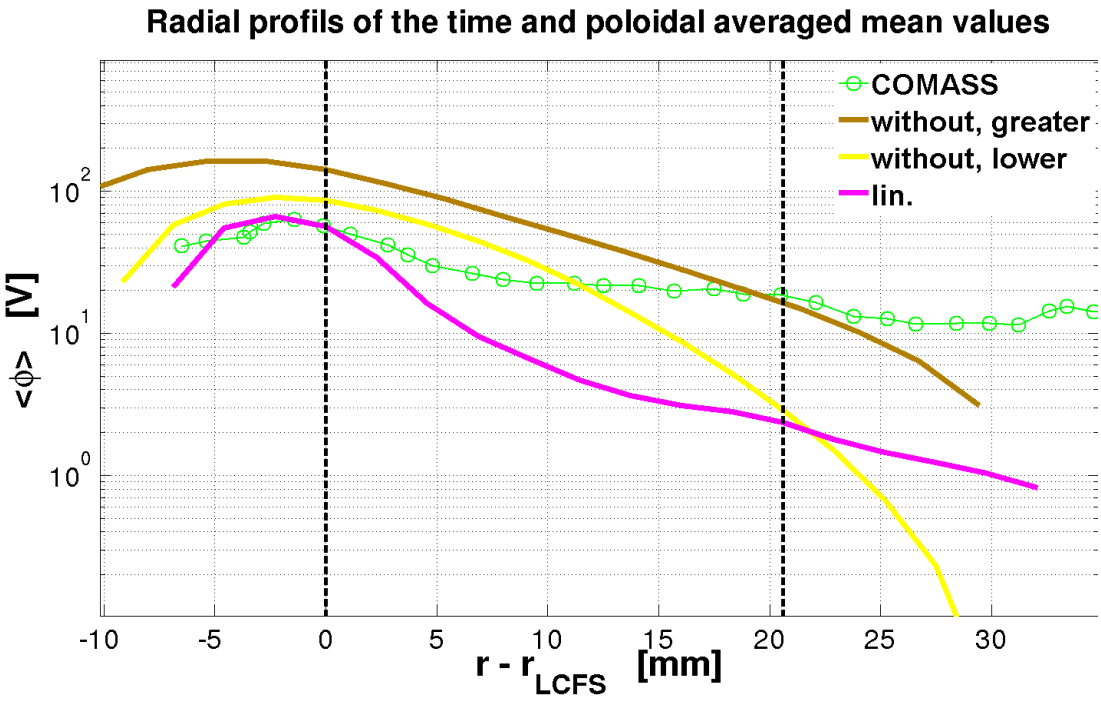

Figure 5.13: The radial profiles of the mean plasma potential.

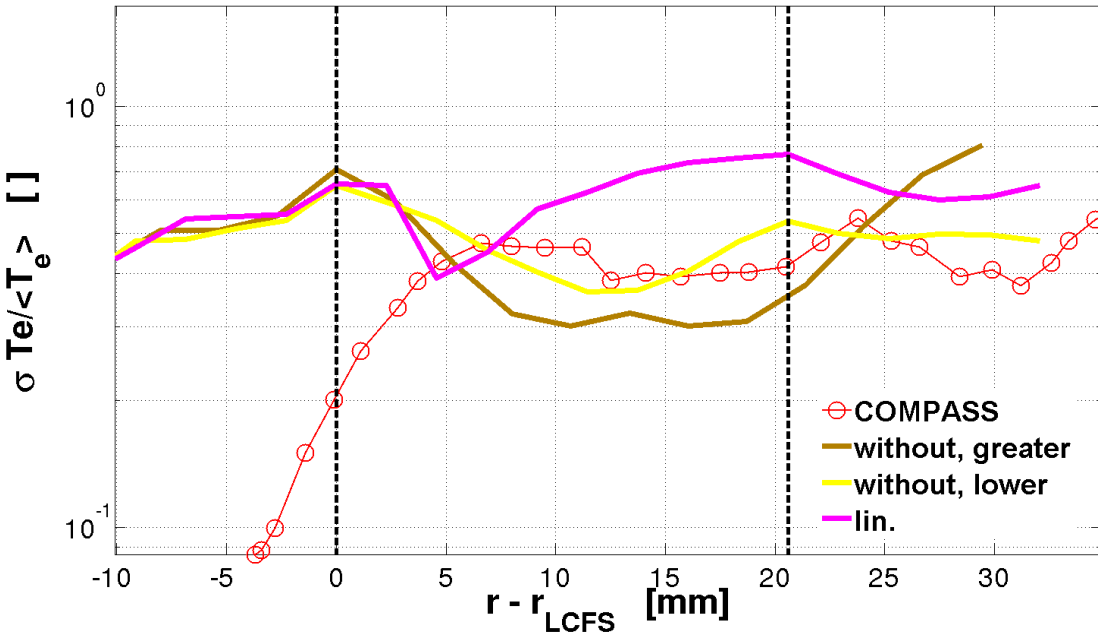

Figure 5.14: The radial profiles of the relative electron temperature fluctuations.

6. Summary and Conclusions

This thesis shows direct comparison between turbulent model ESEL and experimental data, probing plasma in two tokamaks ASDEX Upgrade and COMPASS. This thesis is the first time usage of a tubulence simulation for the COMPASS tokamak. In addition, it shows uniquely detailed comparison of experimental data with lots of simulations with systematically varying several free parameters and the boundary conditions.

The principal findings are:

- 2D ESEL simulation produces turbulence plasma with statistical characteristics quite similar to experimental measurements. This model is based on first physics principles; all the input parameters are based on well-known geometry, measurements of density and temperature at magnetic separatrix and relatively simple physics of ambipolar diffusion along magnetic field lines. It produces turbulence blobs with typical sizes of 1cm and life-times of ≈ 0.1ms, propagating with radial speed of ≈ 1km/s and thus responsible for plasma-wall interaction.

  Generally the quantitative modelling of SOL turbulence and blobs in experiments is difficult and not accurate for a number of reasons such as:

- All of the inputs to such code as ESEL cannot be experimentally measured and setting these necessary additional parameters requires very good judgment. For example boundary conditions, diffusion coefficients or parallel loss times. And the inputs which are experimentally measured such as ion temperature are measured only in some specific locations of the plasma and their functionality in space is not known therefore ESEL uses approximation for it. It is particularly true for modelling 3D plasma with only 2D model ESEL. There are input uncertainties and certain model sensitivity.

- It is important to process the experimental data and simulation data with exactly same approximations and algorithms. It is not always possible to fulfil this condition in the case of the ESEL. Example is computing of the density using by geometry of the probe pins in the case of experimental data. Such approach is not used for the ESEL. Another example is different time step for ESEL data and for the experimental data.

- ESEL and other codes neglect many facts which are not omitted in reality : the LCFS motion, magnetic inhomogeneity (space and temporal), finite Larmor radius, ion heat dynamics, many other possible instabilities and waves in the SOL plasma or central plasma (mainly drift waves) close to the LCFS, and so on.

- The importance of the sheath dissipation term in the governing equation of the ESEL code for the vorticity was verified.

- this thesis demonstrates that ESEL output indeed well describes particular discharges on ASDEX Upgrade (and COMPASS), in particular radial

profiles of temperature and electrostatic potential, together with density fluctuation level. It was demonstrated along with previous publications, that the profile of mean density in the case of the ASDEX Upgrade tokamak plasma is correctly modeled only if the cross-field diffusion coefficient is strongly increased ($6-12\times$) with respect to the well-established neoclassical Pfirsch-Schl**ü**ter diffusion. The reason for so high increase is yet unknown. But increase in this diffusion coefficient results in worse radial profile of the mean electron temperature and plasma potential and too small relative density fluctuations. In the case of the COMPASS tokamak the experimental profile of mean density is flatter and therefore more in agreement with the ESEL model.

The ESEL still in all cases badly describes the relative electron temperature fluctuations and it is apparently still not able to fully describe the tokamak SOL plasma.

The model should be able to describe the behaviour of the tokamak plasma, and predict the plasma parameters for good confinement of the tokamak plasma. The ESEL conforms to the former but not to the latter. At present it is not able to make a good prediction for current tokamaks not to mention the future ITER tokamak.

Bibliography

[1] Edited by MITSURU KIKUCHI, Karl Lackner, Minh Kuang Tran. *Fusion Physics*. International Atomic Energy Agency, Vienna, 2012 ISBN 978-92-0-130410-0.

[2] FTHENAKIS, M., V., Moskowitz D. P. *IThin-film Photovoltaic Cells: Health and Environmental Issues in their Manufacture Use and Disposal*. Progress in Photovoltaics: Research and Applications 3 295-306, (1995). doi: 10.1002/pip.4670030504.

[3] NATIONAL GEOGRAPHIC: http://news.nationalgeographic.com/news/2005/01/0114_050114_solarplastic.html [quoted 2014-03-05]

[4] CENTER FOR TURBULENCE RESEARCH: http://www.stanford.edu/group/ctr/articles/tackle.html [quoted 2014-04-08]

[5] KING, R., R., et al. *40% efficient metamorphic GaInP/ GaInAs/ Ge multijunction solar cells*. Applied Physics Letters 90, 183516, (2007). doi: 10.1063./1.2734507

[6] FORBES: http://www.forbes.com/sites/jamesconca/2012/06/10/energys-deathprint-a-price-always-paid/ [quoted 2014-03-05]

[7] MARKANDYA, A., Wilkinson, P. *Electricity generation and health*. Lancet 2007; 370: 979-90, (2007). Published online at http://www.bigthunderwindpower.ca/files/resources/Electricity_generation_and_health_(The_Lancet_2007).pdf doi: 10.1016/S0140-6736(07)61253-7

[8] WESSON, J.,. *Tokamaks*. Clarendon Press - Oxford, 3rd edition, 2004. ISBN 0 19 8509227.

[9] DAVIDSON, P., A.,. *Turbulence An Introduction for Scientists and Engineers*. University of Cambridge, OXFORD University Press, 2004. ISBN 019852948.

[10] BLEUEL, J.,et al. *The spatial structure of edge fluctuations in the Wendelstein 7-AS stellarator*. New Journal of Physics 4, (2002). online at "http://iopscience.iop.org/1367-2630/4/1/338/pdf/1367-2630_4_1_338.pdf"

[11] ANTAR, Y., G.,et al. *On the scaling of avaloids and turbulence with the average density approaching the density limit*. Physics of Plasmas **12**, 082503 (2005). DOI: 10.1063/1.19535592

[12] ANTAR, Y., G.,et al. *Universality of intermittent convective transport in the scrape-off layer of magnetically confined devices*. Physics of Plasmas **10**, (2003). DOI: 10.1063/1.1536166

[13] GRAVES, P., J.,et al. *Self-similar density turbulence in the TCV tokamak scrape-off layer*. Plasma Phys. Control. Fusion **47**, L1-L9 (2005). DOI: 10.1088/0741-3335/47/3/L01

[14] SPOLAORE, M., et al. *Vortex-Induced Diffusivity In Reversed Field Pinch Plasmas*. Physical Review Letters **93**, 215003 (2004). DOI: 10.1103/PhysRevLett.93.215003

[15] GRULKE, O., et al. *Comparative experimental study of coherent structures in a simple magnetized torus*. Plasma Physics and Controlled Fusion **43**, 525-542 (2001). PII: S0741-3335(01)16320-7

[16] MAQUEDA, J., R., et al. *Intermittency in the scrape-off layer of the National Spherical Torus Experiment during H-mode confinement*. Journal of Nuclear Materials 415, S459-S462 (2011). DOI: 10.1016/j.jnucmat.2010.11.002

[17] GRULKE, O., et al. *Radially propagating fluctuation structures in the scrape-off layer of Alcator C-Mod*. Physics of Plasmas **13**, 012306 (2006). PII: S0741-3335(01)16320-7

[18] FIELD, R., A., et al. *Comparison of measured poloidal rotation in MAST spherical tokamak plasmas with neo-classical predictions*. Plasma Physics and Controlled Fusion **51**, 105002 (17pp) (2009). DOI: 10.1088/0741-3335/51/10/105002

[19] D'IPPOLITO, A., D., et al. *Convective transport by intermittent blob-filaments: Comparison of theory and experiment*. Physics of Plasmas **18**, 060501 (2011). DOI: 10.1063/1.3594609

[20] Edited by KORSHOLM, S., B., et al. *Association Euratom - RisøNational Laboratory for Sustainable Energy, Technical University of Denmark - Annual Progress Report 2008*. ISSN: 0106-2849 ISBN: 978-87-550-3738-0 online at "http://orbit.dtu.dk/fedora/objects/orbit:82839/datastreams/file_5113068/content"

[21] HAVLICKOVA, E., et al. *Steady-state and time-dependent modelling of parallel transport in the scrape-off layer*. Plasma Phys. Control. Fusion **53**, 065004 (24pp) (2011). DOI: 10.1088/0741-3335/53/6/065004

[22] BISAI, N., et al. *Edge and scrape-off layer tokamak plasma turbulence simulation using two-field fluid model*. Phys. Plasmas **12**, 072529 (2005). DOI: 0.1063/1.1942427

[23] RUSSELL, D., A., et al. *Comparison of scrape-off layer turbulence simulations with experiments using a synthetic gas puff imaging diagnostic*. Phys. Plasmas **18**, 022306 (2011). DOI: 10.1063/1.3553024

[24] MYRA, J., R., et al. *Reduced model simulations of the scrape-off-layer heat-flux width and comparison with experiment*. Phys. Plasmas **18**, 012305 (2011). DOI: 10.1063/1.3526676

[25] LI, B., et al. *Plasma transport and turbulence in the Helimak: Simulation and experiment*. Phys. Plasmas **16**, 082510 (2009). DOI: 10.1063/1.3212591

[26] XU, X., Q., et al. *Dynamical simulations of boundary plasma turbulence in divertor geometry*. New Journal of Physics **4**, 53 (2002). PII: S1367-2630(02)34656-1

[27] ZWEBEN, S., J., et al. *Comparison of scrape-off layer turbulence in Alcator C-Mod with three dimensional gyrofluid computations*. Phys. Plasmas **16**, 082505 (2009). DOI: 10.1063/1.3191721

[28] ZWEBEN, S., J., et al. *Edge turbulence imaging in the Alcator C-Mod tokamak*. Phys. Plasmas **9**, 1981 (2002). DOI: 0.1063/1.1445179

[29] TERRY J., L., et al. *Observations of the turbulence in the scrape-off-layer of Alcator C-Mod and comparisons with simulation*. Phys. Plasmas **10**, 1739 (2003). DOI: 10.1063/1.1564090

[30] ENDLER, M., et al. *The fine structure of ELMs in the scrape-off layer*. Plasma Physics and Controlled Fusion **47**, 219-240 (2005). DOI: 10.1088/0741-3335/47/2/002

[31] KOMM, M.. *Interakce plazmatu se stenou tokamaku*. Master thetis, Charles University in Prague, Czech Republic, 2007

[32] CHEN, F., F.,. *Introduction to Plasma Physics*. Plenum Press, New York, 1974. ISBN 978-1-4757-0459-4 (eBook).

[33] HRON, M.,et al. *EDGE TURBULENCE AT PLASMA POLARISATION ON THE CASTOR TOKAMAK* . Czechoslovak Journal of Physics, Vol. **49**, (1999). online at "http://server.ipp.cas.cz/ horacek/pub/hron_turbulence_biasing_castor_99.pdf"

[34] HORACEK, J.,et al. *Interpretation of fast measurements of plasma potential, temperature and density in SOL of ASDEX Upgrade*. Nucl. Fusion **50**, (2010). doi: 10.1088/0029-5515/50/10/105001. online at "stacks.iop.org/NF/50/105001"

[35] COHEN, R., H., et al. *Theory and fluid simulations of boundary-plasma fluctuations*. Nucl. Fusion **47**, 612-625 (2007). doi: 10.1088/0029-5515/47/7/012. online at "http://iopscience.iop.org/0029-5515/47/7/012/pdf/0029-5515_47_7_012.pdf"

[36] DUDSON, B., D., et al. *Experiments and simulation of edge turbulence and filaments in MAST*. Plasma Phys. Control. Fusion **50**, 124012 (2008). doi: 10.1088/0741-3335/50/12/124012. online at "http://iopscience.iop.org/0741-3335/50/12/124012/pdf/0741-3335_50_12_124012.pdf"

[37] TERRY, J., L., et al. *Spatial structure of scrape-off-layer filaments near the midplane and X-point regions of Alcator-C-Mod*. J. Nucl. Mater. **390**, 339 (2009). doi: 10.1016/j.jnucmat.2009.01.152.

[38] BOEDO, J., A., et al. *Fast scanning probe for the NSTX spherical tokamak.* Review if scientific instruments **80**, 123506 (2019). doi: 10.1063/1.3266065.

[39] NAULIN, V.,et al. *Turbulence modeling of JET SOL Plasma.* In Proceedings of the 21st IAEA Fusion Energy Conference, 2006. online at "http://www.iop.org/Jet/fulltext/EFDC060519.pdf" [quoted 2014-02-12]

[40] VERGOTE, M., et al. *Discussion of SOL turbulence properties in TEXTOR by means of ESEL simulations* . In38th EPS Conference on Plasma Physics, 2011. online at "http://ocs.ciemat.es/EPS2011PAP/pdf/P5.068.pdff" [quoted 2014-02-12]

[41] MILITELLO, F.,et al. *Simulations of edge and scrape off layer turbulence in mega ampere spherical tokamak plasmas* . Plasma Phys. Control. Fusion 54, 2012 doi:10.1088/0741-3335/54/9/095011. online at "http://iopscience.iop.org/0741-3335/54/9/095011/article" [quoted 2014-02-12]

[42] HORACEK, J.. *Measurement of edge electrostatic turbulence in the TCV tokamak plasma boundary* . PhD thesis, EPFL, Schwitzerland, 2006 ISSN 0458-5895.

[43] VONDRACEK, P.. *Study of edge plasma physics of tokamak COMPASS by means of two reciprocating probes* . Master thesis, CTU in Prague, Czech Republic, 2012

[44] GARCIA, O., E.,et al. *Turbulence and intermittent transport at the boundary of magnetized plasmas.* Physics of Plasmas **12**, 062309 (2005). doi:10.1063/1.1925617.

[45] FUNDAMENSKI, W., et al. *Dissipative processes in interchange driven scrape-off layer turbulence.* Nucl. Fusion **47**, 417-433 (2007). doi:10.1088/0029-5515/47/5/006.

[46] GARCIA, O., E.,et al. *Interchange turbulence in the TCV scrape-off layer.* Plasma Phys. Control. Fusion **48**, (2006) L1-L10. doi:10.1088/0741-3335/48/1/L01. online at "http://iopscience.iop.org/0741-3335/48/1/L01/"

[47] KIRNEV, S., G.,et al. *Intermittent transport in the plasma periphery of the T-10 tokamak.* Plasma Phys. Control. Fusion **46**, 621-637 (2004). doi:10.1088/0741-3335/46/4/004.

[48] GARCIA, O., E.,et al. *Confinement and bursty transport in a flux-driven convection model with sheared flows.* Plasma Phys. Control. Fusion **45**, 919-932 (2003). PII: S0741-3335(03)55405-7.

[49] GARCIA, O., E.,et al. *Fluctuations and transport in the TCV scrape-off layer.* Nucl. Fusion 47, (2007) 667. doi:10.1088/0029-5515/47/7/017. online at "http://iopscience.iop.org/0029-5515/47/7/017/"

[50] GARCIA, O., E.,et al. *Collisionality dependent transport in TCV SOL plasmas*. Plasma Phys. Control. Fusion 49, (2007) B47. doi:10.1088/0741-3335/49/12B/S03. online at "http://iopscience.iop.org/0741-3335/49/12B/S03/"

[51] GARCIA, O., E.,et al. *Turbulent transport in the TCV SOL*. Journal of Nuclear Materials 363-365, (2007) 575. doi:10.1016/j.jnucmat.2006.12.063. online at "http://www.sciencedirect.com/science/article/pii/S0022311506006593"

[52] KATSUMATA, I., AND OKAZAKI, M., *Ion Sensitive Probe-A New Diagnostic Method for Plasma in Magnetic Fields*. Japanese Journal of Applied Physics, (1967). doi:10.1143/JJAP.6.123.

[53] ADAMEK, J.,et al. *A novel approach to direct measurement of the plasma potential*. Czechoslovak Journal of Physics, Vol. 54, (2004).

[54] ADAMEK, J.,et al. *Ball-Pen Probe Measurements in L-Mode and H-Mode on ASDEX Upgrade*. Contrib. Plasma Phys., 50, No. 9, 843 -859 (2010). doi:10.1002/ctpp.201010145.

[55] ADAMEK, J.,et al. *Fast ion temperature measurements using ball-pen probes in the SOL of ASDEX Upgrade during L-mode*. 38^{th} EPS Conference on Plasma Physics (2011).

[56] ADAMEK, J.,et al. *Direct plasma potential measurements by ball-pen probe and self-emitting Langmuir probe on COMPASS and ASDEX Upgrade*. Contrib. Plasma Phys., 3, (2014).

[57] MüLLER, J.,et al. *Latest investigations on fluctuations, ELM filaments and turbulent transport in the SOL of ASDEX Upgrade*. Nucl. Fusion, **51**, 073023 (11pp) (2011). DOI: :10.1088/0029-5515/51/7/073023

[58] *http://www.tok.ipp.cas.cz/webcdb/generic_signals* [quoted 2014-02-26]

[59] *http://www.ipp.cas.cz/Tokamak/* [quoted 2014-02-26]

[60] GARCIA, O., E., *Collective motions in non-uniformly magnetized plasmas*. European Journal of Physics **24**, (2003) 331-339. online at "stacks.iop.org/EJP/24/331"

[61] STANGEBY, P.,. *The Plasma Boundary of Magnetic Fusion Devices*. Institute of Physics Publishing Ltd, 2000. ISBN 0 7503 0559 2.

[62] KOCAN, M.,et al. *Edge ion-to-electron temperature ratio in the Tore Supra tokamak*. Plasma Phys. Control. Fusion 50, (2008). doi:10.1088/0741-3335/50/12/125009.

[63] SEIDL, J., Krlín, L., *Interchange Driven Turbulence and Bellan Instability in Tokamak Scrape-off Layer*. WDS' 09 Proceedigs of Contributed Papers, Part III, 64-70, 2009. ISBN 978-80-7378-103-3.

[64] NOLD, B., et al. *Influence of temperature fluctuations on plasma turbulence investigations with Langmuir probes*. New Journal of Physics **14**, 063022 (2012). doi:10.1088/1367-2630/14/6/063022.

List of Abbreviations

ITER	—	International Thermonuclear Experimental Reactor
JET	—	Joint European Torus
SOL	—	Scrape Off Layer
LCFS	—	Last Closed Flux Surface
NBI	—	Neutral Beam Injection
LP	—	Langmuir Probe
BPP	—	Ball-Pen Probe
LFS	—	Low Field Side
HFS	—	High Field Side
ESEL	—	ElectroStatic Edge-soL
I-V	—	Current-Voltage
EFIT	—	Equilibrium fitting (code)
LRDFIT	—	LR (inductance and resistance) circuit model with Data FITing capabilities
ELM	—	Edge Localized Mode
2D	—	two-dimensional
3D	—	three-dimensional
CAV	—	Conditionally AVeraged wave form
PDF	—	Probability Distribution Function
LE	—	Left Edge